THE UNIVERSITY OF CALGARY

Measurement of Electrical Properties of Biological Cells Using a Dielectrophoretic Levitation System

by

Jingping Xie

A THESIS

SUBMITTED TO THE FACULTY OF GRADUATE STUDIES

IN PARTIAL FULFILLMENT OF THE REQUIREMENTS FOR THE

DEGREE OF MASTER OF SCIENCE

DEPARTMENT OF ELECTRICAL AND COMPUTER ENGINEERING

CALGARY, ALBERTA, CANADA

September, 1991

ISBN 0-315-75245-9

THE UNIVERSITY OF CALGARY

FACULTY OF GRADUATE STUDIES

The undersigned certify that they have read, and recommend to the Faculty of Graduate Studies for acceptance, a thesis entitled, "Measurement of Electrical Properties of Biological Cells Using a Dielectrophoretic Levitation System", submitted by Jingping Xie in partial fulfillment of the requirements for the degree of Master of Science.

Supervisor, Dr. K.V.I.S. Kaler
Dept. of Electrical and Computer Engineering

Dr. R.A. Stein
Dept. of Electrical and Computer Engineering

Dr. R. Paul
Dept. of Chemistry

Dr. M.M. Moloney
Dept. of Biological Sciences

Date: 22/12/91

ABSTRACT

Dielectrophoretic (DEP) levitation has been shown to be useful as a technique for determining dielectric (polarization) properties of single particles ranging from insulating and conducting spheres to complex biological cells.

In this thesis, a DEP levitation system is described which allows the precise measurement of polarization spectra of biological cells in both positive and negative DEP spectral regions. In addition, an electrophoretic measuring scheme has been proposed and implemented, which enables the measurement of the cell surface charge with better resolution than the conventional method. Using this system, the DEP spectra of *Canola* plant protoplasts have been measured over a wide range of frequencies (1 Hz to 50 MHz) under various suspending medium conditions. It is found that the experimental spectra thus obtained can be interpreted, at least over the mid and high frequency range, in terms of a shelled spherical model. Furthermore, utilizing such a model, methods have been developed to derive various cellular parameters from the measured DEP spectra. For *Canola* protoplasts, the estimated values of membrane capacitance, membrane conductivity, and cytoplasm conductivity are 0.55 ± 0.02 $\mu F/cm^2$, 0.01 $\mu S/cm$, and 4000 $\pm$ 200 $\mu S/cm$, respectively.

ACKNOWLEDGEMENTS

I would like to express my sincere appreciation, gratitude, and indebtedness to my supervisor, Dr. K.V.I.S. Kaler, for providing me with the opportunity to work on this exciting project. His constant support, including financial support from his research grant awarded by NSERC, invaluable encouragement, and friendly guidance are thankfully acknowledged. Grateful appreciations are extended to the Department of Electrical and Computer Engineering for the financial support that was given in the form graduate teaching (GAT) and graduate research (GAR) assistantships. I also wish to thank Dr. R. Paul and Dr. T.B. Jones for many fruitful discussion, Dr. M.M. Moloney for teaching me to plant the *Canola* seeds and allowing me access to the facilities in greenhouse, and Alan Tai for preparing the enzyme solution. I would also like to express my deep gratitude to the above examiners for spending their precious time and efforts in assessing this work. The timely help from Jack Yang and Yanya Shen in finalizing this thesis are also greatly appreciated.

Finally, but not the least, the patience, love, and understanding of my wife, Xiaojuan, has made this thesis possible. I would also like to thank my lovely daughter, Lauren, for not disrupting my sleep too much.

DEDICATION

To my parents and my family

TABLE OF CONTENTS

LIST OF TABLES

LIST OF FIGURES

LIST OF SYMBOLS

Operators:

∇ ..... gradient operator

$|...|$ ..... absolute value

$Re[...]$ ..... real part

$Im[...]$ ..... imaginary part

Symbols:

α, β, γ ..... three major dispersions observed in biological systems

$\underline{\varepsilon}$ ..... complex permittivity

ε' ..... real part of the complex permittivity

ε'' ..... imaginary part of the complex permittivity

ε_∞ ..... high frequency limit of real part of $\underline{\varepsilon}$

ε_s ..... low frequency limit of real part of $\underline{\varepsilon}$

ε_1 ..... permittivity of the suspending medium

ε_2 ..... permittivity of the homogeneous particle

$\underline{\varepsilon}_{2eff}$ ..... complex permittivity of shelled sphere (biological cell)

ε_m ..... permittivity of cell membrane

ε_0 ..... absolute permittivity of free space

σ_1 ..... conductivity of the suspending medium

σ_2 ..... conductivity of the homogeneous particles

σ_m ..... conductivity of the cell membrane

σ_{eff} ..... effective conductivity of the cell

τ ..... relaxation time constant

τ_{bl} ..... relaxation time constant of bound counterion layer

ω ..... radian frequency

ρ_0 ..... surface density of bound counterion

ρ_s ..... surface charge density

ξ ..... energy barrier

γ_1 ..... mass density of the suspending medium

γ_2 ..... mass density of the cell

η ..... viscosity of water

C ..... coefficient

C_m ..... specific membrane capacitance

d ..... thickness of the membrane

D ..... diffusion coefficient of counterions

e_0 ..... charge

E_{rms} ..... applied electric field intensity in root-mean-square

f ..... frequency of the applied field

f_0 ..... mid range cross-zero frequency in Re[$\underline{K}_e$]

f_H ..... fixed high frequency

$f(z)$ ..... position function

$\langle F_{DEP} \rangle$ ..... time-average dielectrophoretic force

F_g ..... gravitational force

g ..... acceleration due to gravity

G_p, G_i, G_d ..... gain coefficients of PID controller

k ..... Boltzman's constant

$\underline{K}_e$ ..... dimensionless excess (effective) polarizability of the particle with respect to the medium

K_s ..... surface conductance

K_z ..... impedance ratio

P_{eff} ..... induced dipole moment

Q_s ..... surface charge

R ..... particle (cell) radius

T ..... absolute temperature (Kelvin)

V ..... applied voltage

V_{rms} ..... applied voltage in r.m.s.

V_f ..... applied low scanning frequency voltage

V'_f ..... actual low frequency voltage applied to the suspension

V_{HS} ..... single frequency levitation voltage at f_H

V_{CH} ..... levitation voltage of f_H when V_f is also applied

V_{dc} ..... applied d.c. voltage

z ..... cell position

Z_e ..... chamber impedance

Z_{bs} ..... impedance of bulk suspension

CHAPTER 1

INTRODUCTION

Electrical and dielectric properties of biological cells and materials are of interest for many reasons and hold a pre-eminent position in several areas of physiology, biophysics and biomedical engineering. As for the human body, these properties determine the pathways of current flow through the body and are therefore important in the measurements of physiological parameters using impedance techniques and studies of biological effects of electromagnetic fields[1]. Clinically, the precise measurements of electrical properties of biological cells and determinations of cellular parameters can provide a diagnostic tool for detection of various effects (such as chemical agents, drugs, nuclear radiation, etc.) on cells and discrimination between normal cells and "diseased" cells (such as cancer cells). In modern biotechnology, electrofusion and electroporation of biological cells become more and more important in new species hybridization and agent transfer, though the fundamental mechanisms involved remain to be fully understood. In addition, finding the optimal applied field parameters (such as field strength, pulse shape and duration, and field frequency) is crucial for improving "yield", which requires a thorough understanding of the electrical properties of cells, cell-medium and cell-cell interactions.

In most situations biological cells or particles are immersed in a specific electrolyte or suspending medium. The electrical (dielectric) response of the cells is therefore

influenced by the electrical properties of the cellular compartments (e.g. membrane, cytoplasm) and those of the suspending medium. By measuring the electrical and more specifically, dielectric response (especially in the frequency domain), it is possible to understand the underlying polarization mechanism(s) and to determine the properties of biological cells.

In the past, a variety of measurement techniques have been devised to quantify the characteristic dielectric response. However, each is applicable in a limited set of circumstances. The most common approaches and their associated areas of applications and limitations are briefly discussed below.

1.1. Cell Suspension Method

The "cell suspension" method is frequenctly used technique to study the frequency-dependent dielectric properties of biological cells in suspension and tissue samples[1-4]. Here, the cell suspension forms a heterogenous dielectric material which is introduced into a capacitance chamber. Both the conductance and capacitance are measured over a wide frequency range using a sensitive impedance bridge technique. In the high frequency range (MHz to GHz), a transmission-line approach can be used, in which the sample is the dielectric material in the transmission line and measurements are made of the response of the line, either in time domain (Time Domain Spectroscopy)[5] or in the frequency domain, to determine the loss (ε'') and permittivity (ε') of the sample. From such measurements the dielectric properties (such as the effective permittivity) of the cells may then be extracted by invocation of the appropriate mixture formulae [1,4,6,7]. Such measurements on a cell suspension have provided valuable insight concerning the

frequency-dependent polarization response mechanisms of intact cells. For a cell suspension, the measured permittivity changes occur (where polarization dispersions occur) in three regions of the frequency spectrum. These are labelled, in the order of increasing field frequency, as the α, β, γ dispersion[1,2] as shown in Figure 1.1.

Since such measurements are all based on the relative change of impedance of the suspension chamber, a relatively high concentration of cells is required in order to observe such a change, which would result in the cell-cell interactions and hence introduce error to the derived effective permittivity of cells when using certain mixture formula[1]. In addition to this, in the low frequency region where conductivity effects dominate, the measurement apparatus must be extremely sensitive to small changes in the reactive component of the measured impedance[8].

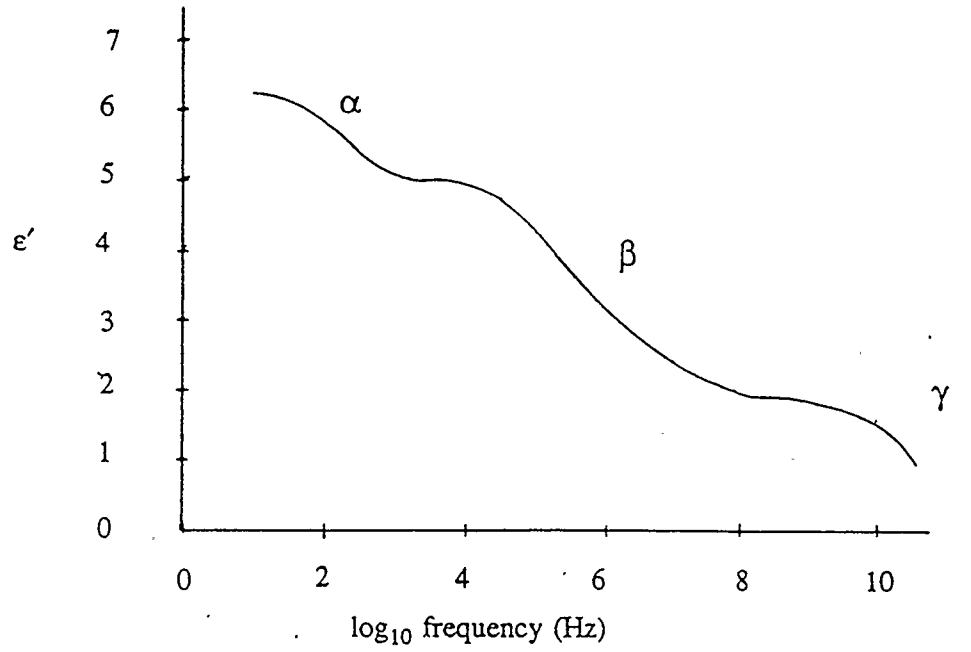

Figure 1.1. A schematic illustration of three major dispersion regions found in typical cell suspension and tissues (after Foster and Schwan[1]).

1.2 Micropipette Technique

The micropipette technique, unlike the suspension method, has been devised to measure the membrane conductance and capacitance of a selected individual cell by several investigators[9,10] in order to study the ion transport properties of the cell membrane. The micropipette, which is made of a borosilicate glass capillary and is filled with salt solution, serves as the probing electrode. When conducting the measurement, a tight seal is established between the cell membrane and the pipette tip by applying a weak suction and a measuring bridge is set up between this tip electrode and a reference electrode immersed in the suspending medium. These measurements are generally restricted to low frequencies (~4 Hz to 1 kHz) due to the large parasitic impedance of the micropipette, and furthermore the technique is inherently invasive.

1.3 Electrorotation Method

Several investigators[11,12] have studied the rotational behaviour of biological cells induced by a rotating electric field. It has been shown[11] that the rotational speed is related to the imaginary part of the effective polarizability $\underline{K}_e$ of the cell (see chapter 3). By measuring the cell rotation rates at various frequencies of the applied field, yields the frequency dependent rotation spectrum. By fitting the measured rotation spectrum to that predicted theoretically (using suitable model), certain cellular parameters, such as membrane capacitance, may be extracted. Although this method has the advantage of simplicity, the manual data collection can be rather tedious and erroneous. Furthermore, cells have to be exposed to moderately high electric field intensities in order to quantify the rotation rate with resonable certainty or confidence level.

1.4 Electrophoresis

Most cell types maintain a net negative surface charge at physiological pH[13,14], and the surface charges are attributed to certain types of protein groups[15]. Thus when placed in a dc electrostatic field, the cells tend to move toward the anode electrode. By measuring this "electrophoretic velocity", several investigators have utilized this property to determine the net surface charge[14,15], which in turn is affected by the "physiological state" of the cell. Electrophoresis has also been used for cell separation[16].

1.5 Dielectrophoresis

Dielectrophoresis (DEP) is the motional response of electrically polarizable particles when subjected to a non-uniform electric field[17]. Unlike electrophoresis, it does not require a net charge on the particle and is independent of field polarity. Here the force acting on a neutral particle is a function of the excess (or effective) polarizability of the particle with respect to the surrounding medium, the frequency of the applied field, the local field magnitude and gradient, and the particle shape and volume. Dielectrophoresis has already acquired various applications in industry, for example, pumping liquids and powders, classifying and separating minerals, removing particulate matter from suspension in liquids or gas, and anchoring toner particles in Xerography. Dielectrophoresis has primarily been applied to biological cells in three ways. First, as a method of measurement, it has been used to obtain the polarization spectrum over a wide frequency range, second for separation of cells differing in the polarization characteristics, and third for cellular electromanipulation. Since the 1970's, several investigators have studied the behaviour of bioparticles under non-uniform electric field and various methods, based on

the principle of dielectrophoresis, have been developed for measuring the frequency-dependent polarization response (also referred to as DEP spectra) of biological cells[17-26]. Most of these methods (see detailed review in Chapter 2) are based on an indirect measurement of the DEP force, conducted on a large quantity of cells. Therefore they are inevitably subject to error and averaging effect. However, this has been circumvented by the introduction of DEP levitation[27,19,20].

Levitation is an effective technique for studying small particle properties and interactions. Methods have been developed to levitate particles with magnetic fields, acoustic fields, and electric fields. Dielectrophoretic levitation is the 3-D spatial confinement of a single particle, where the gravitational or buoyant forces are balanced by the DEP force. Therefore it offers the means to study the polarization response of single particles with much improved accuracy.

Early work on the DEP levitation system indicates that it can be successfully applied for biological cells with improved accuracy over other methods[19,20]. However, it is limited to the frequency region (usually from several kHz to tens of MHz) where biological cells experience a relatively strong positive DEP force. The polarization response in the low frequency region, where the cells experience a negative DEP force, still remains to be fully investigated and is important for understanding the influence of surface phenomena on the polarization response.

1.6 Thesis Outline

In this thesis, a dielectrophoretic levitation system has been modified and improved to achieve precise measurement of both positive and negative DEP spectra. In addition,

a new scheme has been proposed and implemented to measure the effective surface charge of biological cells which is in principle proved to be more accurate than the conventional electrophoresis method. Some technical aspects for achieving the above measurements have also been addressed. Experiments on plant protoplasts for various medium conditions have been conducted. Based on the experimental results and suitable theoretical cell model, several cellular parameters have been derived and some underlying polarization mechanisms discussed.

Chapter 2 provides a review of some existing techniques for measurements of DEP spectra of biological cells. This is followed, in Chapter 3, by discussions of the relevant dielectric polarization mechanisms. Chapter 4 contains a detailed description of the cell levitation system, DEP and EP (electrophoresis) measuring schemes, including image processing and control algorithms. Chapter 5 describes the experiment procedure, error analysis, and data correction methods. The DEP spectra of *Canola* protoplasts under various conditions and derivation of cellular parameters are presented in Chapter 6. Chapter 7 includes conclusions and suggests possible directions for further work.

CHAPTER 2

DIELECTROPHORESIS OF BIOLOGICAL CELLS

As mentioned earlier, dielectrophoresis can be used to determine the frequency-dependent polarization spectra of biological cells. Theoretically, this measured polarization response can not only provide valuable insights into the various frequency-sensitive polarization response mechanisms of the cells but may also facilitate the characterization of the cells. Practically, the polarization spectrum may be used for "fingerprinting" various kinds of cells including normal and "diseased" cells.

The first application of dielectrophoresis to living cells was reported by Pohl and Hawk[18]. They first successfully collected yeast cells using a pin-plate electrode geometry and subsequently "yield spectra" (collection rate at the electrode surfaces *vs.* frequency) were obtained which reflect the excess polarization spectra in a certain way. The "yield spectra" were obtained by observing an electrode through a microscope and estimating, via time-sequenced photographs for each measurement frequencies, the rate at which the cells were collected at the electrode. These spectra were compared for cells of varying age, and treatment (such as exposure to heat, chemical agents, and ultraviolet radiation)[17]. All of these effects showed influence on the yield spectra and therefore on the excess polarizability of the cells.

Following the pioneer work of Pohl *et al* in this area, several other investigators studied the DEP spectra of biological cells with different approaches.

The research group led by Pethig[21] has recently developed an optical technique for measuring the dielectrophoresis of micro-organisms and cells. Their measurements were based on the monitoring of the changes in light absorbancy through a cell suspension as the cells are collected at an interdigitated electrode array. The micro-electrode array was fabricated using standard photo-lithographic techniques. Measurements were performed on lyophilized bacteria and Friend murine erythroleukaemic cells [22]. Although data collections with this method have been claimed to be faster than the earlier "batch" method, it is still time-consuming in that the measurements have to be interrupted at each frequency to allow the reloading of a new suspension.

Kaler *et al*[23] proposed a method of obtaining the DEP spectrum of biological cells using quasi-elastic light scattering, in which the velocity of the particles undergoing dielectrophoresis within a pair of *isomotive* electrodes is measured through the detection and analysis of the doppler frequency shift of the laser light scattered by the particles. Experiments were performed on yeast cells. Adamson and Kaler[24] developed a stream-centred DEP system, in which a narrow sample stream suspended within a larger sheath was injected between a pair of isomotive electrodes and the deflection of the cell stream resulting from dielectrophoresis was detected using a linear photodiode array. Tests were performed on 5-μm DVB microspheres.

Those methods described above are all based on the measurements on cell suspension. The measured quantities (collection rate, optical absorbancy, velocity, and deflection), while ultimately related to the DEP force, do not necessarily exhibit a linear dependence The DEP force is also affected by such complicating factors as fluid viscosity, fluid

stirring and perturbation due to the mass movement of the particles. In addition, particle-particle interactions also introduce error in the data thus obtained.

However, this situation was improved when Kaler and Pohl[19] investigated the behaviour of single yeast cells under the action of opposing gravitational and dielectrophoretic forces by dynamically levitating individual cells. This balancing technique, although through manual adjustment, for the first time, permitted the direct measurement of the DEP force on single cells so that a straightforward comparison of theoretical predictions and experimental measurements can be made. By optically detecting the position of the levitated cell (particle), Kaler and Jones[20] reported a feedback-controlled levitation system which can measure the polarization response of single cells. Their measurements, however, were limited to the frequency region where the particle or cell exhibits a relatively strong positive DEP response. It is known that biological cells also exhibit negative DEP responses in the low frequency region and it has been suggested[1] that the polarization responses in the low frequency region are dominated by the cell surface properties. Few studies have been carried out to investigate the negative DEP responses of biological cells. Although Pohl *et al*[25] observed positive and negative DEP responses for the first time using a cylindrical electrode geometry chamber and later Adamson and Kaler[24] developed the stream-centred DEP system which also allowed the observation of deflection due to the negative DEP force, their observations are qualitative and still based on the measurements of movement induced by the DEP force. Marszalek *et al*[26] extended their investigation of cell DEP responses to the negative DEP region, but their results were also based on the qualitative

observations of horizontal drift of a cell sedimenting between a pair of long vertically mounted parallel cylinder-plate type electrodes.

Thus far no quantitative study has been carried out on the low frequency DEP responses of biological cells, due to the limitations addressed above. The objective of this investigation was to develop a technique to obtain a complete and accurate DEP response (DEP spectra) of individual model biological cells over a wide frequency range, and then with these DEP spectra to study the various polarization mechanisms of the cells and to reveal some important electrical characteristics of biological cells.

CHAPTER 3

THEORY

3.1 General Relaxation Theory

The dielectric response of a material to an electric field involves the physical displacement of charges, whose kinetics determine the frequency dependence of the bulk properties. When the frequency of the applied field is sufficiently high such that the induced displacement can no longer keep up to the changing field, a relaxation process can be observed in the form of polarization dispersion. Typically, the relaxational effects are described by first-order differential equations that lead to single time constant responses. However, in some real physical and biological materials, several relaxation processes may occur in parallel, and hence the total electrical response of the material in such a case may be characterized by several time constants. As long as these time constants are well separated, each relaxation process can be treated separately as single relaxation processes. In the simplest case, the polarization of a sample will relax toward the steady state as a first-order process characterized by a relaxation time τ. The dielectric response of such a first-order system in the frequency domain can be expressed as

$$\underline{\varepsilon} = \varepsilon_\infty + \frac{(\varepsilon_s - \varepsilon_\infty)}{1 + j\omega\tau} \tag{3.1}$$

where ε_∞ now refers to the permittivity at infinite frequencies due to the electronic polarizability and ε_s is the static permittivity of the material. Separating Eq.(3.1) into real and imaginary parts yields:

$$\underline{\varepsilon} = \varepsilon' - j\varepsilon'' \tag{3.2}$$

$$\varepsilon' = \varepsilon_\infty + \frac{\varepsilon_s - \varepsilon_\infty}{1 + (\omega\tau)^2}, \quad \varepsilon'' = \frac{(\varepsilon_s - \varepsilon_\infty)\omega\tau}{1 + (\omega\tau)^2} \tag{3.3}$$

The relaxation process described by Eq.(3.1) is characteristic of a Debye type relaxation[17]. Figure 3.1 illustrates the permittivity spectra for an Debye type relaxation.

3.2 Dielectrophoresis

Non-uniform electric fields can exert force on polarizable dielectric particles. This effect, known as dielectrophoresis, can be used to study the dielectric properties of the particles.

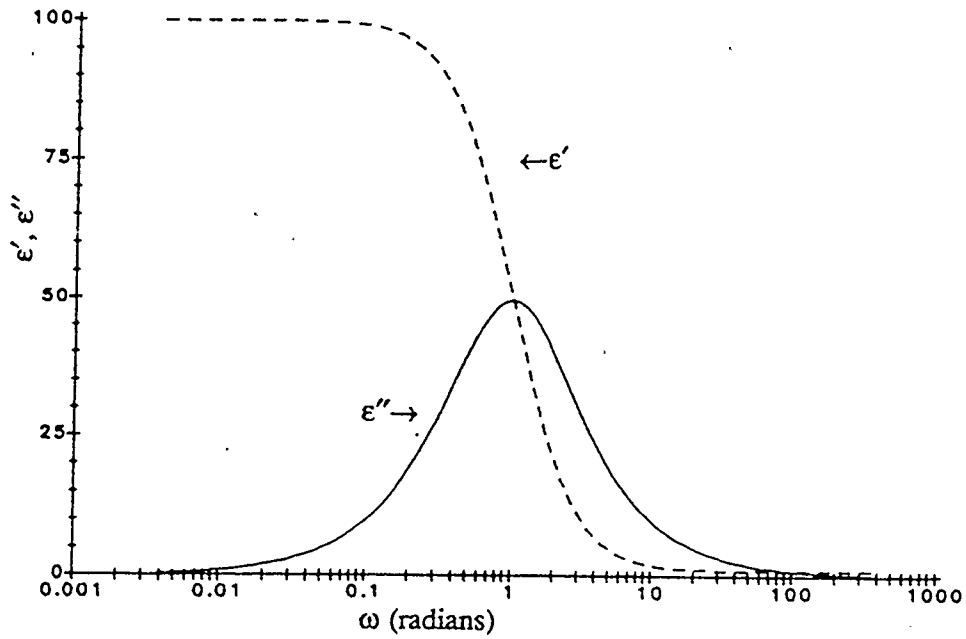

Figure 3.1. Relative permittivity vs. radian for Debye type relaxation ($\tau = 1$)

A neutral particle under the influence of an external electric field $\boldsymbol{E}_0$ is polarized, creating a local molecular charge separation (or imbalance). This separation, or polarization may be represented by an equivalent dipole moment $\boldsymbol{P}_{eff}$, which can be visualized as two opposite charges $+Q$ and $-Q$, separated by distance d. If the applied field is uniform, then the electrostatic forces on each end of the dipole are in opposing direction and of equal magnitude, in other words, the net force on the particle is zero. However, if the applied field is non-uniform then there will be a net force acting on the particle in the direction of the field gradient. This dielectrophoretic force can be expressed as[17]

$$\boldsymbol{F}_{DEP} = (\boldsymbol{P}_{eff} \cdot \nabla)\boldsymbol{E}_0 \qquad (3.4)$$

where $\boldsymbol{P}_{eff}$ is the induced effective dipole moment of the particle. $\boldsymbol{E}_0$ is the local field in the vicinity of the particle.

3.2.1 The DEP Force and Polarization Spectra for Homogeneous and Shelled Spheres

The Homogeneous Spherical Model

For a homogeneous ideal dielectric sphere of radius R, the induced effective dipole moment ($\boldsymbol{P}_{eff}$) can be expressed as[27]

$$\boldsymbol{P}_{eff} = 4\pi R^3 \varepsilon_1 \left(\frac{\varepsilon_2 - \varepsilon_1}{\varepsilon_2 + 2\varepsilon_1}\right) \boldsymbol{E}_0 \qquad (3.5)$$

where ε_1 and ε_2 are the permittivities of the suspending medium and the sphere, respectively. Using Eq.(3.4), the DEP force becomes

$$\begin{aligned} \boldsymbol{F}_{DEP} &= (\boldsymbol{P}_{eff} \cdot \nabla)\, \boldsymbol{E}_0 \\ &= 2\pi R^3 \varepsilon_1 \left(\frac{\varepsilon_2 - \varepsilon_1}{\varepsilon_2 + 2\varepsilon_1}\right) \nabla E_0^2 \end{aligned} \qquad (3.6)$$

One should note that the induced dipole moment $\boldsymbol{P}_{eff}$ in Eq.(3.5) is derived for the uniform field case. For a non-uniform field, in addition to dipole, higher-order multipolar contributions (e.g. quadrupole, octupole, etc.)[28] would also be induced. However, as long as the dimension of the non-uniformity is comparable to that of the particle, these higher-order moments can be neglected without significant error..

For a lossy homogeneous sphere immersed in an Ohmic medium, i.e., having finite conductivities of σ_2 and σ_1, respectively, and with an ac field applied, the time-average DEP force can be expressed as[29]

$$\langle \boldsymbol{F}_{DEP} \rangle = 2\pi R^3 \varepsilon_1 \, Re\left[\frac{\underline{\varepsilon}_2 - \underline{\varepsilon}_1}{\underline{\varepsilon}_2 + 2\underline{\varepsilon}_1}\right] \nabla E_{rms}^2 \tag{3.7}$$

where $\underline{\varepsilon}_2 = \varepsilon_2 - j\sigma_2/\omega$, $\underline{\varepsilon}_1 = \varepsilon_1 - j\sigma_1/\omega$ are the complex permittivities of the sphere and the medium. E_{rms} refers to the root mean squared value of the electric field intensity. For simplicity Eq.(3.7) is often stated as

$$\langle \boldsymbol{F}_{DEP} \rangle = 2\pi R^3 \varepsilon_1 \, Re[\underline{K}_e] \, \nabla E_{rms}^2 \tag{3.8}$$

where the factor

$$\underline{K}_e = \frac{\underline{\varepsilon}_2 - \underline{\varepsilon}_1}{\underline{\varepsilon}_2 + 2\underline{\varepsilon}_1} \tag{3.9}$$

represents the dimensionless frequency-dependent effective or excess polarizability of the particle. Substituting these complex permittivities into $\underline{K}_e$, we obtain

$$\underline{K}_e = K_\infty + \frac{K_s - K_\infty}{1 + j\omega\tau} \tag{3.10}$$

where

$$K_\infty = \frac{\varepsilon_2 - \varepsilon_1}{\varepsilon_2 + 2\varepsilon_1}, \quad K_s = \frac{\sigma_2 - \sigma_1}{\sigma_2 + 2\sigma_1}, \quad \tau = \frac{\varepsilon_2 + 2\varepsilon_1}{\sigma_2 + 2\sigma_1} \tag{3.11}$$

From the above we know that it is a typical Debye type relaxation process with relaxation time constant of τ. The high-frequency limit is controlled by the permittivities:

$$\lim_{\omega \to \infty} Re[\underline{K}_e] = K_\infty = \frac{\varepsilon_2 - \varepsilon_1}{\varepsilon_2 + 2\varepsilon_1} \tag{3.12}$$

while the low-frequency limit is controlled by the conductivities:

$$\lim_{\omega \to 0} Re[\underline{K}_e] = K_s = \frac{\sigma_2 - \sigma_1}{\sigma_2 + 2\sigma_1} \tag{3.13}$$

Figure 3.2 shows an example of the frequency dependence of the real part of the effective polarizability, or DEP spectrum, for a homogeneous sphere.

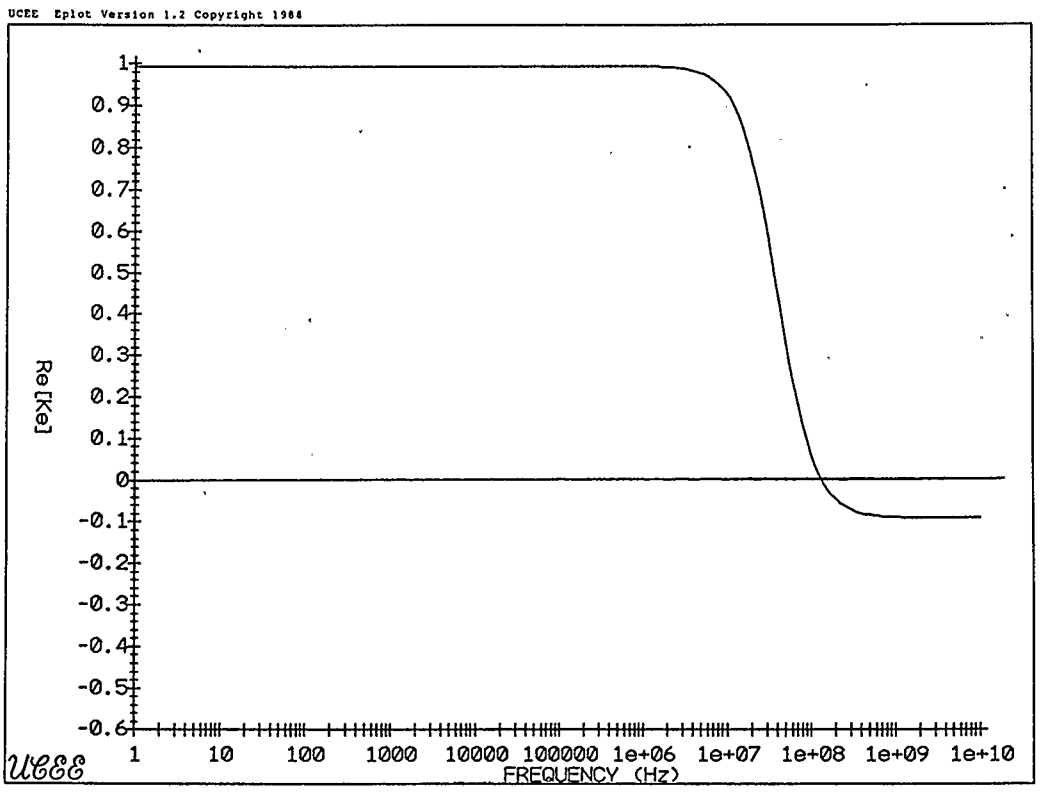

Figure 3.2. An example of DEP spectrum of a lossy homogeneous spherical particle where σ_1 = 10 μS/cm, σ_2 = 5000 μS/cm, $\varepsilon_1 = 80\varepsilon_0$, $\varepsilon_2 = 60\varepsilon_0$.

It is apparent that for Re[$\underline{K}_e$] > 0 the DEP force is positive, i.e., directed so as to impel the particle into the region of the field intensity maxima. This is the case of positive DEP. If, on the other hand, Re[$\underline{K}_e$] < 0, then the particle is pushed into the region of electric field minimum. This is referred to as negative DEP.

The Shelled Spherical Model

For a shelled spherical particle as shown in Figure 3.3, the dielectric response of the particle can be represented by an equivalent homogeneous sphere of radius $R + d$ and complex permittivity $\underline{\varepsilon}_{2eff}$[30], where

$$\underline{\varepsilon}_{2eff} = \varepsilon_2 \left[\frac{a^3 + 2\underline{K}_e(\underline{\varepsilon}_2, \underline{\varepsilon}_m)}{a^3 - \underline{K}_e(\underline{\varepsilon}_2, \underline{\varepsilon}_m)}\right] \tag{3.14}$$

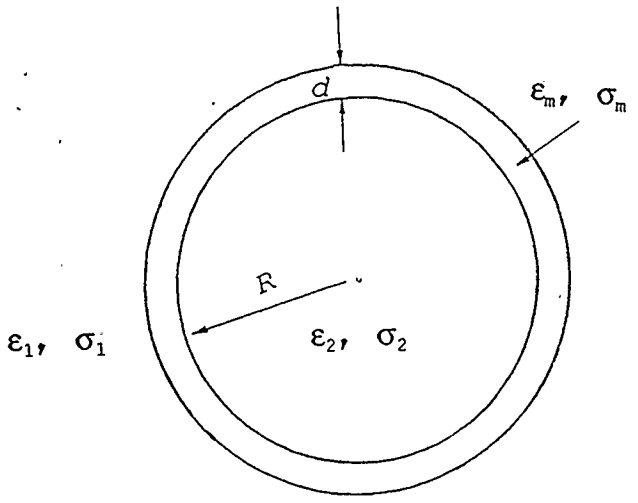

Figure 3.3. A single shelled sphere that represents a biological cell

Here, $\underline{\varepsilon}_m = \varepsilon_m - j\sigma_m/\omega$, $a = (R + d)/R$, and $\underline{K}_e$ is the same complex excess polarizability function as defined in Eq.(3.9). The DEP force expression is the same as Eq.(3.7), except that $\underline{K}_e$ is here given by

$$\underline{K}_e(\underline{\varepsilon}_{2eff}, \underline{\varepsilon}_1) = \frac{\underline{\varepsilon}_{2eff} - \underline{\varepsilon}_1}{\underline{\varepsilon}_{2eff} + 2\underline{\varepsilon}_1} \tag{3.15}$$

If we substitute the following quantities ε_1, ε_2, ε_m, σ_1, σ_2, σ_m, R, and d into Eqs.(3.14) and (3.15), the latter will become quite complicated, hence obscuring the direct contributions of each of these quantitiess to the frequency-dependent Re[$\underline{K}_e$], i.e. the theoretical DEP spectrum. In order to find the relations rigorously without making any approximations to the equations, we calculated and plotted several groups of Re[$\underline{K}_e$]~f curves. For each group only one parameter was varied and others were kept constant and assigned with typical values available for biological cells, especially plant protoplasts in our case. A program was written to calculate Re[$\underline{K}_e$] for each discrete frequency value. There is no need to calculate the DEP spectra for different values of ε_1, the permittivity of the suspending medium because the practical medium used in experiments is always aqueous solution (8% sorbitol) and has a relative permittivity value of 80. For parameters ε_m and d, we introduced a specific membrane capacitance $C_m = \varepsilon_m/d$ to account for the effects of both. Figure 3.4 shows the calculated theoretical DEP spectra for the different conditions. For all the plots, except the varying parameter, all the other parameters were assigned values typical for plant protoplasts as follows:

$\varepsilon_1 = 80\varepsilon_0$ (water), $\varepsilon_2 = 60\varepsilon_0$[20], $\varepsilon_m = 2.5\varepsilon_0$[31], $C_m = 0.5$ μF/cm^2[31], $\sigma_1 = 10$ μS/cm, $\sigma_2 = 5000$ μS/cm, $\sigma_m = 0.1$ μS/cm, and $R = 17.5$ μm.

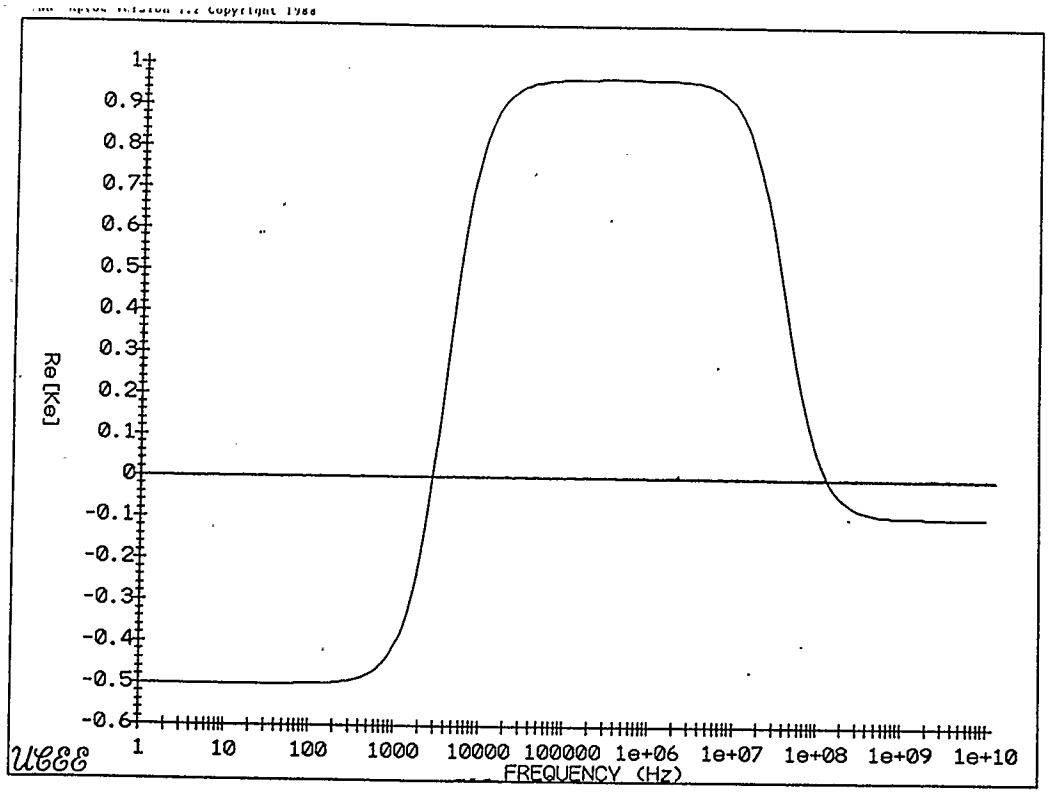

Figure 3.4a. A typical theoretical DEP spectrum for the shell spherical model

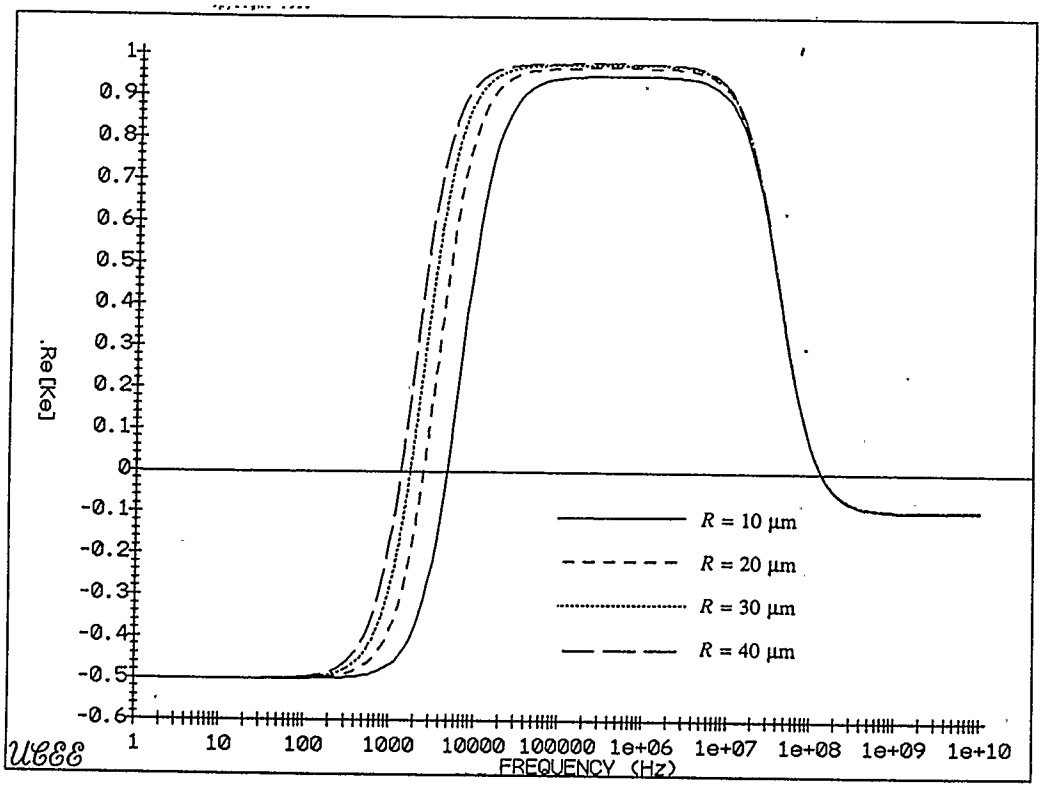

Figure 3.4b. R dependence of DEP spectra for the shell spherical model

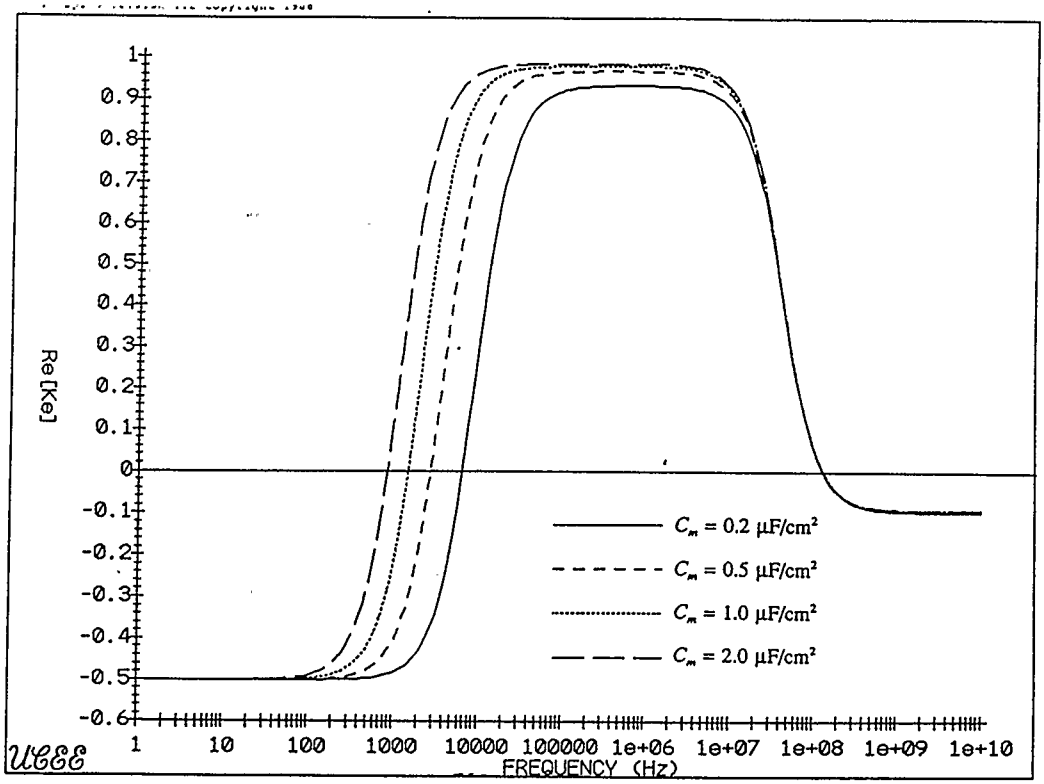

Figure 3.4c. C_m dependence of DEP spectra for shell spherical model

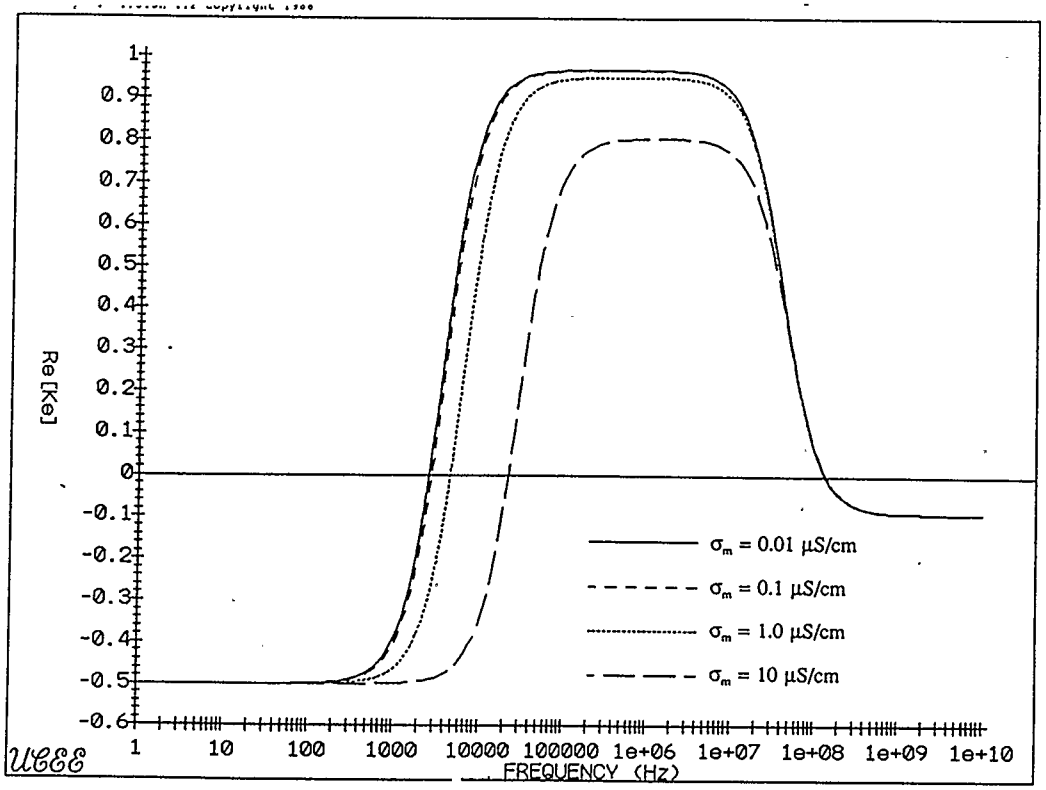

Figure 3.4d. σ_m dependence of DEP spectra for the shell spherical model

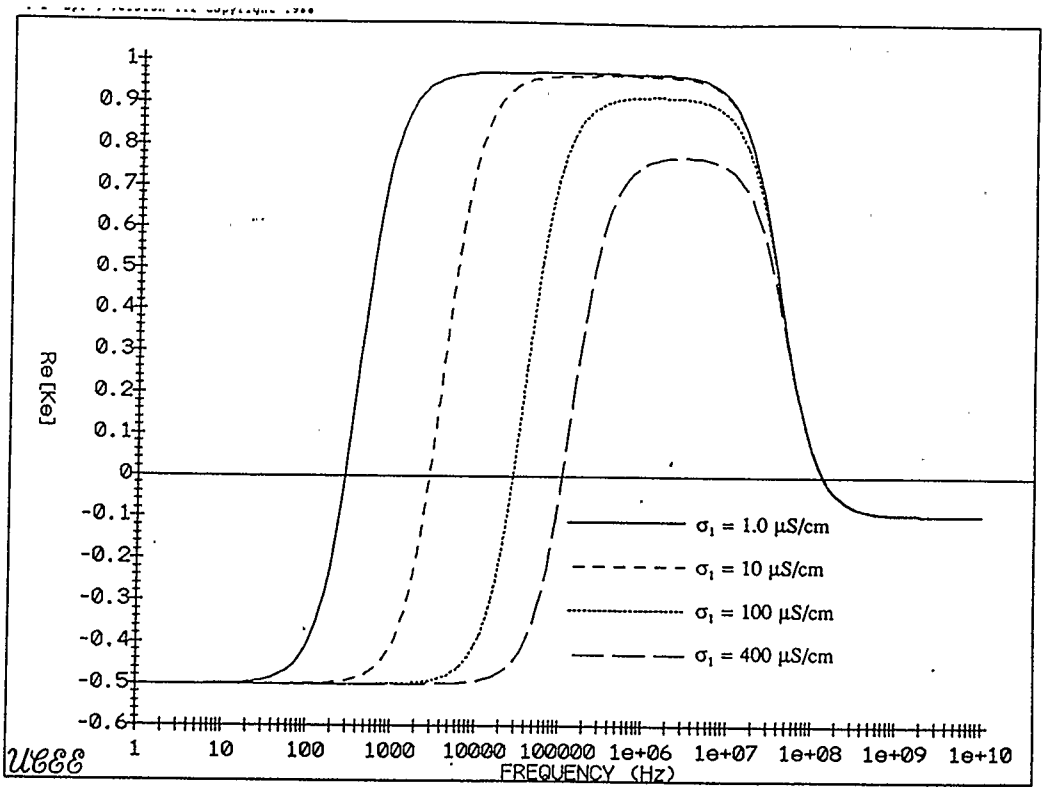

Figure 3.4e. σ_1 dependence of DEP spectra for the shell spherical model

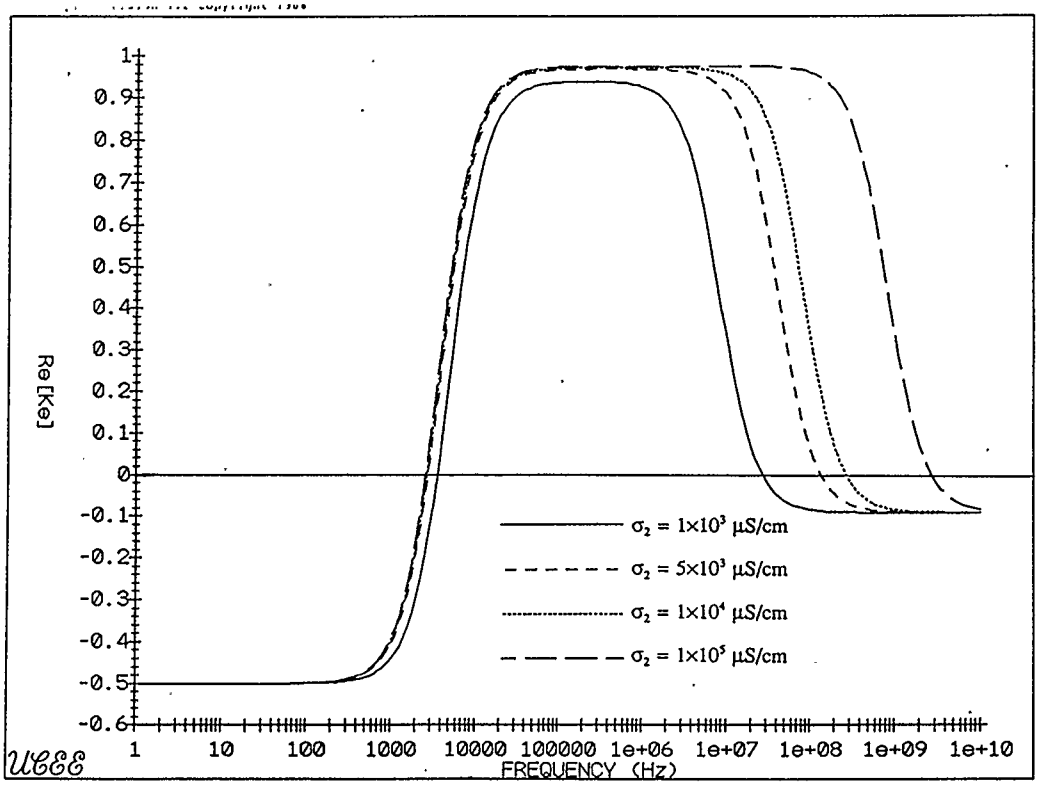

Figure 3.4f. σ_2 dependence of DEP spectra for the shell spherical model

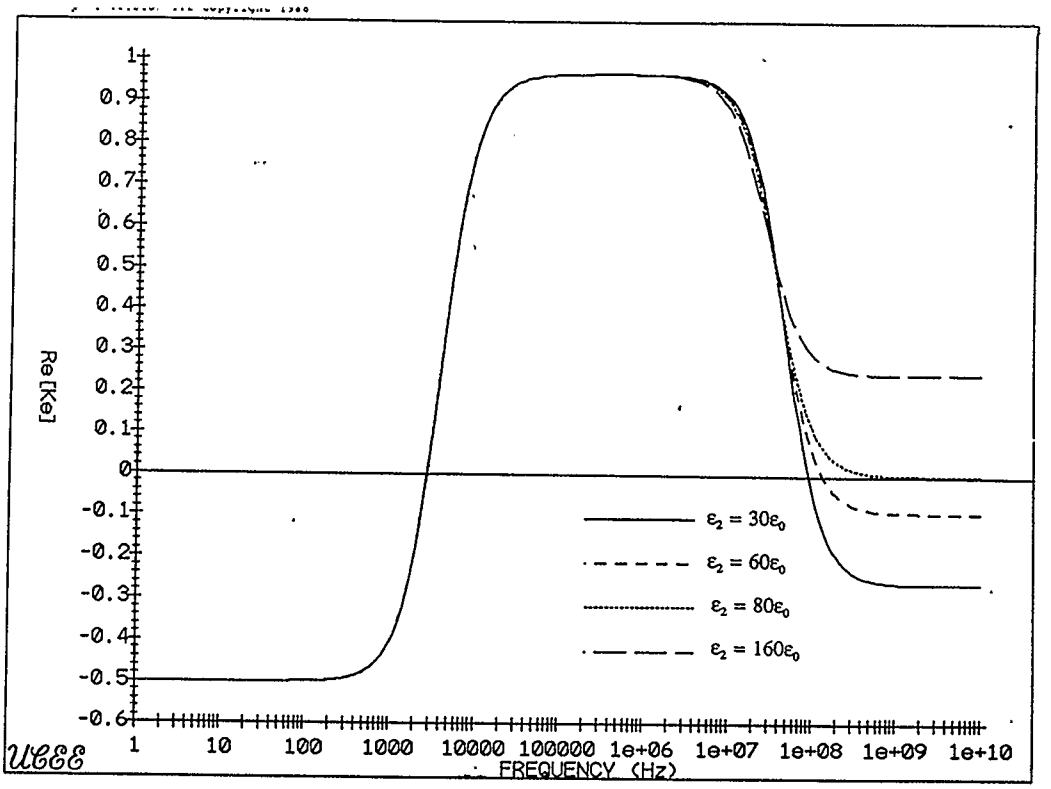

Figure 3.4g. ε_2 dependence of DEP spectra for the shell spherical model

From the theoretical DEP spectra we can see that there are two polarization dispersions. These can be physically interpreted as following: Above the first relaxation frequency region (or when f > ~ 20 kHz in Figure 3.4a), the membrane appears transparent to the externally applied field. Hence the field effectively sees a homogeneous conductive sphere (of ε_2, σ_2) immersed in a fluid medium (of ε_1, σ_1). Therefore, the approximate relaxation time in the high frequency region can be expressed by Eq.(3.11). The high-frequency amplitude (f > ~ 300 MHz in Figure 3.4a) is controlled by ε_1 and ε_2 (see Eq.(3.12)), and the mid-frequency amplitude is controlled by σ_1 and σ_2 (see Eq.(3.13)). That is why the Re[$\underline{K}_c$] in the mid-frequency region tends to approach

1 (because $\sigma_2 \gg \sigma_1$). In the low frequency region ($f <$ ~ 300 Hz) the field can not penetrate the cell membrane, hence the particle behaves like an insulator and the amplitude of Re[$\underline{K}_e$] is determined by Eq.(3.13). That is why its value converges to -0.5. In the upward transition region (1 KHz ~ 20 KHz) , the membrane begins to play an important role.

It is well known that biological cells have membranes of about 5nm in thickness. The cell membranes are generally structures composed mainly of a bilayer of long-chain lipid molecules which normally have very low conductivity[31]. The interior of biological cells, the cytoplasm, have very high conductivity and can be approximated by a conductive homogeneous medium. Therefore, the above shelled model can provide an approximation to the biological cell and we can expect a similar dielectric relaxation behaviour or DEP spectra to those theoretical plots. By measuring the frequency-dependent Re[$\underline{K}_e(f)$] spectra of real cells and resorting to the above theoretical model, one can determine the electrical parameters of various cellular compartments.

3.2.2 Derivation of Cellular Parameters

In order to extract cellular parameters from experimentally obtained DEP spectra, it is possible to fit the modelled spectra (such as those in Figure 3.4) to them. This is done by superimposing frequency responses predicted from a general equation on the experimental data, until the minimum deviation (as seen by eye, or according to some statistical criterion such as Least-Squared-Error regression values) is obtained. For example, it is apparent from the above theoretical spectra, specifically Figure 3.4f, that the conductivity of the interior of the cell (cytoplasm) σ_2 determines predominantly the

relaxation time in the high frequency region. Therefore, the conductivity of the cytoplasm can be easily determined by fitting this part of the spectrum.

Although the "fitting procedure" mentioned above may give a satisfactory explanation for the data, it is clumsy[12]. In addition, unless reasonable values for many (particularly the membrane) parameters can be assumed, the number of unknown is too large to allow unambiguous assignment of values to any of them. This situation can be alleviated, at least theoretically, by taking spectra at several different conductivity values. However, simultaneous fitting of several spectra represents a difficult computation that has yet to be carried out[12]. These complications result from using equations that can not be solved analytically.

The general equations (3.14) and (3.15) may be simplified by the use of reasonable approximations based on the properties of biological cells. These new equations deal with the most significant point, i.e., the cross-zero frequency, f_0, and lend themselves to analytical solutions, provided that measurements are made over a wide range of medium conductivities. The derivation of such an analytical expression is presented here to determine the specific membrane capacitance C_m.

For present purposes, the shell is intended to represent the cell membrane in which case $d/R \ll 1$ and $\sigma_m \approx 0$. Then $a^3 \approx 1 + 3(d/R)$ and Eq. (3.14) becomes

$$\underline{\varepsilon}_{2eff} \approx C_m R \left[\frac{j\omega \tau_2 + 1}{j\omega (\tau_m + \tau_2) + 1}\right] \tag{3.16}$$

Here, $\tau_2 = \varepsilon_2/\sigma_2$ and $\tau_m = \varepsilon_m R/d\sigma_2 = C_m R/\sigma_2$ are time constants. Substituting it into Eq.(3.15), we obtain

$$\underline{K}_e(\omega) = \frac{\omega^2(\tau_1\tau_m - \tau_2\tau'_m) - 1 + j\omega(\tau'_m - \tau_1 - \tau_m)}{2 - \omega^2(\tau_2\tau'_m + 2\tau_1\tau_m) + j\omega(\tau'_m + 2\tau_1 + 2\tau_m)} \tag{3.17}$$

where $\tau'_m = C_m R/\sigma_1 = \varepsilon_m R/\sigma_1 d$ and $\tau_1 = \varepsilon_1/\sigma_1$. In our case, attention is restricted to the low-frequency cross-zero point, in the vicinity of which $\underline{K}_e(\omega)$ can be reasonably approximated as follows:

$$\underline{K}_e \approx \frac{j\omega(\tau'_m - \tau_1 - \tau_m) - 1}{j\omega(\tau'_m + 2\tau_1 + 2\tau_m) + 2} \tag{3.18}$$

If we let $\mathrm{Re}[\underline{K}_e] = 0$, we obtain

$$\omega_0^2(\tau'_m - \tau_1 - \tau_m)(\tau'_m + 2\tau_1 + 2\tau_m) \approx 2 \tag{3.19}$$

or

$$\omega_0^2(\tau'^2_m + \tau_1\tau'_m + \tau_m\tau'_m - 2\tau_1^2 - 4\tau_1\tau_m - 2\tau_m^2) \approx 2 \tag{3.20}$$

For biological cells it is reasonable to assume $\varepsilon_1 \ll \varepsilon_m R/d$ or $\tau_1 \ll \tau'_m$. Then we have

$$\omega_0^2(\tau'^2_m + \tau_m\tau'_m - 2\tau_m^2) \approx 2 \tag{3.21}$$

Since $\sigma_1 \ll \sigma_2$, i.e. $\tau_m \ll \tau'_m$, we may approximate

$$f_0 \approx \frac{\sigma_1}{\sqrt{2\pi RC_m}} \tag{3.22}$$

From the above we can see that the membrane capacitance can be approximately determined by the above relation.

3.3 Dielectric Polarization Mechanisms

When a polarizable matter is exposed to an electric field, several polarization mechanisms will contribute to its dielectric response. These are electronic, atomic, dipolar, interfacial, and counterion polarizations. The first three occur on a molecular scale, while the last two depend upon the gross or macroscopic structure.

Electronic polarization arises from the slight distortion of the centres of positive and negative charge of the atoms due to the applied electric field. When the frequency of the applied field is sufficiently high that the distortion can no longer keep up to the changing field, a polarization dispersion can be observed. For the electronic polarization mechanism, the dispersion is observed in the optical to ultraviolet frequency ranges and therefore does not concern us here. For atomic polarization, which arises from the shift of differently charged atoms with respect to each other, its dispersion is observed in the infrared frequencies and therefore is beyond the range of our instrumentation.

Dipolar (orientational) polarization arises from the orientational response of molecules or parts of molecule to the externally applied field[17]. Molecules composed of several atoms may possess permanent dipoles. They tend to respond to an external electric field by realignment so as to reduce their potential energy. Examples of such dipolar molecules are HF, NO; H_2O and chlorobenzene. The dielectric relaxation process due to dipolar polarization can be described as Debye type process of Eq.(3.1). The time constant for dipolar relaxation range from picoseconds for small dipolar molecules such

as water, to microseconds for large globular proteins[1].

3.3.1 Interfacial (Maxwell-Wagner) Polarization

Interfacial polarization, as its name implies, arises due to the charge accumulation occurring at the interfaces of differing materials making up a heterogenous dielectric. Interfacial effects can dominate the dielectric properties of colloids, emulsions and cell suspensions. As discussed in the previous section, the high frequency polarization behaviour of the homogeneous and shelled spherical particles immersed in a suspending medium arise exclusively from the interfacial polarization mechanism.

3.3.2 Counterion Polarization

Another major class of dielectric phenomena arises from the ionic diffusion in the electrical double layers induced by and adjacent to the charged surface. Many investigators have reported the counterion polarization effects in systems that contain the charged surfaces: emulsions, suspensions of charged polystyrene spheres, microorganisms, and long-chain macromolecular polyions such as DNA. Dielectric polarization effects due to the counterion polarization are difficult to analyze rigorously, since they involve coupled electrical and hydrodynamic phenomena in the double layers surrounding the particle that are governed by nonlinear equations[1]. Schwarz[32] first proposed the bound-ion layer theory that successfully accounted for the dielectric dispersion observed in suspension of colloidal particles in electrolyte solution. He considered the case of a spherical particle of radius R with counterion surface charge density ρ_0, in which the thickness of the electrical double layer is much less than the particle diameter. The frequency-dependent surface conductivity was found by solving the electrodiffusion

equation to obtain the effective permittivity $\underline{\varepsilon}_p$ of the particle:

$$\underline{\varepsilon}_p = \varepsilon_b + \frac{1}{1 + j\omega\tau_{bl}} \cdot \frac{e_0^2 \rho_0 R}{\varepsilon_0 k T} \tag{3.23}$$

where ε_b is the permittivity of the bulk material of the particle, and e_0 is the charge of the counterion. The relaxation time τ_{bl} is proportional to the square of the radius:

$$\tau_{bl} = \frac{\varepsilon_0 R^2}{2 u_b k T} \tag{3.24}$$

where u_b is the surface mobility of the counterion. It is expected that u_b will be smaller than the mobility of the ions in bulk solution. Without specifying the nature of ionic binding, Schwarz suggests that the surface mobility would differ from that in the solution, u_0, by having an energy barrier, ξ, of electrostatic origin:

$$u_b = u_0 e^{\frac{-\xi}{kT}} \tag{3.25}$$

Moreover, it is thought possible that a distribution of ξ (activation energy) values would causes a distribution of relaxation times, such as is observed.

Several investigators have recently criticized Schwarz's model for its neglect of the ionic diffusion in the bulk electrolyte near the charged surface, which they argue gives rise to the polarization. Dukhin[33], Fixman[34], and Chew and Sen[35] have done important work on this problem; Mandel and Odijk[36] have published an excellent review of this newer work.

In their theories, Chew, Sen, and Fixman abandoned the model of a tightly bound layer of charges assumed by Schwarz. They assumed instead the Guoy-Chapman model

of a diffuse double layer in which the ionic charge distribution is given by the Boltzmann distribution in terms of the potential, which is related in turn to the charge distribution by Poisson's equation. Some of these authors also considered hydrodynamic effects (electrically induced fluid flow). Finally, using various approximations, these authors solved the resulting coupled fluid electro-mechanical problem.

Recently, Grosse[37,38] proposed a simplified model that preserves important features of these latter theories yet can be exactly solved. The model assumes that the counterion layer is thin and it contains only ions that are opposite in sign to that of the fixed charges on the particles, and the counterions can exchange freely only with ions of the same sign in the bulk electrolyte. The surface conductivity G_s was assumed to be high. In this model, when an electric field is applied, the ions in the system will redistribute under the influence of both the field and diffusion. Grosse obtained a set of coupled differential equations for the ion concentrations and current densities. The solution of these equations yields a broad, asymmetrical, low-frequency dispersion in the permittivity of the particle. The time constant τ of this dispersion is similar to that derived by Schwarz:

$$\tau \propto R^2 / D \tag{3.26}$$

but now D is the diffusion coefficient of the ions in the bulk electrolyte.

Grosse's model lends itself to a simple physical interpretation of the phenomenon: the large dielectric increments of the charged spheres (such as polystyrene) are direct consequences of the asymmetrical charge distribution on the surface of the particle. The motion of an ion in the bulk electrolyte near the particle depends greatly on whether its sign is the same or opposite to that of the ions in the counterion layer. Ions of the same

sign can enter the counterion layer, and their charge is quickly conducted to the opposite side of the particle; those of opposite sign are excluded from the layer and must travel around the particle in the bulk electrolyte surrounding the particle. Thus, for an ion in the bulk electrolyte, the particle acts as either a good conductor or an insulator, depending on whether its charge is the same or opposite to that of the counterion layer surrounding the particle. In response to an applied electric field, a cloud of charge accumulates in the electrolyte within a Debye length of the particle, which accounts for the large permittivity of the particle.

CHAPTER 4

AUTOMATED DEP AND EP LEVITATION SYSTEM

4.1 Conditions for Dielectrophoretic Levitation

From the DEP force expression we know that in order to measure the Re[$\underline{K}_e(f)$], two approaches can be used. One approach is to apply a constant ac electric field over the measured frequency range while measuring the DEP force. This approach was adopted by most investigators[17,18,21-26] (see Chapter 2). Another approach is to keep the DEP force constant while recording the required field intensities over the frequency range, which is far more precise. The latter idea leads to the DEP levitation approach.

The DEP levitation technique is based on the balance of the gravitational or buoyant force and the DEP force to suspend a particle stably in a fluid of known properties. Hence it offers the means to study the polarization response of single particles. In order to levitate a particle exhibiting the negative DEP, i.e. Re[$\underline{K}_e$] < 0, it requires a local minimum in the electric field intensity. Such minima are allowed in divergence- and curl-free electrostatic fields[39]. Thus passive levitation of particles, droplets, and bubbles exhibiting the negative DEP is readily achieved with a cusped axisymmetric electric field[39,40]. The field for such a levitation system is designed to levitate particles without any need for servo control by creating a potential well that is strong enough to counteract the gravitational or buoyant force acting on the suspended object. Passive levitation has been exploited as a means for precise measurement of the dielectric

constant of homogeneous insulating particles by Kallio and Jones[41] using the cusped axisymmetric electric field shown in Figure 4.1

To levitate particles exhibiting positive DEP ($Re[\underline{K}_e] > 0$) in a similar fashion would require that a field intensity maximum exist at an isolated point in the space detached from the electrode surfaces. However, such maxima are not allowed in the divergence- and curl-free electrostatic fields[39]. Instead, the stable levitation can be achieved by resorting to the active feedback-control of the particle position. A simple implementation of this scheme was used by Kaler and Pohl[19] who performed the measurements on yeast cells. A computer-controlled active DEP levitation was first demonstrated by Jones and Kraybill[42] who measured the effective dipole moments of metallic particle chains suspended in insulating dielectric oils.

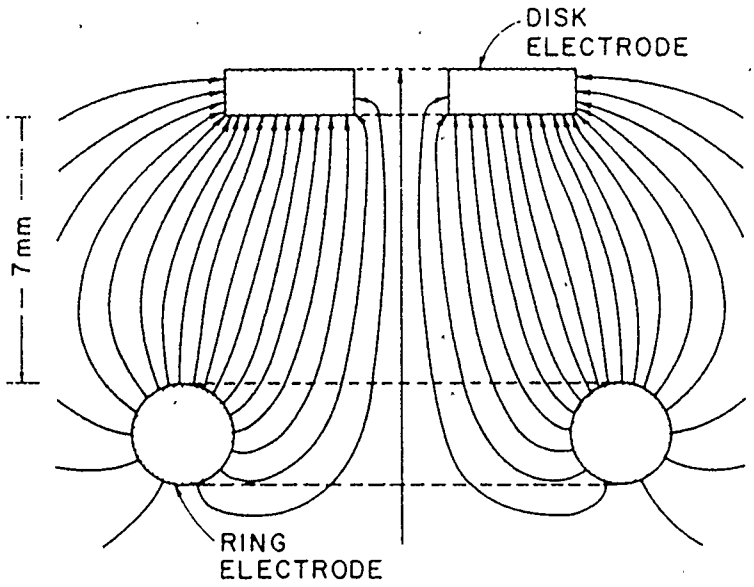

Figure 4.1. Typical electric field plot for ring disk electrodes showing cusped electric field for levitation of air bubble(after Jones and Bliss[39]).

4.2 Levitation and DEP Spectra Measuring Schemes

As mentioned earlier, shelled spherical particle, like biological cell, exhibits positive DEP over a wide frequency range. Therefore only feedback-controlled levitation is applicable in such cases.

4.2.1 The Feedback Controlled Levitation Scheme

The condition required for the stable levitation of a particle experiencing a positive DEP force have been discussed at length by Jones and Kraybill[42]. The particle, assumed to be in equilibrium on the axis in an axisymmetric electric field, must be stable with respect to the radial and axial motions. The radial stabilization is achieved using a focused electric field with the intensity decreasing as the particle moves away from the axis, as in the case of cone-plate electrode configuration of Figure 4.2. In such an

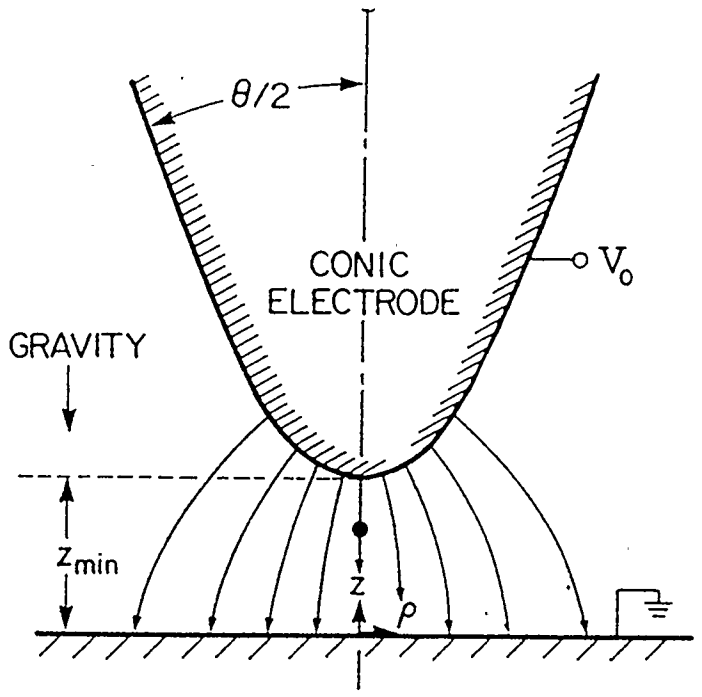

Figure 4.2. Cone-plate electrode structure which produces focused electric field suitable for feedback-controlled DEP levitation when Re[$\underline{K}_e(\omega)$] > 0 (after Kaler and Jones[20]).

electrode structure, the stabilization in the axial direction is achieved by sensing the vertical particle displacements from an equilibrium point and adjusting the levitation voltage to maintain the particle at the preset equilibrium point.

For a spherical particle of radius R and density γ_2 suspended in a medium of density γ_1, the gravitational force F_g acting on the particle is given by:

$$F_g = \frac{4}{3}\pi R^3 (\gamma_2 - \gamma_1) g \tag{4.1}$$

where $g = 9.81$ m/s^2 is the acceleration due to the gravity. For a particle located on the axis and stably levitated at some point z by feedback control of the voltage applied to the electrodes (see Figure 4.2), the DEP force can be equated to the gravitational force.

$$\langle F_{DEP} \rangle = F_g \tag{4.2}$$

Using equation (3.8), (4.1) and (4.2), we obtain

$$Re[\underline{K}_e(f)] = \frac{2|\gamma_2 - \gamma_1| g}{3\varepsilon_1 |\partial E_{rms}^2 / \partial z|} \tag{4.3}$$

The gradient term $|\partial E_{rms}^2/\partial z|$, which depends on the voltage squared and must be known to determine $\mathrm{Re}[\underline{K}_e(f)]$, is ordinarily obtained in a calibration step, where a conducting particle (with $\underline{K}_e(f) = 1$) of known density is levitated in an insulating liquid of known density and dielectric permittivity. However, the electrostatic field solution along the axis $E_z(0,z)$ is analytically well approximated for the cone-plate electrode configuration[42] and given by:

$$E(0, \underline{z}) = \frac{2\,V}{h\,(1 - \underline{z}^2)\,\ln\,[(1 + \underline{z}_{min})\,/\,(1 - \underline{z}_{min})]} \tag{4.4}$$

where $\underline{z} = z/h$, $h = z_{min}/\cos(\theta/2)$, $\underline{z}_{min} = z_{min}/h$ and V is the voltage applied between the conic electrode and the ground plane electrode. For the above axial electric field profile, the expression for $|\partial E_{rms}^2/\partial z|$ is then given by

$$\partial E_{rms}^2\,/\,\partial z\big|_{0,\,z} = -\frac{16\,V_{rms}^2\,\underline{z}}{h^3\,(1 - \underline{z}^2)^3\,\ln^2\,[(1 + \underline{z}_{min})\,/\,(1 - \underline{z}_{min})]} \tag{4.5}$$

Combined with Eq.(4.3), we have

$$Re[\underline{K}_e(f)] = \frac{G}{\varepsilon_1\,f(z)} \cdot \frac{1}{V_{rms}^2(f)} \tag{4.6}$$

where f is the frequency of the applied field, and

$$G = 2|\gamma_2 - \gamma_1|g/3, \quad f(z) = -\frac{16\,\underline{z}}{h^3\,(1 - \underline{z}^2)^3\,\ln^2\,[(1 + \underline{z}_{min})\,/\,(1 - \underline{z}_{min})]} \tag{4.7}$$

In the entire measurement process, the cell is always levitated at a fixed position so that the position function $f(z)$ can be treated as a constant. Therefore, from Eq.(4.6) we know that $\mathrm{Re}[\underline{K}_e(f)]$ is determined reciprocally by the square of the *rms* levitation voltage. During the levitation process, the levitation voltage squared (V_{rms}^2) is recorded for each frequency point as long as the cell is levitated stably at the preset position for a given period of time ($\simeq$ 10 sec).

As mentioned above, the feedback-controlled levitation scheme is only suitable for levitating particles exhibiting the positive DEP. However, biological cells exhibit both

positive and negative DEP responses in different frequency regions. Although both passive and active (feedback controlled) levitations can be used to measure the negative and positive DEP of a single cell, one can not expect an accurate, reliable, and continuous DEP spectrum because of the difficulties of moving the same cell from one electrode chamber to another and the absolute calibration between two different levitation systems. Therefore, a double frequency levitation scheme, which enable both positive and negative DEP measurements, has been proposed and implemented in our system based on the positive DEP feedback-controlled levitation scheme and the cone-plate electrode configuration.

4.2.2 Double Frequency Levitation Scheme

The principle behind the double frequency levitation is to utilize a positive DEP force to balance the negative DEP force and the net gravitational force when levitating in the negative DEP regions, that means two ac voltages of different frequencies f_1, f_2 may be synthesized to achieve this purpose. Figure 4.3 illustrates the double frequency scheme compared to the single frequency scheme. It has been shown (see Appendix) that the mean-square of the sum of two sinusoids is approximately equal to the sum of mean-squares of each sinusoid if their frequencies are well separated. From Eqs.(3.8) and (4.5) we know that the DEP force F_{DEP} is proportional to the mean-square of the applied voltage, therefore we have:

$$\langle F_{syn}(f_1, f_2)\rangle = \langle F_{DEP}(f_1)\rangle + \langle F_{DEP}(f_2)\rangle \tag{4.8}$$

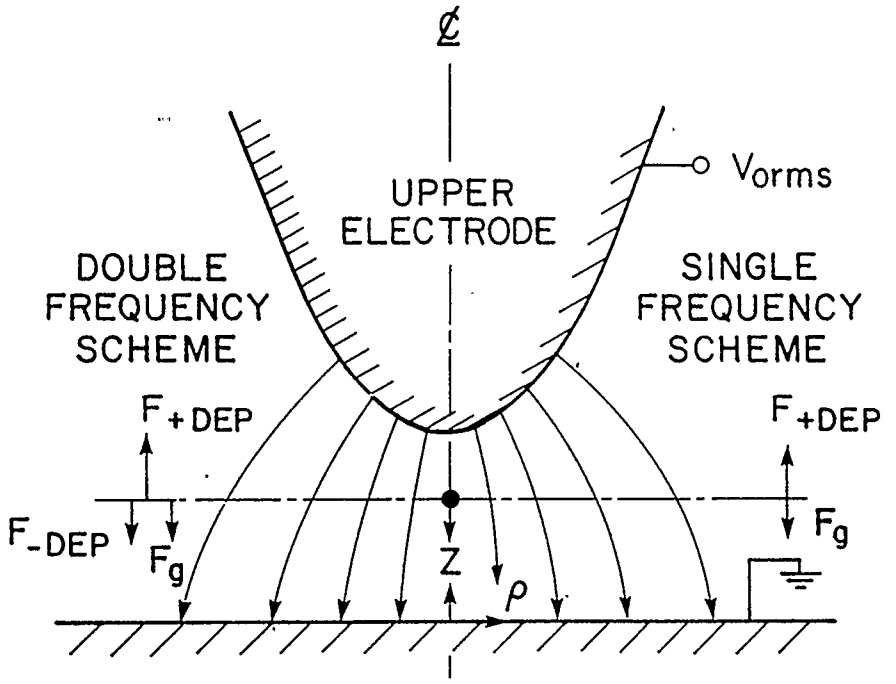

Figure 4.3. Cross-sectional view of the electrode geometry used and comparison of the single and double frequency levitation schemes.

With this superposition relation, the measurement of DEP spectrum is carried out as follows:

The measurement starts from the high frequency end and the positive DEP spectrum in this region (approx. 100 kHz ~ 50 MHz) is obtained by the feedback-controlled levitation with a single frequency voltage. With the frequency scanning down to certain region, the levitation voltage V thus required will increase (as $\mathrm{Re}[\underline{K}_e(f)]$ decreases). When it increases to a certain extent (e.g. 2 volts), the double frequency scheme is invoked. That is, two sinusoidal voltages are summed and applied to the levitation chamber electrodes, one with fixed frequency f_H (where $\mathrm{Re}[\underline{K}_e(f)] > 0$ and near maximum value) and controllable amplitude V_{HC} and the other a scanning frequency f and fixed amplitude

V_f (All the amplitude concerned here are in r.m.s. values). V_{HC} is the levitation voltage of frequency f_H which maintains the cell at the preset position when the fixed voltage V_f of frequency f is also applied. That means:

$$\begin{aligned} F_g &= \langle F_{syn} \rangle = \langle F_{DEP}(f) \rangle + \langle F_{DEP}(f_H) \rangle \\ &= C\{ Re[\underline{K}_e(f)]\ V_f^2 + Re[\underline{K}_e(f_H)]\cdot V_{HC}^2 \} \end{aligned} \tag{4.9}$$

where $C = 2\pi R^3 \varepsilon_1 f(z)$ is a constant. In order to determine the scanning frequency component $\mathrm{Re}[\underline{K}_e(f)]$, a single frequency calibration procedure at frequency f_H is performed, before the invocation of double frequency scheme, to obtain the levitation voltage V_{HS}, that means:

$$F_g = \langle F_{DEP}(f_H) \rangle = C \cdot Re[\underline{K}_e(f_H)]\ V_{HS}^2 \tag{4.10}$$

Using Eqs.(4.9), (4.10), we obtain

$$Re[\underline{K}_e(f)] = \frac{Re[\underline{K}_e(f_H)]\ (V_{HS}^2 - V_{HC}^2)}{V_f^2} \tag{4.11}$$

Combined with Eq.(4.6), we have

$$\begin{aligned} Re[\underline{K}_e(f)] &= \frac{G}{\varepsilon_1 f(z)} \cdot \frac{(V_{HS}^2 - V_{HC}^2)}{V_f^2\ V_{HS}^2} \\ &= \frac{G}{\varepsilon_1 f(z)} \cdot \frac{1}{V_{eq}^2} \end{aligned} \tag{4.12}$$

where

$$V_{eq}^2 = \frac{V_{HS}^2 \cdot V_f^2}{V_{HS}^2 - V_{HC}^2} \tag{4.13}$$

Comparing with Eq.(4.6), we can see that V_{eq} is effectively the equivalent single frequency levitation voltage at frequency f which alone can exert the same force of F_g either upward (for positive DEP) or downward (for negative DEP). Actually, in our system, only single frequency levitation voltages in Eq.(4.6) and the equivalent voltages in Eq.(4.13) are recorded.

In order to obtain the absolute value of Re[$\underline{K}_e(f)$], we have to find the coefficient G in Eqs.(4.6) and (4.12) which is determined by Eq.(4.7), i.e. the mass density difference between the cell and the medium ($\gamma_2 - \gamma_1$). Rather than measuring γ_1 and γ_2 separately, we measured the sedimenting velocity v of the cell and resorting to the well-known Stokes drag equation, which shows that the terminal velocity of a spherical particle of radius R falling in a medium of density γ_1 and viscosity η is given by:

$$v = \frac{2}{9}\frac{(\gamma_2 - \gamma_1)\, g\, R^2}{\eta} \tag{4.14}$$

4.2.3 Electrophoresis Measuring Scheme

As mentioned earlier, most cell types maintain a net negative surface charge at physiological *pH*. A measure of this surface charge can not only provide important information on physiological "state" of the cells such as the conformation of membrane proteins, it also plays an important role in the counterion polarization mechanism. Therefore, it is important to be able to determine quantitatively the magnitude of the net

surface charge.

The surface charge density of a biological cell can be determined through electrophoretic measurement using either a commercially available microelectrophoresis apparatus[14] or a similar system developed in the laboratory. Regardless of the nature of the electrophoretic systems the parameter actually measured is the same: the mean velocity at which the cell sample is translated under the action of a uniform dc electric field. This electrophoretic velocity can then be converted into the electrophoretic mobility, and then the zeta potential and the surface charge density[14]. It is obvious that this kind of dynamic measurement (i.e. velocity) can be easily affected by such factors as fluid viscosity, fluid stirring and perturbation due to cell movement.

Based on the feedback-controlled DEP levitation, a new scheme has been proposed and implemented in our system which enable us to measure quantitatively the magnitude of net charge of the particle. The underlying principle is to use the DEP force to balance the electrophoretic force and measure it in a static way such that the resolution of measurement is not affected by such factors as fluid viscosity, fluid stirring and perturbation due to cell movement. This involves three levitation steps. First, levitate the cell with single frequency voltage at f_H and record the levitation voltage V_{HS}, Secondly, superimpose a constant negative dc offset $-V_{dc}$ and record the levitation voltage V_{H-}, and finally superimpose a positive dc offset $+V_{dc}$ of the same magnitude as $-V_{dc}$ and record the levitation voltage V_{H+}. With these data in hand, the amount of net charge Q_s of the cell can be determined in the following way.

From the description of the above three levitation conditions, we know that the

following three equations hold:

$$\begin{aligned} F_g &= F_{DEP}(f_H) \\ &= C \cdot Re[\underline{K}_e(f_H)]\ V_{HS}^2 \end{aligned} \tag{4.15}$$

$$F_g = F_{DEP}^{+}(f_H) + F_{DEP}^{+}(dc) + E(z) \cdot Q_s \tag{4.16}$$

$$F_g = F_{DEP}^{-}(f_H) + F_{DEP}^{-}(dc) - E(z) \cdot Q_s \tag{4.17}$$

where $E(z)$ is the dc field intensity component at the levitation position z. Since the DEP force is independent of the field polarity, the DEP forces due to the dc offset should be same regardless of its polarity. With Eqs.(4.16) and (4.17), we therefore have:

$$\begin{aligned} Q_s &= \frac{F_{DEP}^{-}(f_H) - F_{DEP}^{+}(f_H)}{2\ E(z)} \\ &= \frac{C \cdot Re[\underline{K}_e(f_H)]\ (V_{H-}^2 - V_{H+}^2)}{2\ E(z)} \end{aligned} \tag{4.18}$$

From Eqs.(4.15) and (4.1) we have

$$C \cdot Re[\underline{K}_e(f_H)] = \frac{4}{3}\pi R^3\ (\gamma_2 - \gamma_1)\ g \cdot \frac{1}{V_{HS}^2} \tag{4.19}$$

Therefore

$$Q_s = \frac{2\pi R^3\ (\gamma_2 - \gamma_1)\ g}{3\ f_1(z)} \cdot \frac{(V_{H-}^2 - V_{H+}^2)}{V_{dc} \cdot V_{HS}^2} \tag{4.20}$$

where

$$f_1(z) = \frac{E(z)}{V_{dc}} = \frac{2}{h\,(1 - \underline{z}^2)\,\ln\,[(1 + \underline{z}_{min}) / (1 - \underline{z}_{min})]} \tag{4.21}$$

is the position function according to Eq.(4.4). Thus the surface charge density ρ_s is

$$\rho_s = \frac{\pi R\,(\gamma_2 - \gamma_1)\,g}{6\,f_1(z)} \cdot \frac{(V_{H-}^2 - V_{H+}^2)}{V_{dc} \cdot V_{HS}^2} \tag{4.22}$$

4.3 Cell Levitation System

A sectional view of the experimental levitation chamber and the block diagram of the whole system are shown in Figure 4.4. The cone-plate electrode assembly (with z_{min} = 600 μm and θ = 60° as defined in Figure 4.2) is housed in a Plexiglas chamber fitted with cover glass windows to aid the optical monitoring of the chamber contents. One of the optical windows is removable to facilitate the cleaning of the chamber and introduction of fresh dilute cell suspension each time a new experiment is to be conducted. The window is secured in place and sealed with vacuum grease to eliminate evaporation and the influence of air currents. The assembled chamber is mounted and held in place with spring-loaded clips on a vertical microscope stage with the electrode connected to the wide band summing amplifier. This amplifier was built with a wide band, high slew rate, and high output current operational amplifier (*HA-2542*, Harris).

A conventional light source fitted with an infrared filter is used to illuminate the chamber and the cell image is focused into a MOS Solid State video camera (model

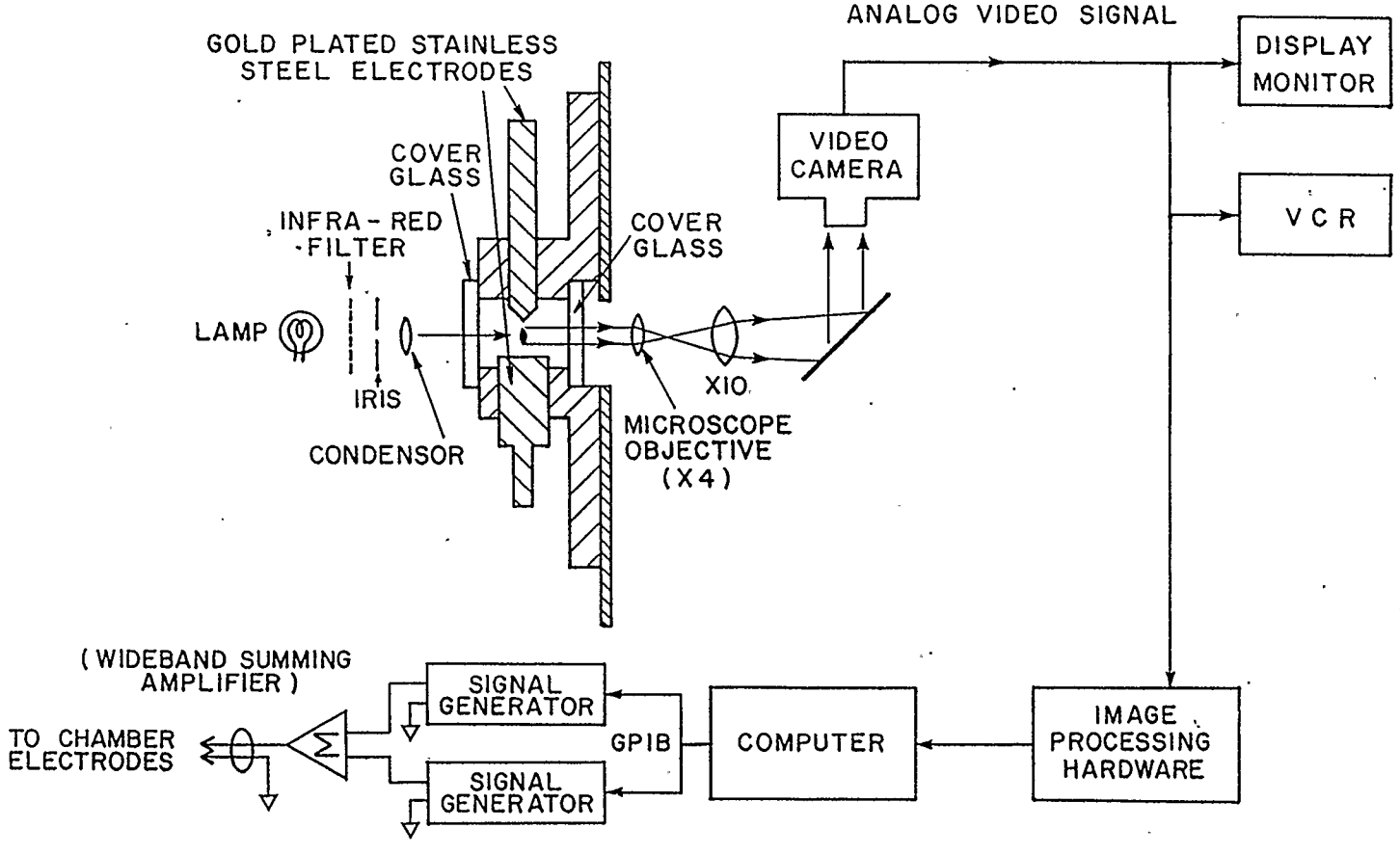

Figure 4.4. Sectional view of the levitation chamber together with the block diagram of the whole system

JE2362A, JAVELIN Electronics Co., Japan) and displayed on a video monitor. The video signal from the camera is also interfaced to a real-time image acquisition PC board (model MVP-AT, Matrox Electronic Systems Ltd., Dorval, Quebec) which is plugged into a 286-based IBM-AT computer. The computer is interfaced to the two signal generators (model 178 Wavetek, San Diego, CA and model 3325A Hewlett Packard, Loveland, Colorado) via the GPIB-488 bus to facilitate the controls of both the amplitudes and frequencies of the voltages applied to the chamber electrodes (via the wide-band summing amplifier).

Three levitation modes have been integrated in the levitation software: Capture mode, Regulate mode, and Automatic Measuring mode. When the levitation program is activated it enters the capture mode first. In this mode, manual adjustment of the applied voltage can be carried out to select and capture a suitable cell. Once the cell has been selected in the above manner and appropriately positioned between the chamber electrodes, the operator can switch the process to the regulate mode by striking a single key. In this mode, the feedback control loop is activated so that automated levitation (adjustment of applied voltage) can be performed. With the cell stably levitated along the axis, the process can be switched to either automatic EP measuring mode or DEP measuring mode. In the automatic DEP measuring mode, the software is designed such that once the cell is stably levitated at a fixed location for a prescribed time period (typically from 10 to 20 sec), the values of the applied voltage over this time period are averaged and saved with other data (such as frequencies, cell size, etc.) in a file, and the frequency of the applied voltage is automatically changed to a new preprogrammed value.

These preprogrammed frequency values are chosen so that when plotted on a logarithmic scale, the data points are evenly spaced.

4.4 Algorithms for Cell Position Detection and Cell Size Measurement

Since the field gradient is position dependent, hence Re[$\underline{K}_e$] obtained with our DEP levitation method is also position dependent, which has been shown in Eqs.(4.6) and (4.7). Therefore, detection and measurement of cell position are crucial for the accurate measurement of the DEP spectrum.

4.4.1 A Simple Approach Based on the Optical Intensity Profiles

Initially, a simple thresholding scheme was employed to locate the cell position. At the beginning of each levitation measurement, the selected cell is always properly positioned (in Capture mode) within a rectangular processing window before the process is switched to the feedback levitation mode. The cell image normally appears as a dark spot on a light background or as a dark ring. The optical intensity profiles of both x and y image planes of the processing window are calculated and then compared with a threshold value to detect the cell edges (see Figure 4.5). It was found that such a simple approach was unsatisfactory, particularly when the cell is moving rapidly or when another piece of material floats by the processing window or when the background intensity is non-uniform. Furthermore, background noises due to the illumination system and image acquisition board also gave rise to false detections of the cell position (this was confirmed by the observed fluctuations of the detected position of a fixed object in a static image). The above non-idealities were further compounded by the uneven density of the cell image, or cell reorientation induced at certain frequencies, giving rise to erroneous

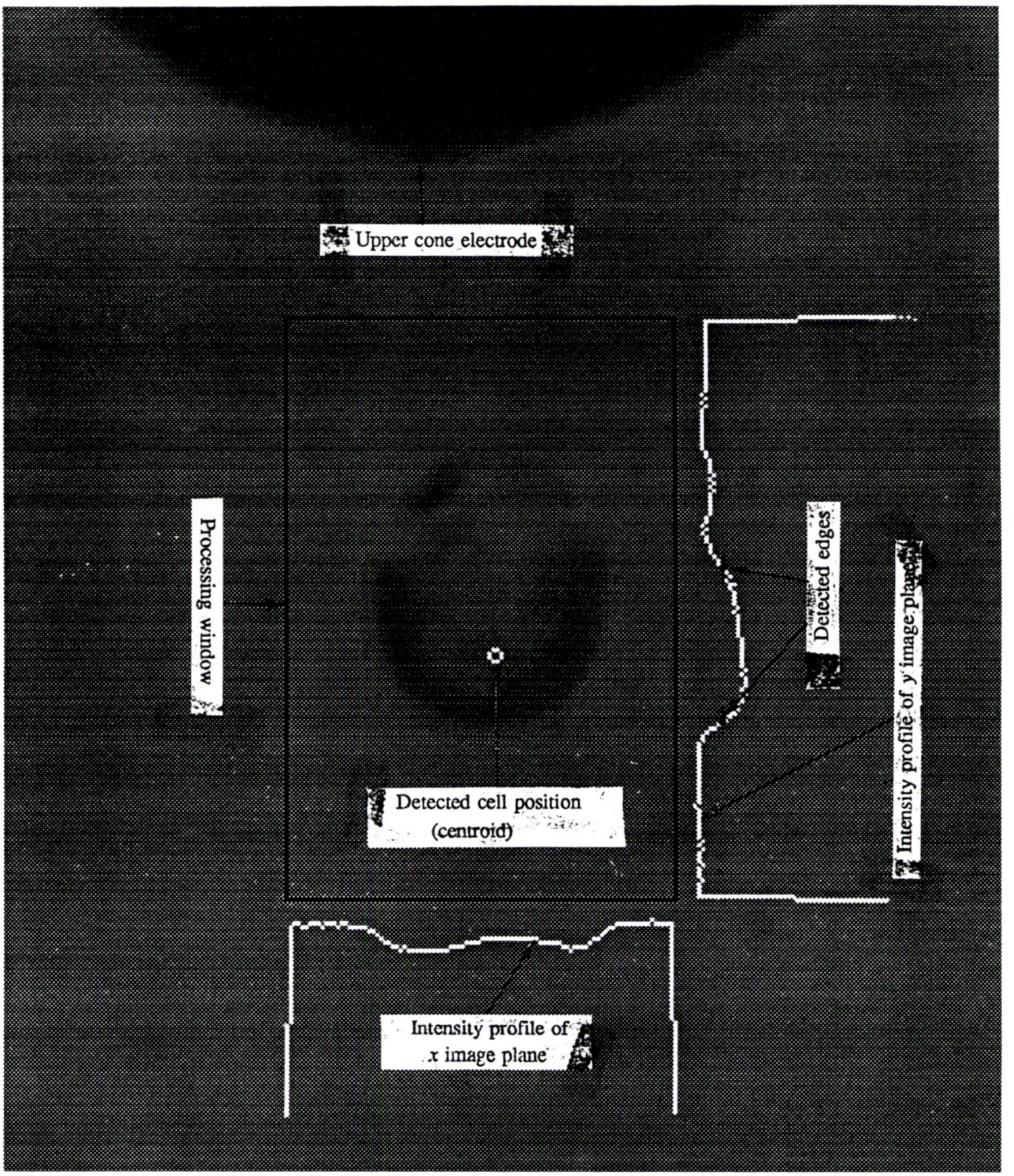

Figure 4.5. The actual cell image displayed during levitation experiment.

detections of the cell position (see Figure 4.5). Therefore, more reliable cell-position detection algorithms were considered.

An attempt has been made to develop an algorithm which can not only determine the position of the cell (i.e. the coordinates of centroid of the ellipse-like cell) but also the cell size and its orientation as well as shape information, all of which are crucial for investigations of the instantaneous mechanical responses of cell or cell chains due to the DEP effect. The following section describes the research work on the cell image processing and analysis for achieving the above goals.

4.4.2 Shape Analysis and Measurement of Cell Image Using Elliptic Fourier Fitting

In cell DEP levitation and electrorotation measurements, and cell fusion, the shape information are of great interest since the mechanical responses of cell (e.g. changes in position, shape, and orientation) under various electric field conditions are important to the understanding of its various polarization response mechanisms.

For the shape analysis of an image, there are usually several procedures involved: thresholding and segmentation, contour tracking and feature extraction.

Thresholding, Segmentation and Edge Detection

A correct edge extraction or segmentation of a cell image is the first step for the accurate shape measurements and analysis. During the past decades considerable effort has been put into the research towards the automatic segmentation of various kinds of cells[43-46]. Most of them, however, are concerned with the cell images that are either in smear or slice forms, both of which have been more or less preprocessed chemically or physically, not in a live and intact suspended state. The most widely used technique

dealing with the segmentation problem is the classical one, proposed by Prewitt and Mendelsohn[44]. This technique is based on the histogram of the digitized cell image. Ideally the histogram will have three peaks, corresponding to nucleus, cytoplasm and background, respectively. The minima between these three peaks represent optical density values with low frequency of occurrence and should correspond to the boundaries between different parts of the image. For our cases, only the whole cell image (i.e. nucleus plus cytoplasm) needs to be segmented from the background. Therefore the problem falls into finding an appropriate valley between the rightward peaks, if any. Fortunately, for most of the cells under study, the histograms of the cell (plant protoplast) images do present a valley, although often not so distinct, between the high peak (which represents the fairly uniform bright background) and one or some fairly low peaks which represent mainly the grey levels of the pixel within the cell, which makes it possible for us to develop an automatic thresholding algorithm. Based on this property of the cell image an automatic threshold-searching algorithm has been developed. It first smoothly filters the histogram, then starts searching from the right side of the histogram (i.e. from the high optical intensity values). After passing the first high peak, it chooses the first valley as the threshold value. Figure 4.6 shows an example of the segmented cell image and its original image.

In some cases, when there is no distinct valley in the histogram, the threshold determined with this algorithm could easily affect the size of the segmented cell image. Therefore another supplementary approach has also been studied.

Minimum error thresholding seems to be a theoretically attractive idea[45]. The grey

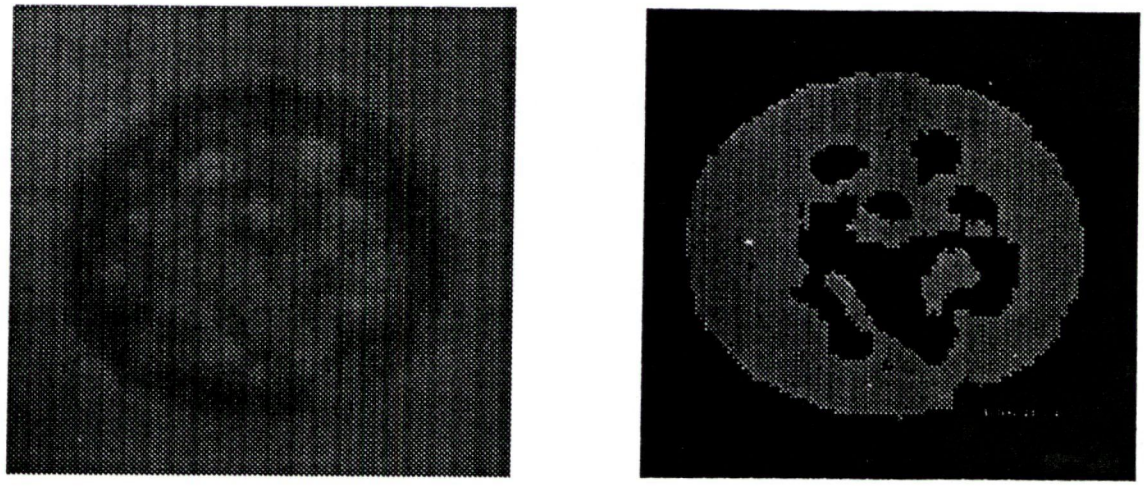

(*a*) (*b*)

Figure 4.6. Original (*a*) and segmented (*b*) cell image

level histogram is regarded as a mixture of a limited number of densities originating from some density function, e.g., normal function. In practice, however, this approach suffers from the same problem as the classical "dip-find" algorithm: one must know in advance how many peaks there are. In addition, finding the optimal threshold by decomposing a mixture of densities is a very time-consuming task. Other investigators[46,47] have also used some complicated and time-consuming approaches such as edge detection based on entropy of the image, and object oriented segmentation.

After investigating the effects of some gradient operators[43] (such as Sobel and Kircsh) on our cell images, it is found that the resultant images yield a fairly good extracted boundary. Therefore for those cell images which have no distinct valley in their histograms, we first applied a gradient operation (such as Sobel or Kircsh operators)

to highlight the cell boundary before using a similar thresholding-search algorithm. The algorithm was slightly modified to achieve a closed boundary segmentation regardless of the thickness of the boundary. By using a thinning operation[48,49], we can always obtain the skeletal boundary which represents the real boundary of the imaged cell. Figure 4.7 shows the segmented boundary image (after having being processed with a gradient operator) and the resulting skeletal boundary, after a thinning operation. Figure 4.8 shows the resulting images with their highlighted boundaries for the above two different method.

Contour Tracking

For the analysis of the shape of the segmented cell object, a closed outer boundary has to be extracted for this purpose. For the image segmented directly from its original one (such as the one shown in Figure 4.6), before contour tracking, a preprocessing operation

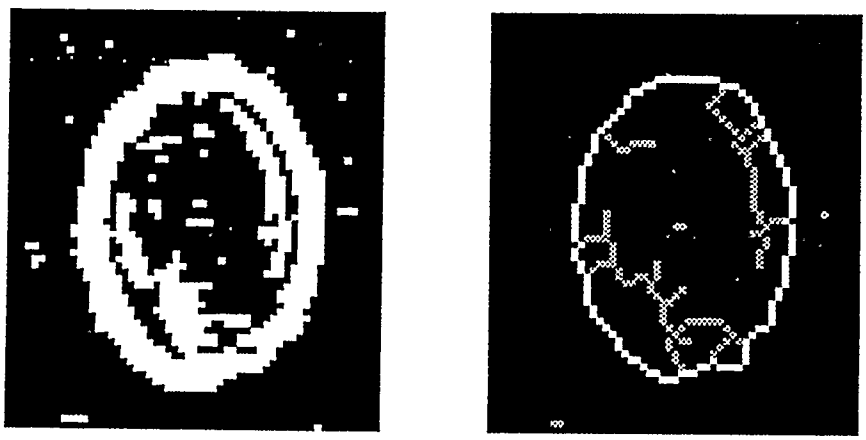

(*a*) (*b*)

Figure 4.7. Segmented boundary image (*a*) and further thinned boundary image (*b*).

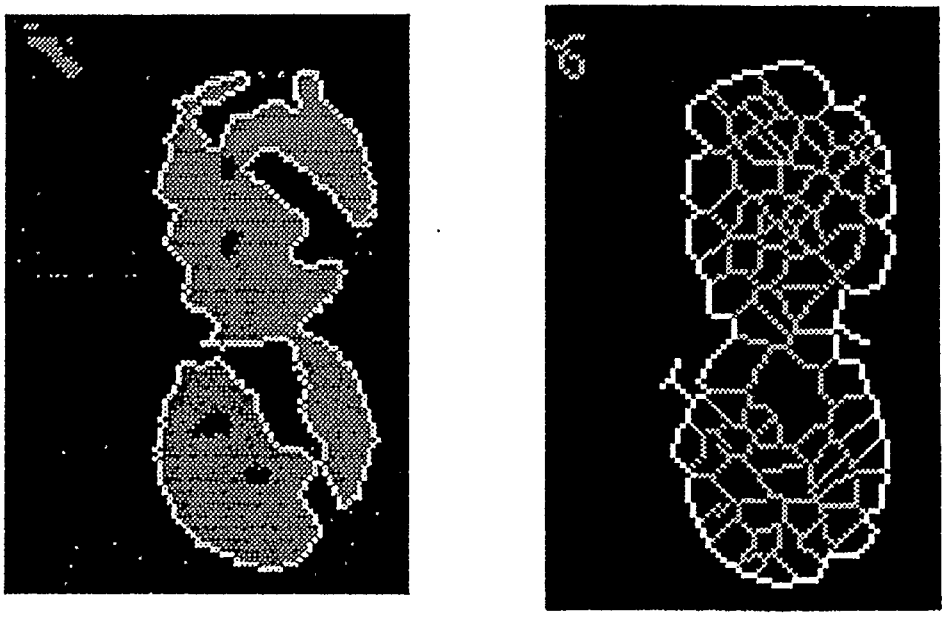

(*a*) (*b*)

Figure 4.8. The resulting image obtained with direct thresholding method (*a*) and the one obtained with gradient operation-plus-segmentation-plus-thinning method (*b*).

is applied to the segmented binary cell image to eliminate some local convexities and concavities which do not represent the fine shape of the cell but some local artifacts introduced by the segmentation. The preprocessing involves two repeated steps:

-First, an expanding which assigns a background point to be an object point when there are at least 3 object points within its 4-neighbourhood;

-Second, a shrinking which assigns an object point to be a background point when there are at least 3 background points within its 4-neighbourhood. This operation will also be illustrated to be useful for minimizing errors of some feature-descriptor data which are sensitive to fine concavities and convexities.

A contour tracking algorithm has been developed to identify the outer boundary of a biological cell. From the definition of the boundary of a plane set we know that the

"contour" of a connected set of pixel R is the set of all pixel in R which have at least one d-neighbour not in R. The algorithm can be described in terms of an observer who walks along pixel belonging to the set and selects the rightmost pixel available. The initial pixel is found by searching (top-to-bottom, left-to-right scan) the first pixel whose 4-neighbour is not in set R (i.e. has zero value). Sometimes there may exist some cell fragments (i.e., floating pieces) left to and above the object (cell) image. In such cases, the tracking would occur around the first top-left fragment. To prevent this erroneous detection of cell fragment, the tracking program checks the length of the tracked contour. If it is short, which means that a far smaller object than cells has been traced, the program sets another starting point which is lower than the previous one and repeats the tracking procedure. During the boundary tracking process, the chain codes representing the cell contour are also generated for later calculation of perimeter.

Fourier Featuring of the Cell Contour

Fourier descriptors have been successfully used by some investigators[50-52] for the characterization of closed contours. In our project, the ultimate goals are to determine the position, orientation, area and perimeter of the ellipse-like cells as well as some shape information, especially the variations of the shape and orientation of the cell under various electrical fields. The Fourier transform of the boundary data of a cell image seems to be the best way to provide elliptic fitting and shape features of the cell image.

Fourier Transform of a Closed Contour

For a given region, once its boundary points have been determined, we can extract some information directly from the boundary points. This is very useful for the

discrimination of shapes of different regions. For a fixed point b_0 on a closed contour, the variations of coordinates of a moving point b along the contour is a periodic function, therefore it can be represented by a Fourier series. The coefficients of each harmonic are related directly to the shape of the boundary. When the number of the harmonics is sufficiently large, the shape information can be extracted almost completely and also the shape can be reconstructed by these limited harmonics.

Let C represent the boundary of a region R, as shown in Figure 4.9. A moving point b moves counterclockwise along C from the starting point b_0. The coordinates of the moving point b can be described using a phasor in the complex plane. i.e.

$$U(t) = x(t) + j\, y(t) , \qquad 0 \le t < T \tag{4.23}$$

After a period T, point b returns to the starting point b_0. Therefore $U(t)$ is a periodic

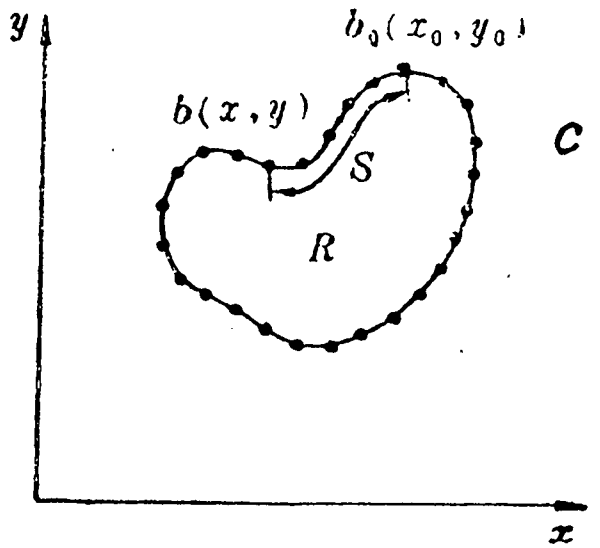

Figure 4.9. Illustration of a closed contour C

function of t with period of T, and can be represented by

$$U(t) = \sum_{n=-\infty}^{+\infty} p_n \, e^{j2\pi n \frac{t}{T}}$$
$$= p_0 + \sum_{n=1}^{\infty} \left(p_n \, e^{j2\pi n \frac{t}{T}} + p_{-n} \, e^{-j2\pi n \frac{t}{T}} \right) \qquad 0 \le t < T \tag{4.24}$$

where

$$p_n = \frac{1}{T} \int_0^T U(t) \, e^{-j2\pi n \frac{t}{T}} \, dt \, , \qquad n = 0, \pm 1, \pm 2, \ldots . \tag{4.25}$$

It can be shown that the points $(x_n(t), y_n(t))$, represented by the vectors

$$U_n(t) = p_n \, e^{j2\pi n \frac{t}{T}} + p_{-n} \, e^{-j2\pi n \frac{t}{T}} \tag{4.26}$$

all have elliptic loci, and that the Fourier approximation to the original contour can be viewed as the addition in proper phase relationship of the rotation phasors which are defined by $x_n(t) + j\, y_n(t)$. Each rotation phasor has an elliptic locus and rotates faster than the first harmonic by its harmonic number n.

The Fourier coefficients can also be derived solely from boundary chain code [51] which is a little more complicated than using the existing boundary coordinate data array. In practice, the available boundary data is in discrete form, therefore FFT algorithm can be used to calculate the Fourier coefficients.

In the course of the contour tracking, the boundary has been stored as a complex sequence: $z_0, z_1, z_2, \ldots, z_{N-1}$ where z_0 contain the coordinates of the staring points and z_i contains these of the ith point of the boundary. Using Discrete Fourier Transform, the

Fourier coefficient sequence is computed as:

$$p_n = \sum_{k=0}^{N-1} z_k \, e^{-j\frac{2\pi kn}{N}}, \qquad n = 0, 1, 2, ..., N-1 \tag{4.27}$$

In order to use the FFT algorithm, an interpolated boundary of $M = 2^r$ points with $2^{r-1} \leq N < 2^r$ is generated from the original boundary.

Due to the periodicity property of sequence p_n , this sequence can be represented by:

$$p_{-\frac{N}{2}+1}, p_{-\frac{N}{2}+2}, ..., p_{-1}, p_0, p_1, ..., p_{\frac{N}{2}} \tag{4.28}$$

In order to construct the approximated elliptic contour, simply comput the inverse FFT of the above Fourier sequence with harmonic components of greater than 1 being assigned a zero value. The resulting data sequence will represent the coordinates of the elliptic contour. By including a number of higher order Fourier coefficients in the inverse FFT computation, a well reconstructed original boundary can be obtained.

From the above discussion we know that for most cells in suspension (which are usually elliptic), the approximation of the contour by using the base harmonic of its Fourier representation, which yield an elliptic contour, will give us many shape information in combination with some other descriptor coefficients.

Feature Extraction from Fourier Coefficients

From the Fourier coefficients we can get the following shape features

1. Circularity

$$F_1 = \frac{|p_1|}{\sum_{n=1}^{+\infty} (|p_n| + |p_{-n}|)} \tag{4.29}$$

Where $F_1 = 1$ corresponding to a circle, otherwise $0 < F_1 < 1$

2. Ellipticity

$$F_2 = 1 - \frac{|p_1| - |p_{-1}|}{|p_1| + |P_{-1}|} \tag{4.30}$$

When the contour C approaches a circle, F_2 approaches zero.

If we neglect all harmonic components except the base, then

$$U(t) = p_1 e^{j2\pi \frac{t}{T}} + p_{-1} e^{-j2\pi \frac{t}{T}} \tag{4.31}$$

will represent the approximated ellipse of contour C. It can be shown that $|p_1| + |p_{-1}|$ and $|p_1| - |p_{-1}|$ are the magnitudes of semi-major and semi-minor axes of the ellipse, respectively.

3. Density

The density here is defined as

$$F_3 = \frac{S^2}{4\pi A} = \frac{S^2}{4\pi^2 [\sum_{n=1}^{\infty} n (|p_n|^2 - |p_{-n}|^2)]} \tag{4.32}$$

where S is the perimeter of the contour C and A is the area of the enclosed region. For the same area, circular contour has the minimum value of $F_3 = 1$.

4. Concavation

$$F_4 = \frac{\sum_{n=1}^{\infty} n^3 (|p_n|^2 - |p_{-n}|^2)}{(|p_1|^2 - |p_{-1}|^2)} \tag{4.33}$$

If there are no concavities and convexities, F_4 will be 1.

It can be shown that all the descriptors described above are independent of position, size, orientation, rotation and translation of the contour. By using these descriptors, we can obtain most of the information we want. The zero harmonic p_0 can give us the coordinates of the centroid of the approximated ellipse, based on which the position of the levitated cell can be determined. From the base harmonic coefficient we can derive the magnitudes of semi-major and semi-minor axes of the approximated ellipse which can represent the ellipse-like cell in our case. By searching the point on the approximated elliptic boundary which has the maximum distance to the centroid, the orientation of the cell can be determined.

In addition to the above measurements, with the above defined Fourier descriptors, we can also obtain some cell shape information. For the coefficient F_4, the original definition seems to be not quite appropriate for our situation because F_4 takes into account every harmonic components with increasing weight of n^3. Therefore some fine concavities and convexities, which might be caused by low spatial resolution and/or segmentation and correspond to the high harmonic components of the Fourier series, will contribute to F_4. In our situation, we are only interested in relatively larger concavities and convexities, which correspond to the lower harmonic coefficients. After some testing a modification has been made in the numerator of the original F_4, as shown below:

$$F_4 = \frac{\sum_{n=1}^{3} n^3 \left(|p_n|^2 - |p_{-n}|^2 \right)}{\left(|p_1|^2 - |p_{-1}|^2 \right)} \tag{4.34}$$

where only 1st, 2nd, and 3rd-harmonic coefficients have been considered. Figure 4.10 shows the different cell shapes and their corresponding descriptor values.

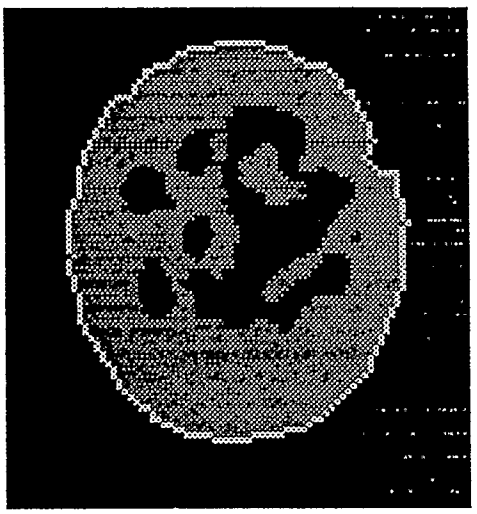

(*a*) F_1=0.77, F_2=0.13, F_4=1.04

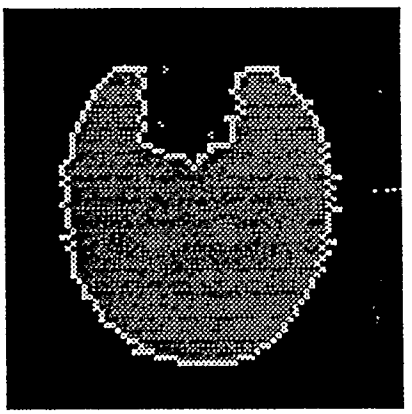

(*b*) F_1=0.48, F_2=0.01, F_4=1.46

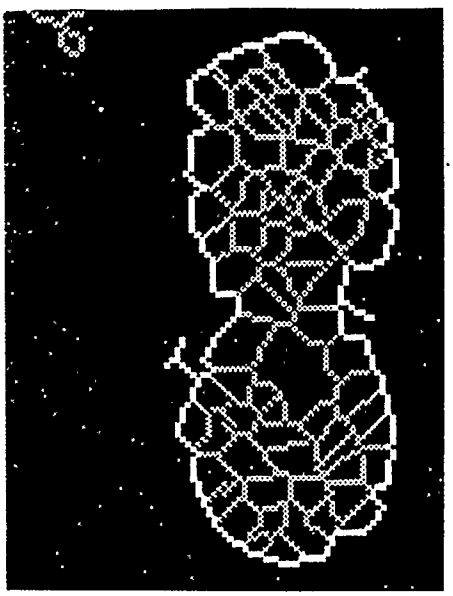

(*c*) F_1=0.52, F_2=0.66, F_4=2.70

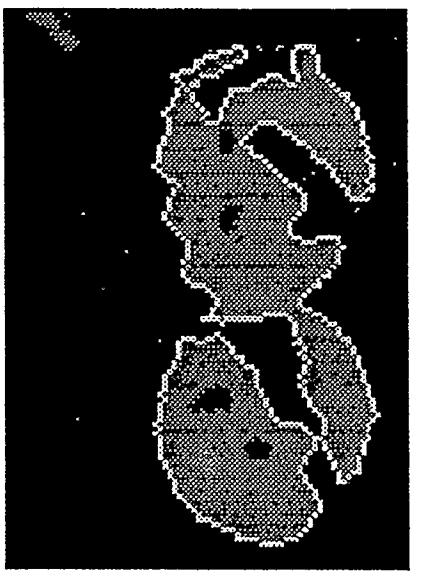

(*d*) F_1=0.40, F_2=0.71, F_4=5.15

Figure 4.10. Different cell shapes and their corresponding descriptor values

Elliptic Fitting of Cell Contour

In addition to feature extraction, Fourier transform of contour has also been used here for elliptic fitting. In some situation we know that the actual shape of the *Canola* protoplast is elliptic, but the digitized image shows very poor contrast in part of the cell boundary. This is partially due to the poor performance of imaging system and partially due to the presence of the chloroplasts inside the cell which represent the dark area and cause greater grey-level changes inside the cell than the actual edge between the cell membranae and the medium. In such cases, when performing the segmentation, the resulting image will show some concavities in the boundary of segmented object (see Figure 4.10*b,d*). This situation can not be circumvented even using more complicated edge detection or thresholding techniques simply because there are almost no grey-level changes in some part of the real boundary. For the above reason, the elliptic fitting of the cell contour is introduced to obtain a more accurate shape determination. In such cases, the fitting procedure is described as follows:

After performing all the processing described above, the Fourier descriptors are obtained. If F_4, which reflect the relatively larger concavities, has a value greater than a preset value, say 1.2 as we found in practice, and the F_2 is less than a preset value, say 0.3, which means that there could not be two cells, then the same value as the segmented pixel will be assigned to the approximated ellipse contour pixel which will fill some part of concavities. After performing the tracking process and Fourier transform again, another ellipse will be obtained which will fit better the actual ellipse-like contour. Therefore more accurate measurements can be obtained, as shown in Figure 4.11.

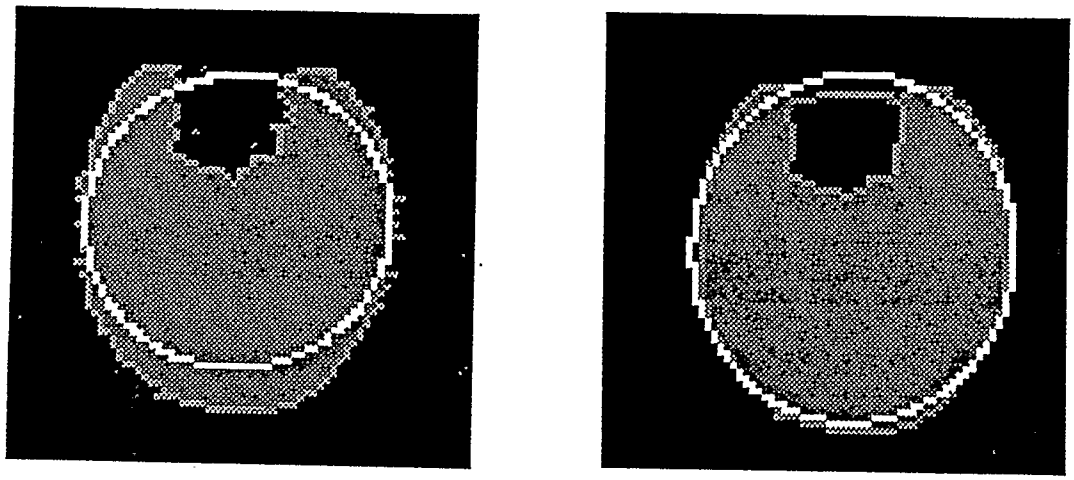

(a) Result of elliptic fitting once (b) Result of elliptic fitting twice

Figure 4.11. Results of elliptic fitting

In addition to the elliptic fitting of a cell boundary image using the base harmonic of its Fourier coefficients, the limited number of these Fourier coefficients can be used to reconstruct the original boundary. Figure 4.12 shows the reconstructed boundaries using one harmonic and two harmonics.

From the above analysis and results, we conclude that the elliptic approximation of the cell image by using Fourier Descriptor of cell boundary can give a fairly accurate measurement of the cell shape for most situations. The elliptic approximation of the cell is considered the optimal and easiest way to obtain the cell shape information, e.g. area, perimeter, position, ellipticity and orientation.

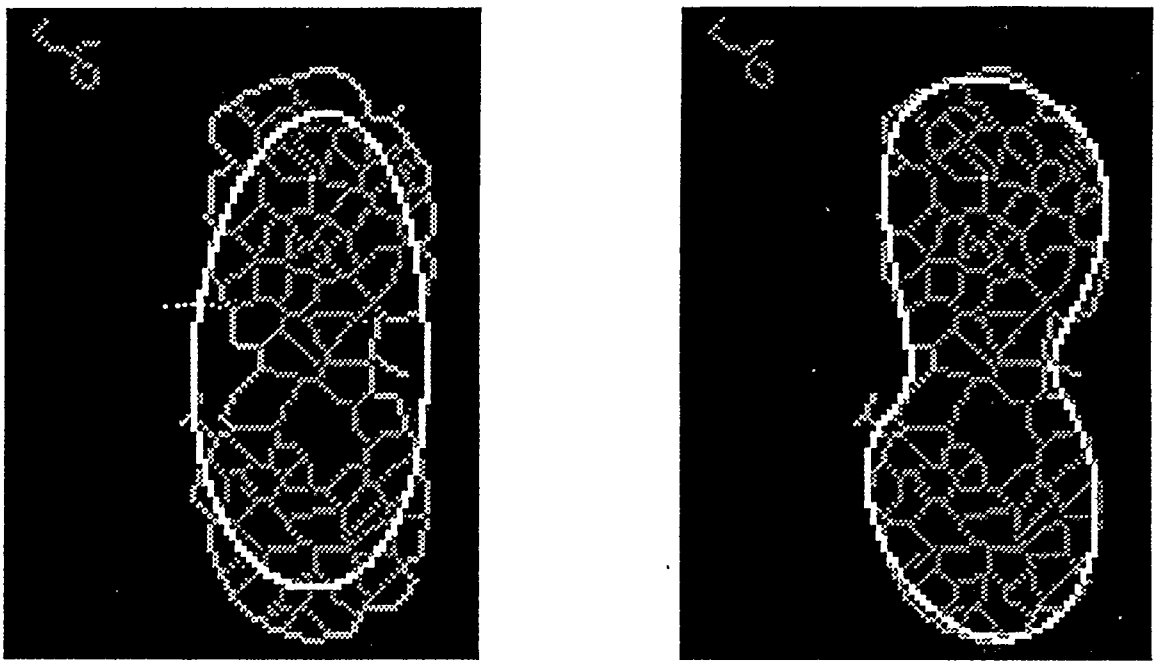

(*a*) (*b*)

Figure 4.12. Boundary reconstruction using one harmonic (*a*) and two harmonic (*b*)

4.4.3 An Adaptive Approach for Cell Position Detection and Size Measurement

Although the above method has been proved to be effective for the automatic measurements of the cell position, cell size, and other shape information, the principle shortcoming of this method is the heavy computational burden, which hence slows down the whole feedback control process. This situation can be alleviated by resorting to either a more efficient coding (e.g. using assembly language) or incorporating fast DSP processor and/or parallel processing architecture, though the actual implementation task may not be straightforward in practice.

In order to achieve reliable and accurate detection of the cell position in our present system without resorting to the complicated approaches suggested above, a simple

adaptive cell position detection method has been developed based on the optical intensity profiles of the processed cell image. For each image frame, the optical intensity profiles of both x and y image planes within the processing window are calculated and three position values are detected for each image plane: two edge position values (coordinates) and one peak position value(see Figure 4.13). Here y_1 and y_2 are the coordinates of the two detected edges and y_p is the coordinate of the peak of the optical profile (see Figure 4.13). $L = y_2 - y_1$ is considered to be the cell length in that projected plane (here only y image plane is taken as an example). L_a is the average of previous four L values. The detected centroid is determined by these values according to the following criterion:

If the present L is approximately the same as L_a, then y_2 and y_1 are considered to be the true edges and the centroid coordinate is calculated as $y_1 + L/2$; If L is sufficiently different from L_a, (e.g. $|L - L_a| > L_a/4$), then chose the edge point, which has less change in distance from y_p compared with that of previous frame, as the true edge point and calculate the centroid coordinate from this point and L_a (i.e. If y_2 is the true edge point, then the centroid coordinate is $y_2 - L_a/2$; If y_1 is the true edge point, then the centroid coordinate is $y_1 + L_a/2$).

Such a screening process has proved to be very effective in preventing most false-edge detections and gives reliable tracking of the cell. In most cases, however, there is still a constant deviation between the detected and the real centroids due to the uneven optical density of the cell (see Figure 4.5) and this deviation may change when the cell undergoes reorientation. This deviation can be eliminated manually in the following way: Each time the detected coordinates of centroid are obtained, a bright ellipse, the centroid of

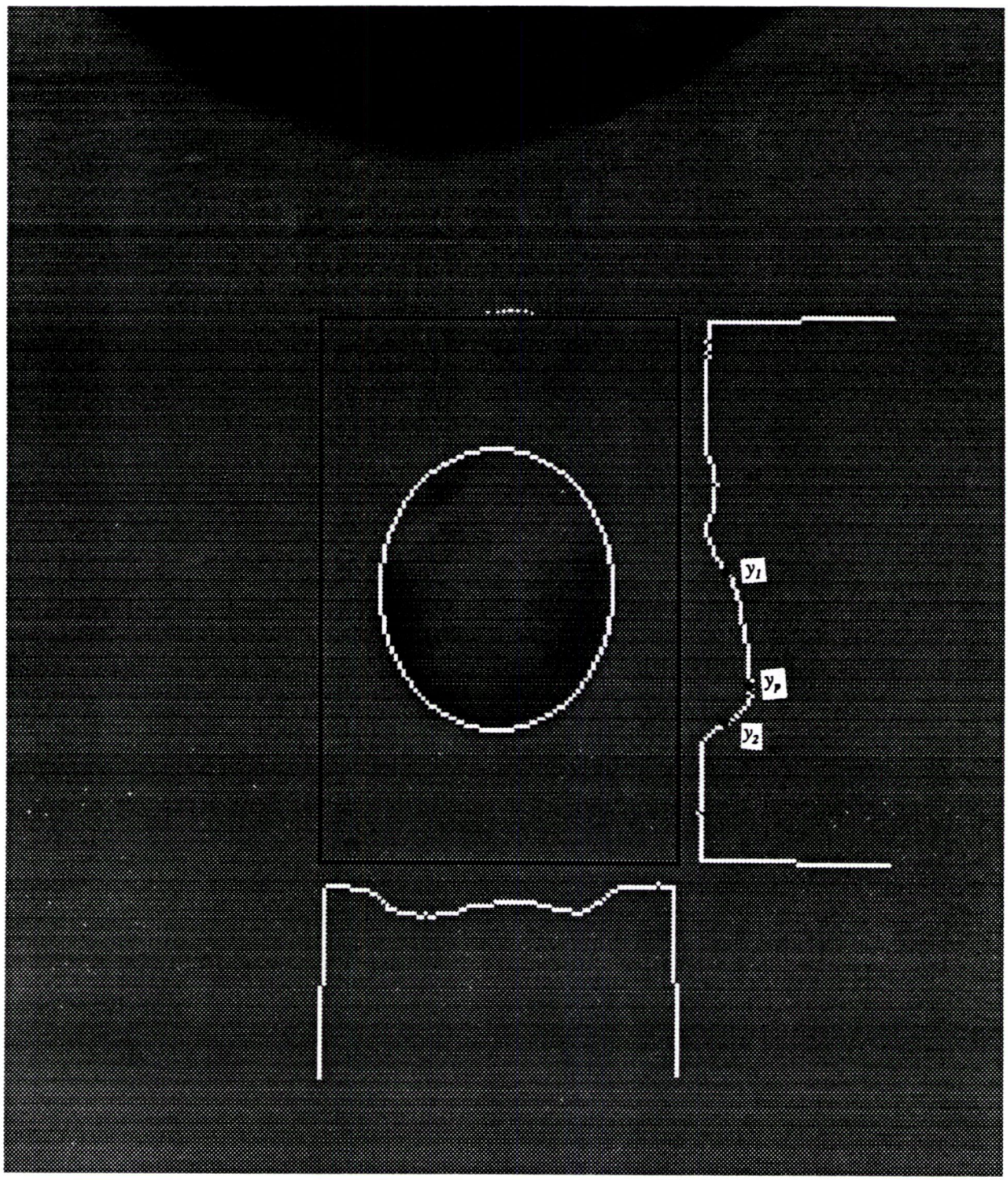

Fig. 4.13. Schematic illustration of the cell detection method

which is the detected centroid, is superimposed upon the original cell image and displayed dynamically. If the centroid of the ellipse does not coincide with that of the cell, the operator can move the ellipse via the keyboard until it coincides with the real cell location. The algorithm was designed such that the centroid of the ellipse is always considered as the finally coded cell position which serves as the input to the feedback controller. Furthermore, the size of the ellipse may be adjusted manually to match the size of the real cell so that the cell size can be easily monitored in this manner.

4.5 Algorithm for Feedback Control of Cell Position

In order to keep the particle levitated stably at a fixed position, a proportional-plus-integral-plus-derivative (PID) controller was incorporated in the closed-loop feedback system, as shown in Figure 4.14. The *plant* of a control system is referred to as that part

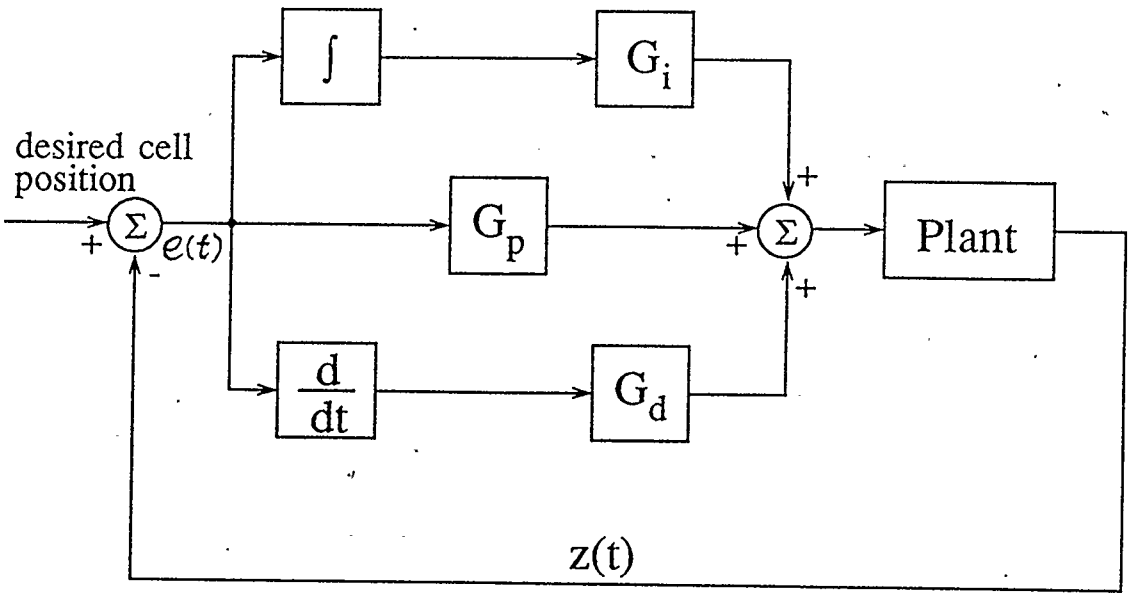

Figure 4.14. The block diagram of the feedback control system

of the system to be controlled, $z(t)$ is the detected cell position signal (see Figure 4.2). The PID position control algorithm is based on the following equation[53]:

$$V(t) = G_p e(t) + G_i \int e(t)\, dt + G_d \frac{de(t)}{dt} \tag{4.35}$$

where $e(t)$ is the position error and G_p, G_i, and G_d are the gain terms for the proportional, integral, and derivative elements of the equation, respectively. In our actual implementation, instead of the standard PID configuration, a modified PID configuration has been used, as shown in Figure 4.15. The input to the differentiator in such a configuration is the cell position $z(t)$ rather than the position error $e(t)$. The effect, however, remains the same. The simple Euler method (or the rectangular rule) was used

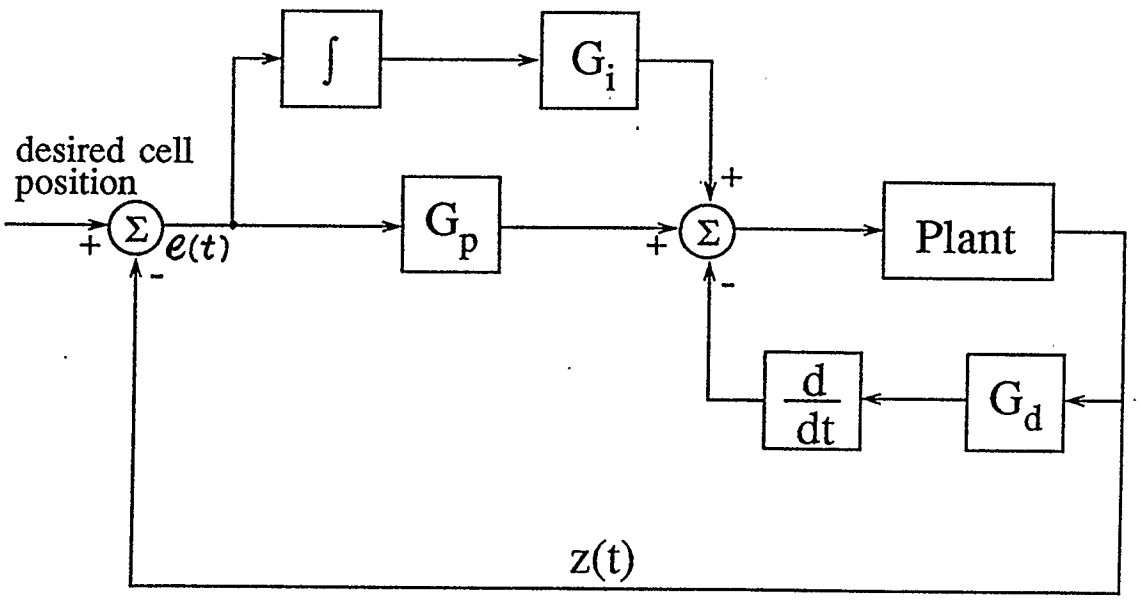

Figure 4.15. The block diagram of the modified PID controller

to perform the numerical integration, i.e.:

$$V_i(nT) = G_i \sum_{k=1}^{k=n-1} e(kT) \tag{4.36}$$

Where n and k are the time indices, T is the sampling interval. For the numerical differentiation, although the slope of the straight line that connects two adjacent data points can be chosen as the discrete derivative, it is easily understood that this simple method results in high gains for high frequency elements, which would reduce the stability of the system. Instead, a five-point smooth numerical differentiator has been implemented in our system. The difference equation describing the above scheme is given as follows (for simplicity, T has been omitted):

$$D(n) = 101z(n) - 144z(n-1) + 36z(n-2) + 16z(n-3) - 9z(n-4) \tag{4.37}$$

Where $z(n)$ is the cell position data. The effect of this differentiator is that it limits the high frequency gain to certain value instead of letting it increase infinitely (as frequency increases infinitely). This effect is clearly shown in its frequency response plot in Figure 4.16. Therefore, the actual controller is implemented as follows:

$$V(nT) = G_p e(nT) + G_i \sum_{k=1}^{k=n-1} e(nT) + G_d D(nT) \tag{4.38}$$

Although the PID controller is relatively robust for most feedback systems, it is however unable to accommodate large variations in the system-parameters of the controlled plant. From the earlier experiments, we found that the PID controller could not be effective over the entire applied frequency range. This is obviously due to the fact that the Re[$\underline{K}_c$] has different values in different frequency regions, which results in the

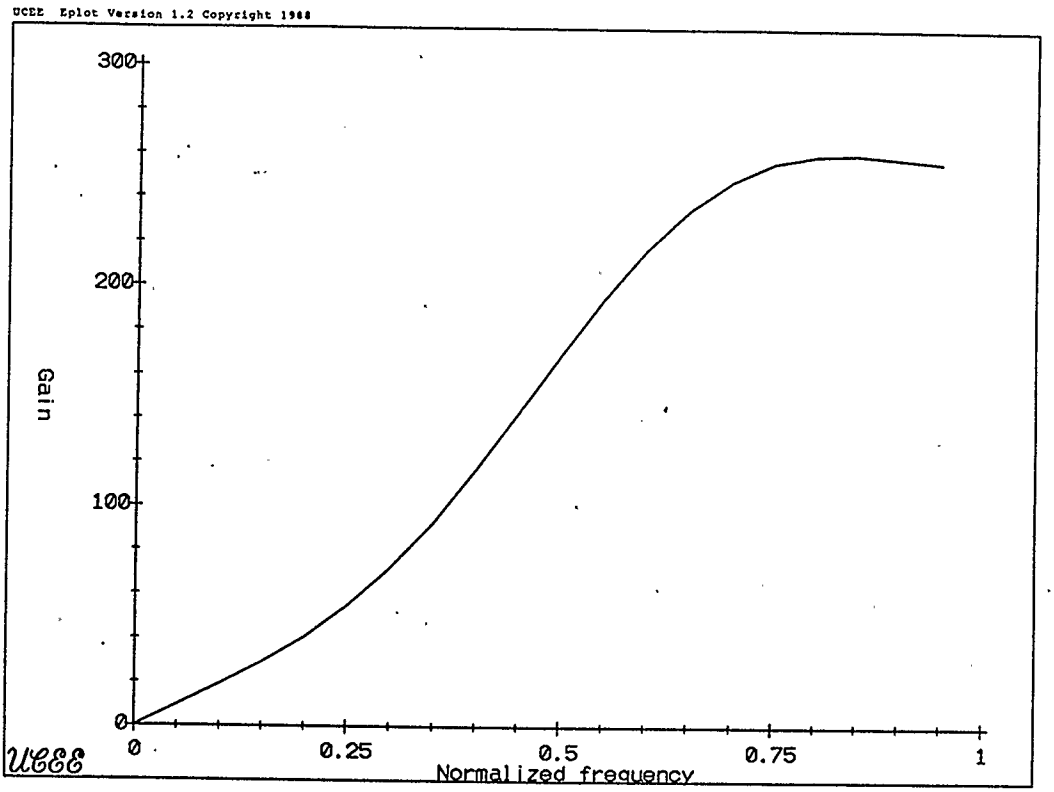

Figure 4.16. Frequency response of the five-point smooth differentiator.

variations in system-parameters of the plant. Although some form of adaptive control can be employed, they usually involve heavy computations (matrix multiplication), which increases the controller time constant and ultimately risks the stability. Instead, we modified the controller expressed in Eq.(4.38) by introducing a variable weighting factor which is related to Re[$\underline{K}_c$] through the averaged levitation voltage, i.e.:

$$V(nT) = C \cdot V_{LEV} \left[G_p e(nT) + G_i \sum_{k=1}^{k=n-1} e(nT) + G_d D(nT) \right] \qquad (4.39)$$

where V_{LEV} can be chosen as the levitation voltage at the previous adjacent frequency. C is an adjusting coefficient determined experimentally. This simple method has been proved to be effective over a wide frequency range.

CHAPTER 5

EXPERIMENTAL PROCEDURE AND DATA CORRECTION

5.1 Sample Preparation and Operation Procedure

Because of their availability and relatively easy acquisition, all the experiments reported here were conducted on *Canola* plant protoplasts.

The plant protoplasts used in this investigation were extracted from *Canola* leaves using an enzymatic digestion procedure to cleave the glycan and pectin linkages in the cell wall. To minimize starch content in the leaves, three-week-old *Canola* plants were obtained and kept in the dark for approximately 12 hours before harvesting. The leaves were sterilized using a 20% bleach solution plus two drops of wetting agent (TWEEN 20) before dissection. The dissected leaves were immersed in a digestion mixture consisting of 0.4% cellulase Onozuka RS, 0.025% Pectolyase Y23 (supplied by Kanematus-Gosho, Tokyo, Japan), 8% sorbitol, and 100 mg/ml $CaCl_2$. The *pH* of the digestion mixture was adjusted to 5.8. The *Canola* leaves immersed in the digestion mixture were incubated in a dish for about 12 hours at room temperature, or until sufficient protoplast density was attained. The contents of the dish were then gently agitated so that more protoplasts were freed. The protoplasts were then separated from the protoplasting solution by centrifuging the mixture for 4 min at 40 *g*. The supernatant was discarded and the protoplast pellet resuspended in 8% sorbitol. This procedure was repeated three more times before the cells were finally diluted, ready for the levitation experiments.

The dilute protoplast cell suspension was loaded into the levitation chamber and secured on the microscope stage. The levitation program was activated and the capture mode invoked. A suitable cell is selected by adjusting the applied voltage. Once the cell is at a proper position in the processing window without other cells inside and the bright ellipse constantly tracks the cell movement, the process is switched to the Regulate mode. In this mode the excursion between the ellipse and the real cell is eliminated by shifting the bright ellipse via the keyboard and the size of the ellipse is adjusted to match the cell in order to obtain the cell size. The process is retained in this mode until the suspension in the chamber becomes stable and the cell is on the vertical axis, then it is switched to the automatic measurement mode in which the DEP and EP measurements are carried out. After the completion of the measurement for each cell, a routine is invoked to let the cell fall freely within the monitor screen range and meanwhile the instantaneous cell position and time history are recorded. This measurement enables the sedimenting velocity of a particular cell to be determined and later be used to determine the absolute value of $\mathrm{Re}[\underline{K}_e]$ using Eq.(4.14). A typical DEP spectrum, plotted here as $\mathrm{Re}[\underline{K}_e]$ versus the frequency, is shown in Figure 5.1.

5.2 Source of Error

5.2.1 Errors due to "Signal Transmission Line"

It can be expected that the actual experimental data are subject to errors due to the non-flat frequency responses of the summing amplifier, the signal generators, and the signal cable lines, especially in the high frequency region. Therefore, appropriate connection and termination are required and the frequency response of the whole "signal

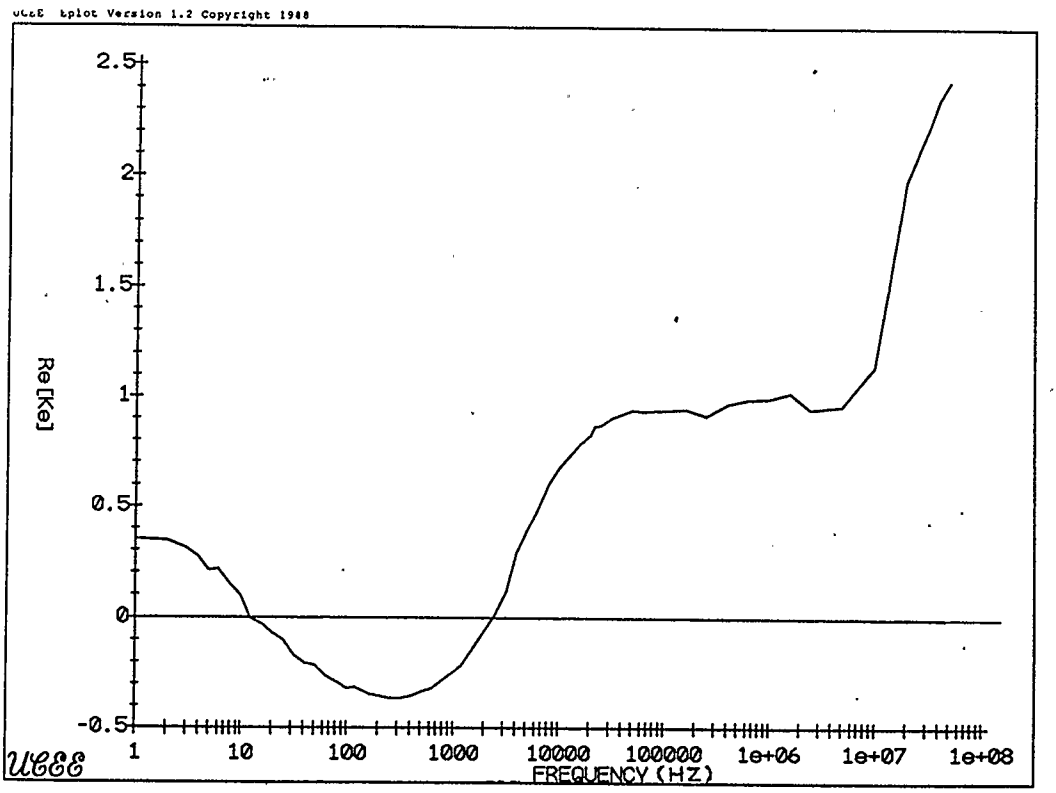

Figure 5.1. A typical original experimental DEP spectrum of *Canola* protoplast

transmission line" needs to be measured. The "transmission line" here is considered as the "black box" between the digital voltage input (from the computer) and the actual output (voltage between the two chamber electrodes). The measured frequency response of the "transmission line" is shown in Figure 5.2. These data were then used to correct the experimental data in the high frequency region (such as in Figure 5.1) and the corrected plot is shown in Figure 5.3.

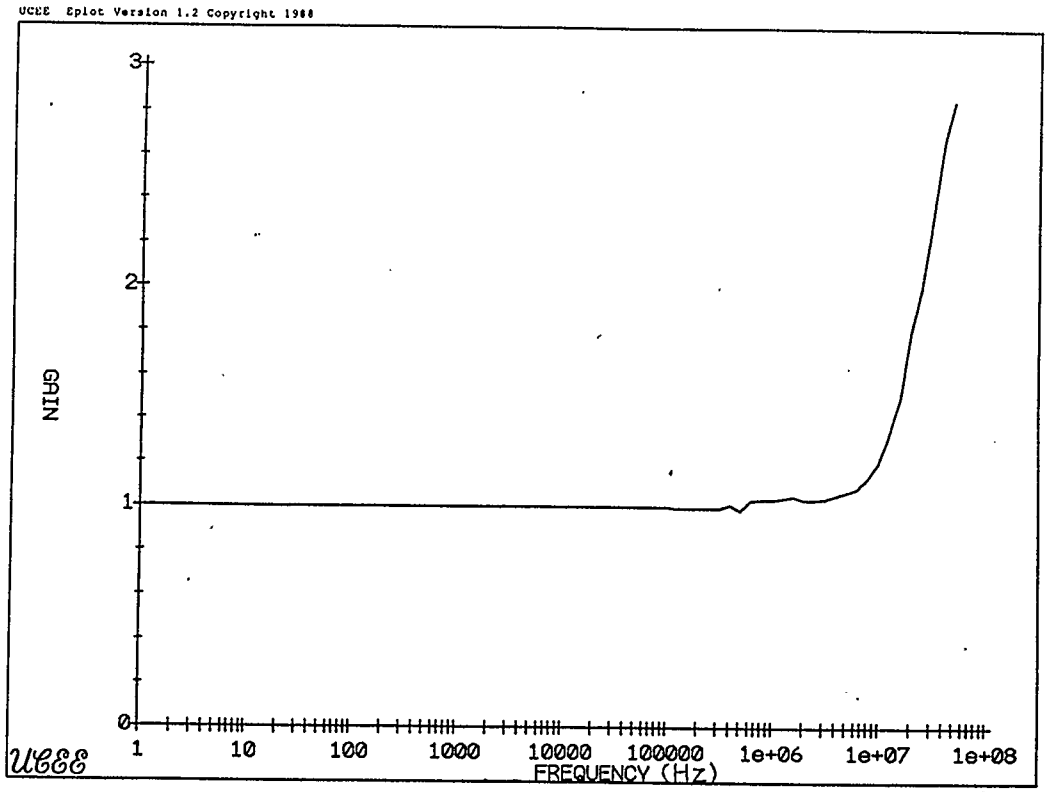

Figure 5.2. The measured frequency response of the "transmission line".

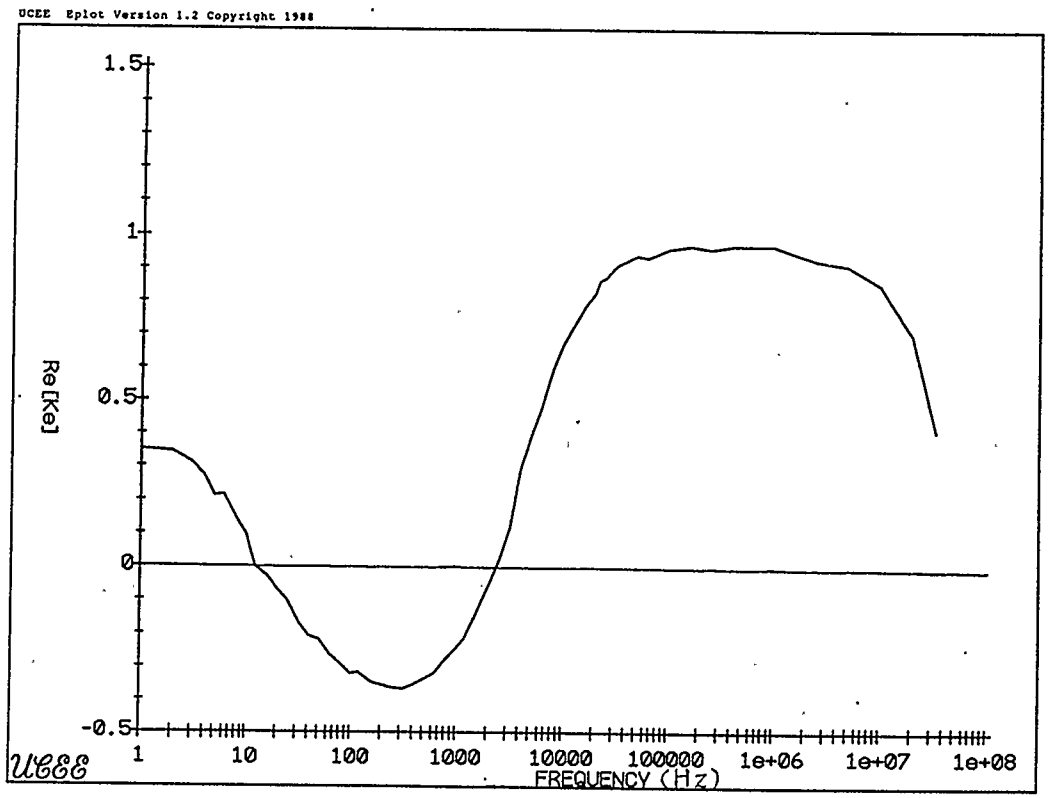

Figure 5.3. The corrected version of DEP spectrum in Figure 5.1

5.2.2 Error due to Electrode Polarization Impedance

It is known that when a metallic electrode is placed in an aqueous solution, there is a tendency for the metal ions to enter into the solution; there is also a tendency for the ions in the solution to combine with the electrode. Although details of such a reaction may be rather complex, depending on a variety of factors or conditions, the net result is a charge distribution at the electrode-electrolyte interface and its spatial arrangement depends on the way in which the electrode metal reacts with the electrolyte. The basic form of the charge distribution was conceived by Helmholtz, who described the electrical double layer, later called the Helmholtz layer. As a result of the particular charge distribution, the electrode acquires a potential. Although this electrode potential can cause problem in some bioelectric measurements (such as Electrocardiogram), it is, in our case, negligible compared to the applied voltage. The presence of a charge distribution at an electrode-electrolyte interface not only provides an electrode with a potential, it endows it with capacitance, since two planes of charge of opposite sign separated by a distance constitute a charged capacitor. Because the distance between the layers of charge is molecular in dimension, the capacitance is large, but it still presents relatively large impedance in the low frequency region, which in effect reduce the actually applied electric field in the medium and hence cause error in the measured quantities. Warburg was the first to demonstrate that an electrode-electrolyte interface could be equated to a series combination of resistance R_p and capacitance C_p; the value of each is frequency dependent. Schwan[54] investigated the influence of electrode polarization on biological impedance determinations by using this simple circuit model. Kell[55] suggested a more

appropriate circuit model which is independent of frequency. From the practical measurements and following discussion it is known that the electrode polarization impedance is not only dependent on the frequency but also on the electrode material, the conductivity of the electrolyte solution, and the current density. Therefore it is unnecessary to develop a general equivalent circuit model. Our interest is to find the contribution of the electrode polarization to the measured levitation spectrum and thereby appropriately account for it.

It is known that different electrode materials have different polarization effects. In our experiments, we coated the stainless steel electrodes with gold to reduce the electrode polarization effect. The actual frequency-dependent electrode polarization impedances for different medium conductivities were also measured. From our experiments we found that the magnitude of the polarization impedance Z_p is a function of the current density, i.e., the higher the current through electrode-electrolyte interface, the lower the polarization impedance Z_p. This observation is consistent with Schwan's result[54]. Based on the fact that the polarization impedance is dependent on both frequency and current-density, a electrode polarization impedance measuring system was designed and is shown in Figure 5.4. To keep the measuring conditions the same as in the real levitation experiments, V_B was always adjusted to the same value of V_f in Eq.(4.13) (the polarization effect always becomes pronounced in the frequency region where double frequency scheme is in operation) and kept constant when varying frequency. The whole chamber impedance, Z_e, which is the electrode polarization impedance plus the bulk impedance of the suspension, is then calculated as follows:

$$Z_e(\omega) = \frac{R_t \, 10^{\frac{Gain(\omega)}{20}}}{1 - 10^{\frac{Gain(\omega)}{20}}} \tag{5.1}$$

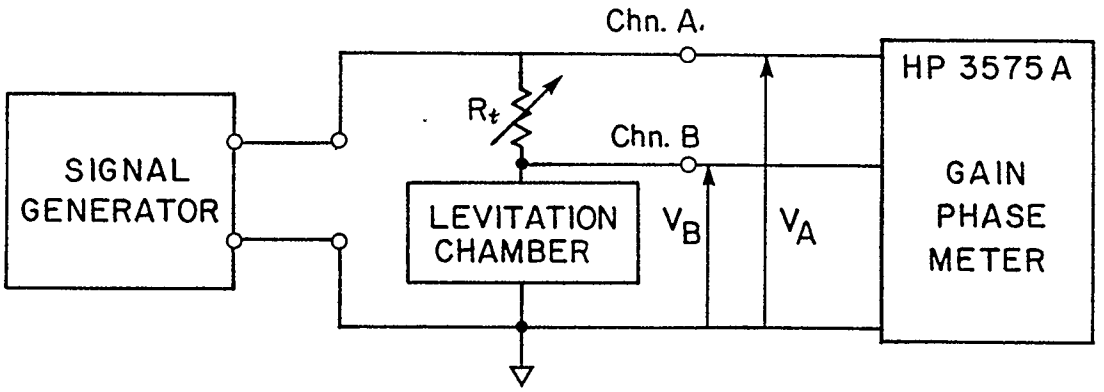

Figure 5.4. Block diagram of the instrumentation used to measure the characteristic impedance of the levitation chamber.

Figure 5.5 shows a typical frequency-dependent chamber impedance. From this impedance curve we can see easily that the flat portion represents obviously the bulk impedance of the suspension which is predominantly resistive because of the dilute suspension used in measurements. With the decrease of the frequency the polarization impedance comes into effect and becomes dominant at very low frequencies. Therefore it can be expected that at the low frequencies the actual field applied to the suspension would be reduced due to the occurrence and increase of the electrode polarization impedance, that means the actual magnitude of V_f in Eq.(4.13) is less than that applied.

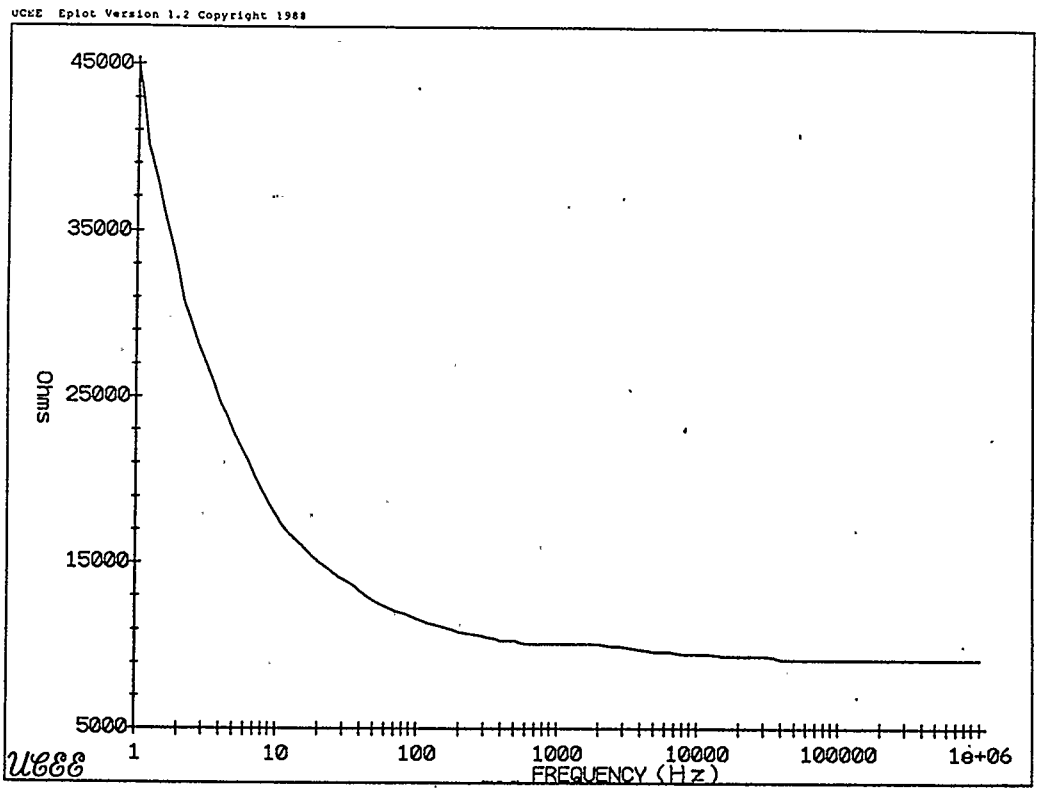

Figure 5.5. Plot of chamber impedance vs. frequency with medium conductivity = 108 μS/cm

Hence V_{eq} in Eq.(4.13) is subject to error and needs to be corrected. It is obvious that the actual voltage applied to the suspension (which is now represented by V'_f and corresponding to V_f in Eq.(4.13)) can be calculated by

$$V'_f = \frac{Z_{bs}}{Z_e} V_f = \frac{V_f}{K_z} \tag{5.2}$$

where Z_e is the chamber impedance, Z_{bs} is the bulk impedance of the suspension and $K_z = Z_e/Z_{bs}$ is, for convenience, here defined as *impedance ratio*. The value of Z_{bs} is considered as the magnitude of the flat portion of the measured Z_e~f curve. Figure 5.6 and 5.7 show the K_z~f curves for different medium conductivities and different cross-electrode voltage V_f. From these curves we can see that higher medium conductivity

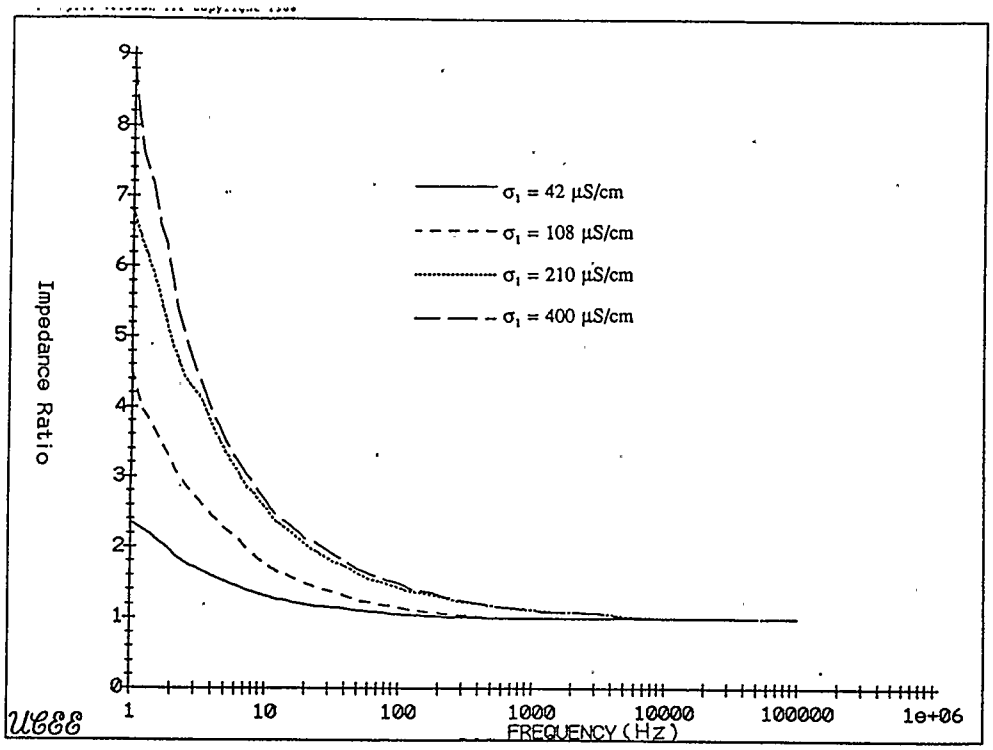

Figure 5.6. The impedance ratio vs. frequency for several medium conductivities.

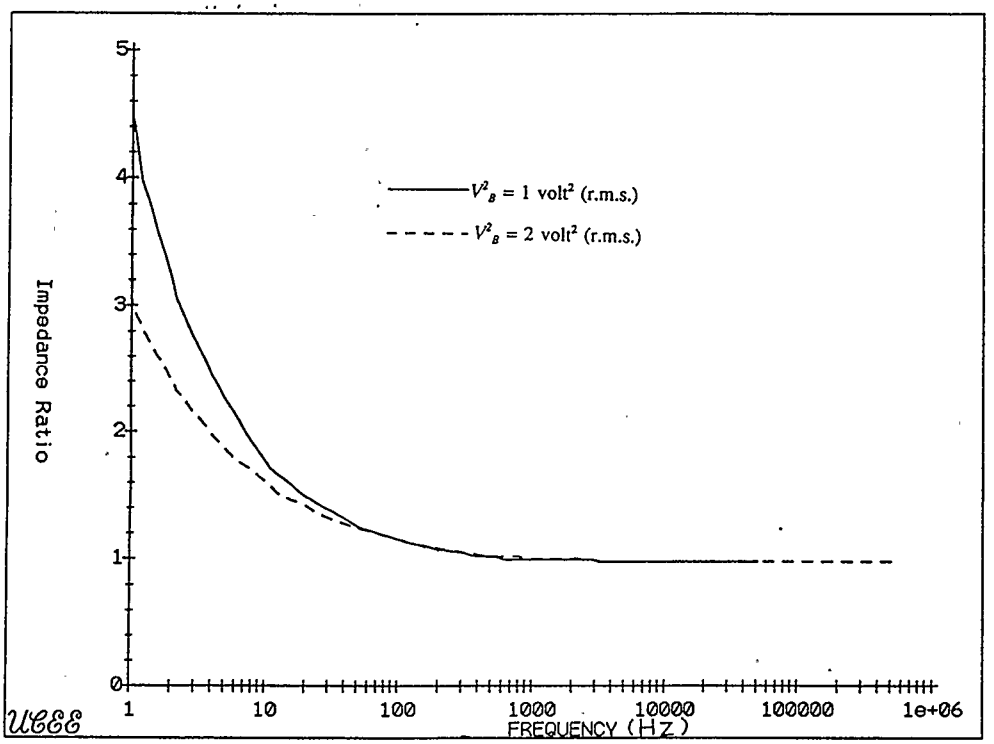

Figure 5.7. The impedance ratio vs. frequency for different voltages applied with the same medium conductivity of 108 μS/cm.

results in higher impedance ratio and higher V_f value results in lower impedance ratio. From Eq.(4.13) and (5.2), it is obvious that the corrected Re[$\underline{K}_e$] is simply given by the original Re[$\underline{K}_e$] multiplied by K^2_z. Figure 5.8 shows a typical example of the corrected and uncorrected DEP spectra. From the plots we can see that without correction, the low frequency DEP responses of the cell can be easily confused and lead to a false interpretation.

5.2.3 Error due to Heating Convection

During levitation experiments, it is found that under certain conditions, namely, high medium conductivity (> ~ 150 μS/cm) or higher low-frequency voltage V_f (2 volts in r.m.s.), there is a sharp decrease in Re[$\underline{K}_e$] in the low frequency region and beyond

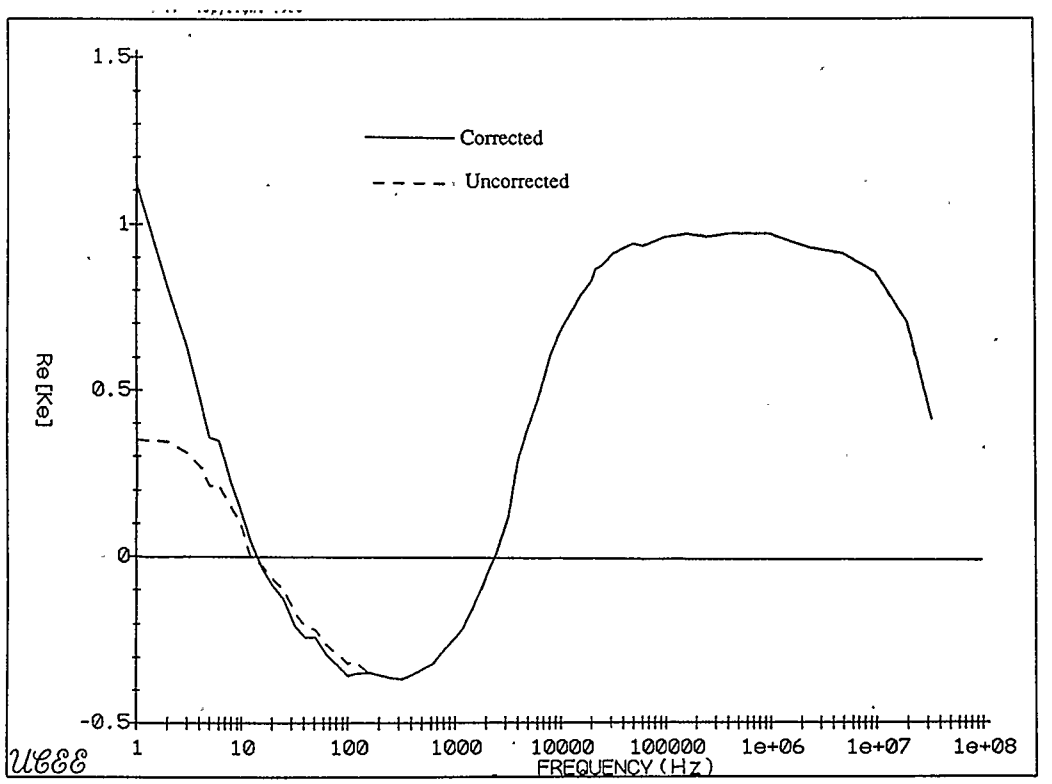

Figure 5.8. A typical example of corrected and uncorrected DEP spectra.

which, the cell can no longer be levitated (see Figure 5.9 and 5.10). This phenomenon suggests that there is a relatively strong downward force exerted on the cell. After several experiments and careful observations, we conclude that such an effect may be attributed to joule heating[20] which becomes more pronounced in the low frequency region. Figure 5.9 shows such effects caused by the increase of V_f and Figure 5.10 shows those caused by the increase of medium conductivity. It is difficult at present to quantify the contribution of the heating convection, because it is affected by several factors: medium conductivity, field intensity, and field frequency. However, by controlling some experimental conditions, e.g., reducing the applied low-frequency voltage V_f and limiting the medium conductivity, this contribution can be minimized. In order to obtain accurate

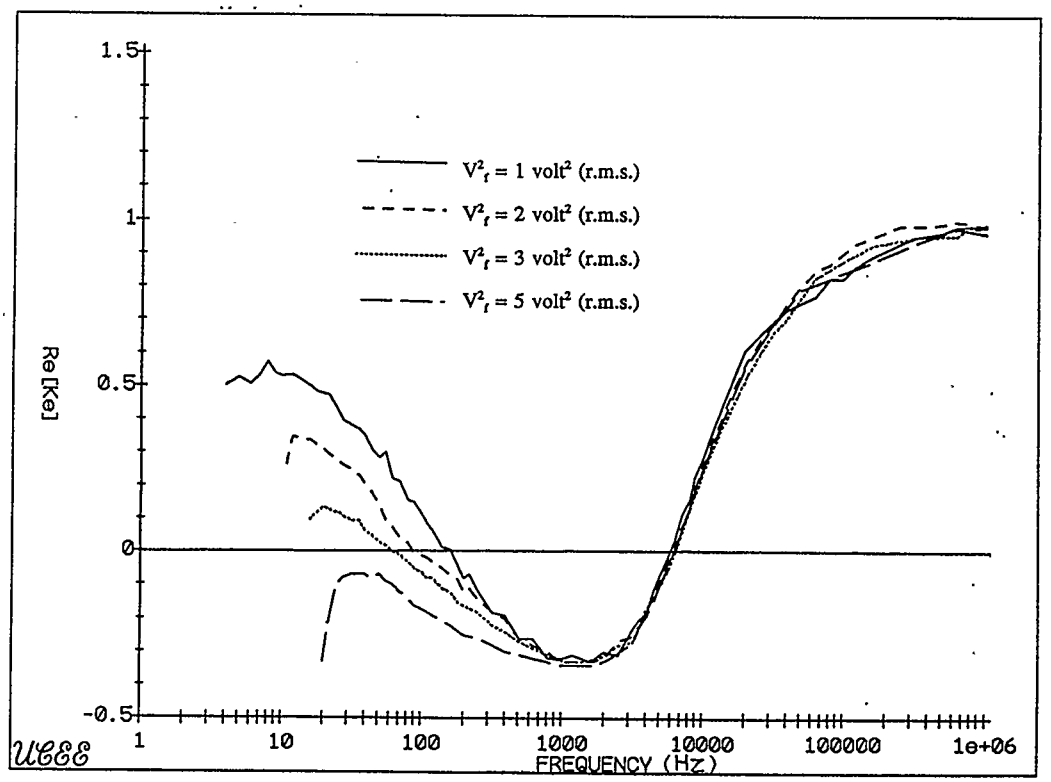

Figure 5.9. Influence of heating convection on measured DEP spectra (for different low-frequency voltage V_f).

measurements using double frequency levitation scheme, it is obvious that the low-frequency voltage V_f in Eq.(4.13) should not be too low. From experiments it is found that choosing $V_f = 1$ volt r.m.s. is an appropriate tradeoff between the accuracy of double frequency levitation scheme and the effect of joule heating.

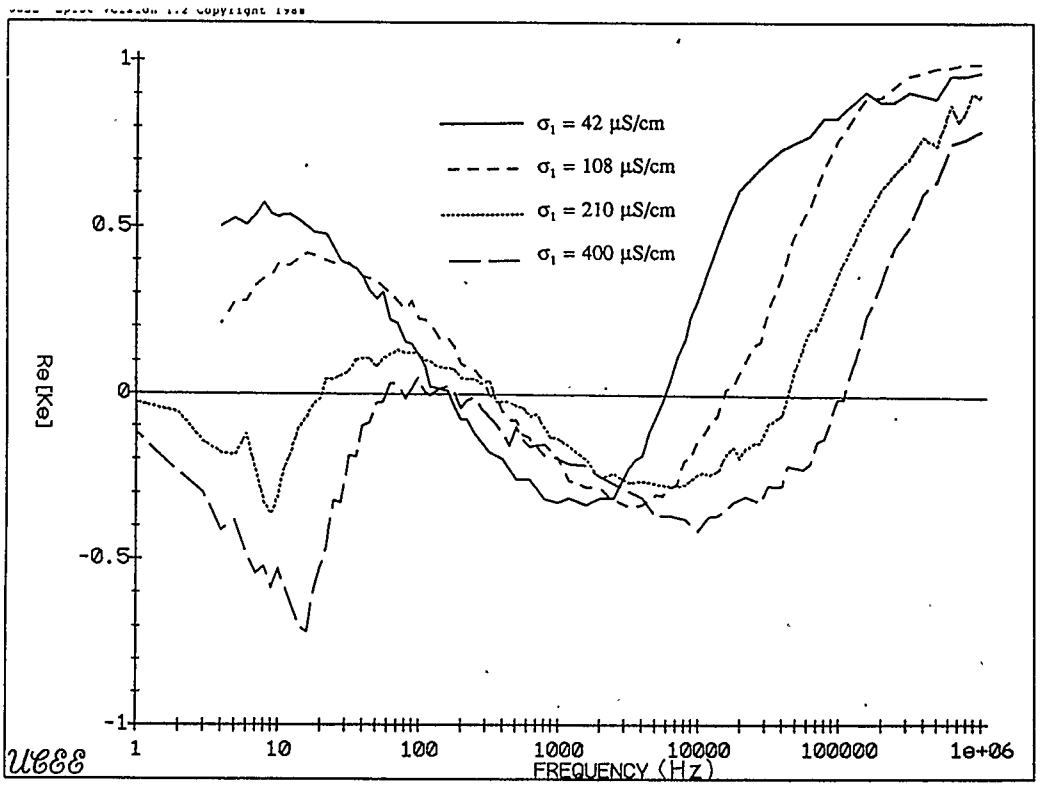

Figure 5.10. Influence of the heating effect on the measured spectra (for different medium conductivities).

CHAPTER 6

RESULTS, ANALYSIS and DISCUSSION

Frequency-dependent DEP levitation spectra were obtained for a number of *Canola* plant protoplasts, suspended in 8% sorbitol solution with various conductivities and *pH* values, over the frequency range of 1 Hz to 50 MHz. All such measurements were carried out at room temperature (22°C). A typical example of the DEP spectrum is shown in Figure 6.1. From the plot we can see that in the mid frequency region (from 20 kHz to 5 MHz) Re[$\underline{K}$] is positive and has a flat band. As the frequency decreases,

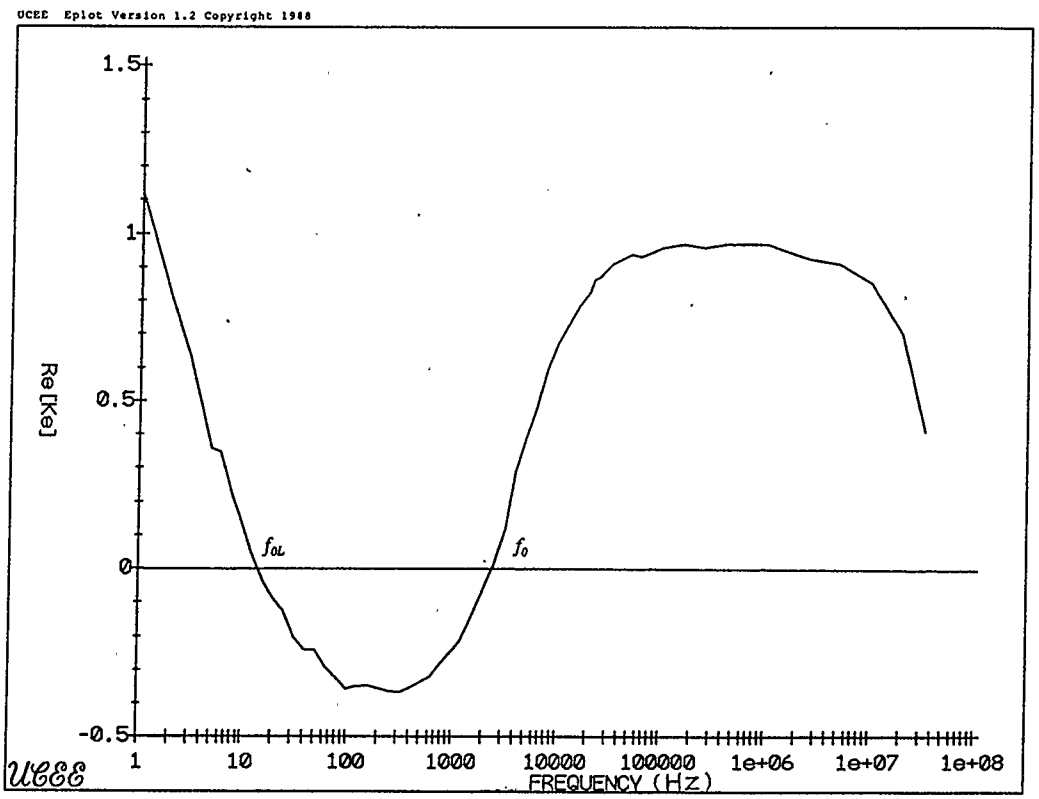

Figure 6.1. A typical experimental DEP spectrum for a single canola protoplast with σ_1 = 18 μS/cm, R = 22 μm, and *pH* = 5.88.

it experiences two major transitions. The higher frequency relaxation (around 25 MHz), as predicted by the shelled spherical model (see Figure 3.4), is also observed. Comparing Figure 6.1 with Figure 3.4a, we can see that the theoretical shelled spherical model can well represent the real biological cells in the mid and high frequency regions (from hundreds of Hz to 50 MHz). The only difference between the theoretical and experimental spectra occurs in the low frequency region. In the theoretical spectrum, after the mid-frequency positive/negative transition, Re[$\underline{K}_e$] tends to approach -0.5, as the frequency decreases. In the experimental spectrum, however, after this transition, Re[$\underline{K}_e$] exhibits a negative peak and leads to positive again. This rise in Re[$\underline{K}_e$] represents another relaxation process in the low frequency region and is possibly due to the surface charge associated counterion polarization (or electrical double layer), which has been intentionally ignored in the shelled spherical model. As discussed in Chapter 3, there are several models accounting for such surface charge mediated polarization mechanism. However none of them are based on the measurements of single cell (particle) but on the experiment data of suspension method. Therefore our experimental spectra can provide direct verifications of those models without resorting to any other theories (such as the mixture theory, as in the case of suspension method, which itself is only suitable for the very dilute suspension). This low frequency behaviour will be discussed further in later section.

6.1 Medium Conductivity and Cell Radius Dependencies of DEP Spectra

Experiments were performed for several different medium conductivities at a fixed *pH* value of 5.88. The conductivity of the suspending medium was adjusted by adding KCl

and measured by a conductivity meter (model No. 1710, Bio-Rad Laboratories Inc., Richmond, CA). The measured spectra are shown in Figure 6.2. From Figure 6.2a we can see that varying the medium conductivity does not influence the high frequency relaxation region (around 25 MHz). This behaviour is consistent with the theoretical prediction of the shelled spherical model. From Figure 6.2a,b we can see that the medium conductivity has a significant effect on both mid-frequency relaxation and low-frequency relaxation, i.e. the cross-zero frequencies f_0 and f_{0L}. With the increase of the medium conductivity, f_0 shifts towards high frequency, as theoretically predicted in the shelled spherical model.

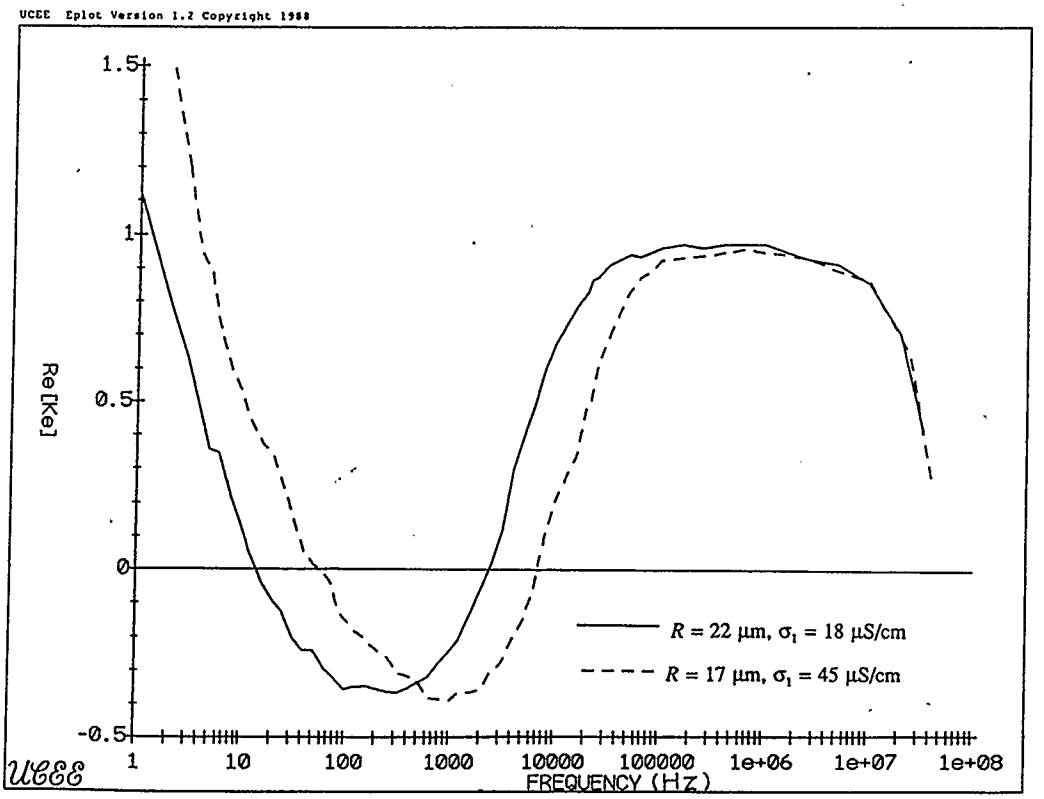

Figure 6.2a. Experimental DEP spectra for different medium conductivities (pH=5.88).

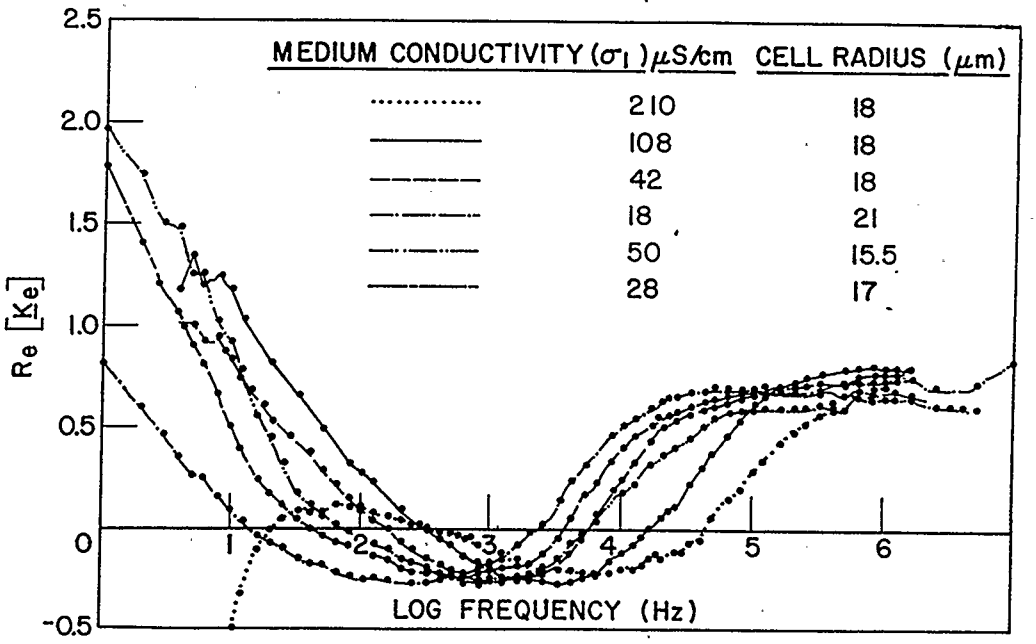

Figure 6.2b. Experimental DEP spectra for different medium conductivities (pH = 5.88).

Another experimentally variable parameter is the cell radius. By performing the levitation experiments on the cells of different sizes and keeping other parameters constant, we obtained the radius-dependent DEP spectra, as shown in Figure 6.3. The effects of cell radius on both the magnitude and cross-zero frequency f_0 are consistent with the model prediction (see Figure 3.4b).

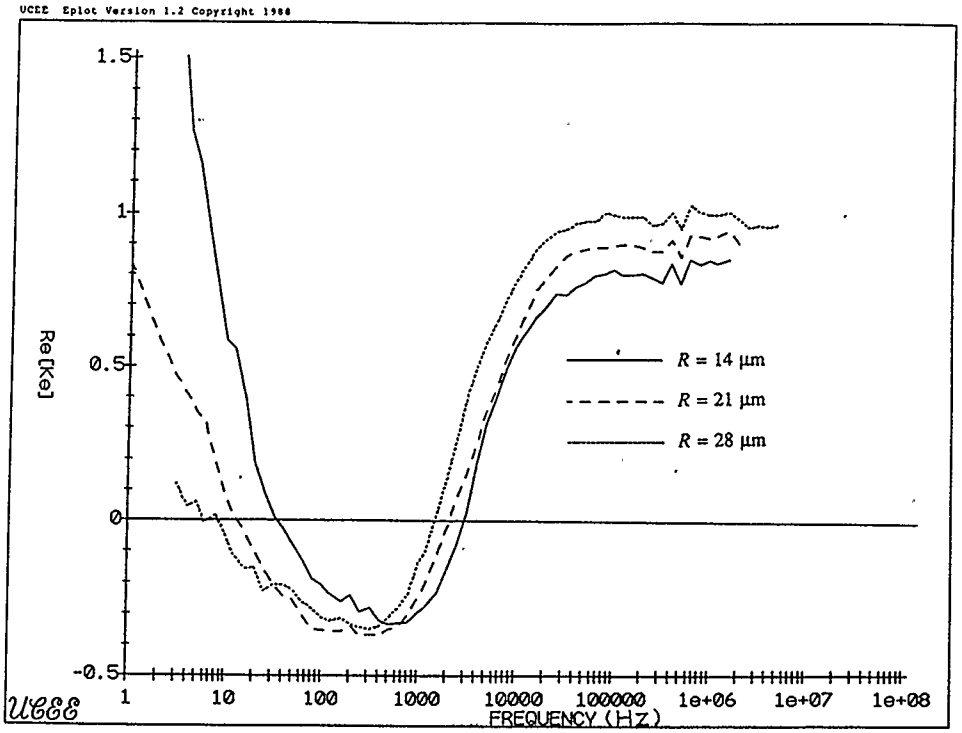

Figure 6.3. Experimental DEP spectra for different cell radii (σ_1 = 18 μS/cm, *pH* = 5.88).

6.2 Extraction of Cellular Parameters

From the theoretical plots shown in Figure 3.4 and earlier discussion in Chapter 3, we know that the relaxation time in the high frequency region is principally determined by the cytoplasm conductivity. This is also reflected in Eq.(3.11). With such information at hand, an estimate of cytoplasm conductivity of *Canola* plant protoplast is obtained by fitting the theoretical plot to the experimental data, as shown in Figure 6.4. The cytoplasm conductivity obtained is approximately 4000 ± 200 μS/cm.

As discussed in Section 3.2.2, the membrane capacitance can be determined by Eq.(3.22). Although this relation can provide theoretical guidance, it is, however,

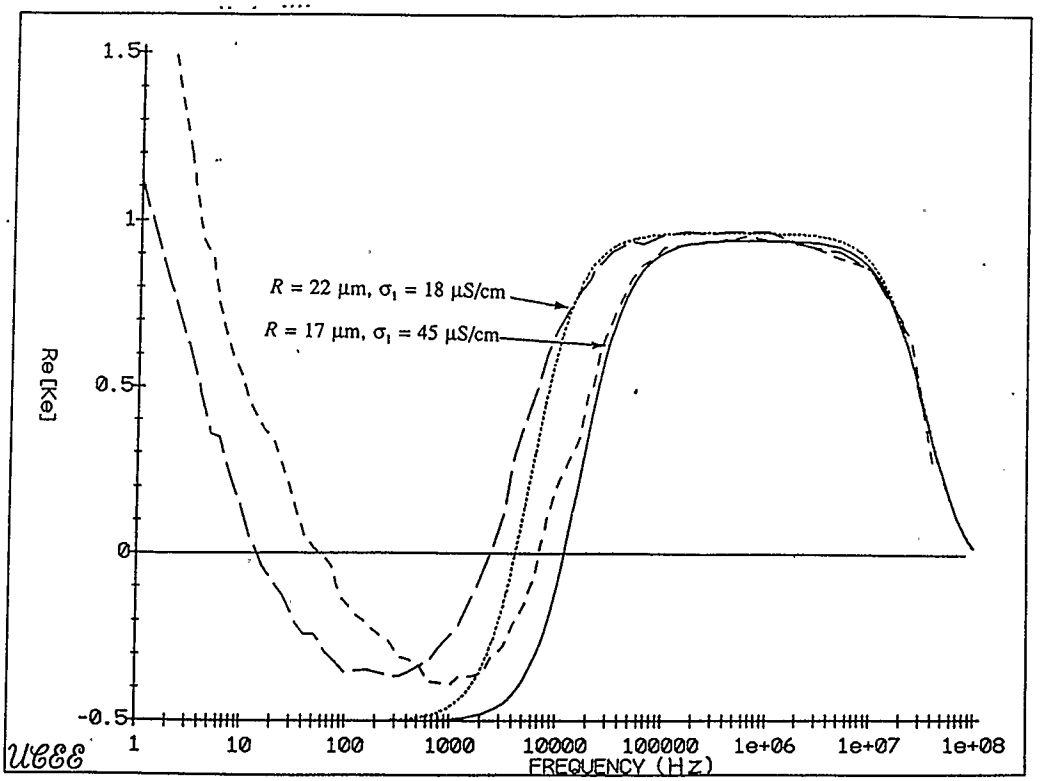

Figure 6.4. Comparison of experimental DEP spectra with their corresponding theoretical counterparts. For the parameters assigned to both theoretical spectra, σ_2 is 4000 μS/cm; R and σ_1 are the same as their experimental counterparts, the rest are the same as the typical values in Chapter 3 (see page 18).

obtained based on several approximations, especially the approximation of $\sigma_m \approx 0$. Therefore it is necessary to evaluate the validity of Eq.(3.22) and to find the contribution of σ_m to the cross-zero frequency f_0 so that we might be able to develop a method to estimate the magnitude of membrane conductivity σ_m in addition to membrane capacitance. In order to do this we have to find the rigorous relations of $f_0 \sim \sigma_1$, $f_0 \sim R$, $f_0 \sim C_m$, and $f_0 \sim \sigma_m$. However, most of these relations can hardly be derived analytically. For this reason, a program has been developed to calculate and find the cross-zero frequency f_0 based on the shelled spherical model (Eqs.(3.14) and (3.15)). For each set

of the calculated data (e.g. f_0~σ_1), except the variable (e.g. σ_1) , all other parameters (unless specified) were assigned the same typical values as in Section 3.2.1 (see page 18). The calculated data sets were then fitted, using least-squares regression with *Microsoft Chart* software package, to either power or linear functions. Table 1 shows these fitted resultant functions. It is found that each set of the calculated data can fit quite well to its corresponding function (with all the *correlation coefficients* above 0.96 and *standard error of prediction* below 1%). Figure 6.5 shows the worst case of the fittings (i.e., has least *correlation coefficient* and highest *error of prediction* values). From Table 1 we can see that the membrane conductivity has significant effects on the f_0~R, f_0~C_m, and f_0~σ_1 relations. The effect of σ_m on f_0~σ_1 relation is also shown in Figure 6.6. When σ_m is in the range of 1 μS/cm or greater, Eq.(3.22) is no longer considered to be valid. Therefore

Table 1 Calculated Relations between f_0 and Cellular Parameters

	f_0~R (R=10~28)	f_0~C_m (c_m=0.2~0.8)	f_0~σ_1 (σ_1=10~400)	f_0~σ_m (σ_m=0.01~10)
σ_m = 0.01	$f_0 = 43646\ R^{-0.99}$	$f_0 = 1300\ C_m^{-0.99}$	$f_0 = 250\ \sigma_1$	*N/A*
σ_m = 0.1	$f_0 = 38928\ R^{-0.92}$	$f_0 = 1455\ C_m^{-0.93}$	$f_0 = 268\ \sigma_1$	*N/A*
σ_m = 0.1 (σ_1=400)	$f_0 = 1510822\ R^{-0.92}$	$f_0 = 119158\ C_m^{-0.60}$	*N/A*	*N/A*
σ_m = 1.0	$f_0 = 23188\ R^{-0.56}$	$f_0 = 3073\ C_m^{-0.60}$	$f_0 = 449\ \sigma_1$	*N/A*
σ_m = 2.0	$f_0 = 20581\ R^{-0.39}$	$f_0 = 4956\ C_m^{-0.44}$	$f_0 = 636\ \sigma_1$	*N/A*
σ_1 = 10	*N/A*	*N/A*	*N/A*	$f_0 = 2581(1+0.763\sigma_m)$
σ_1 = 400	*N/A*	*N/A*	*N/A*	$f_0 = 99970(1+0.766\sigma_m)$

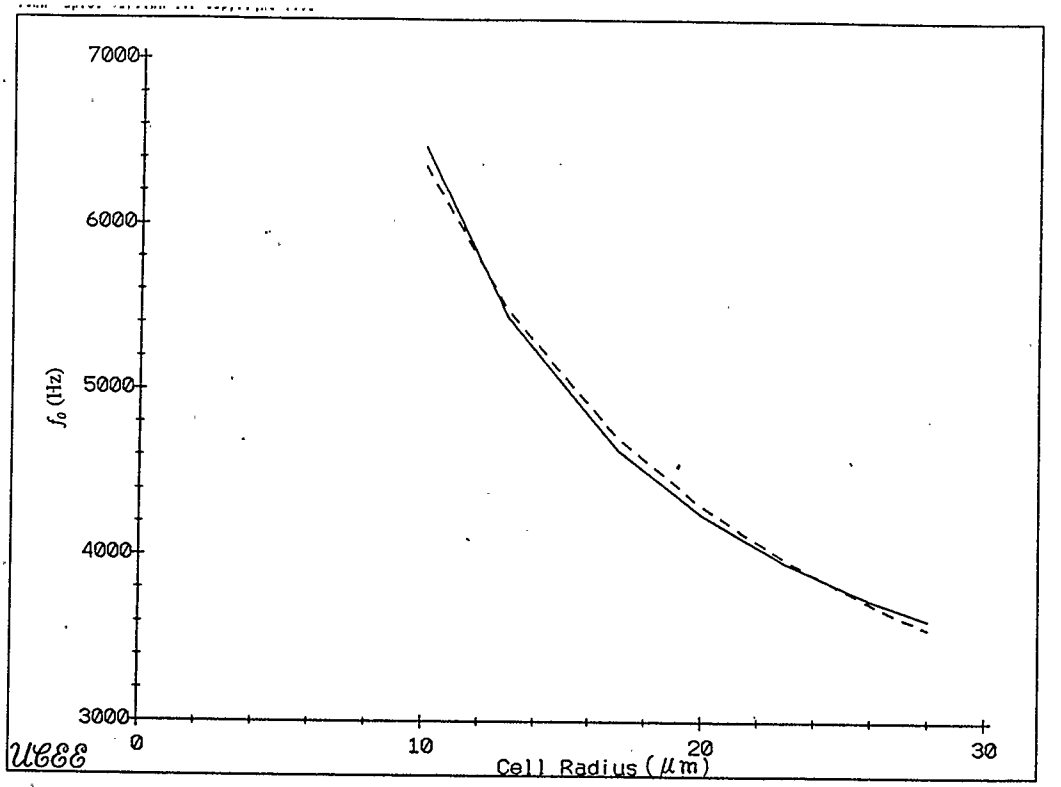

Figure 6.5. An example of curve fitting for f_0~R relation when σ_m = 2.0 μS/cm.

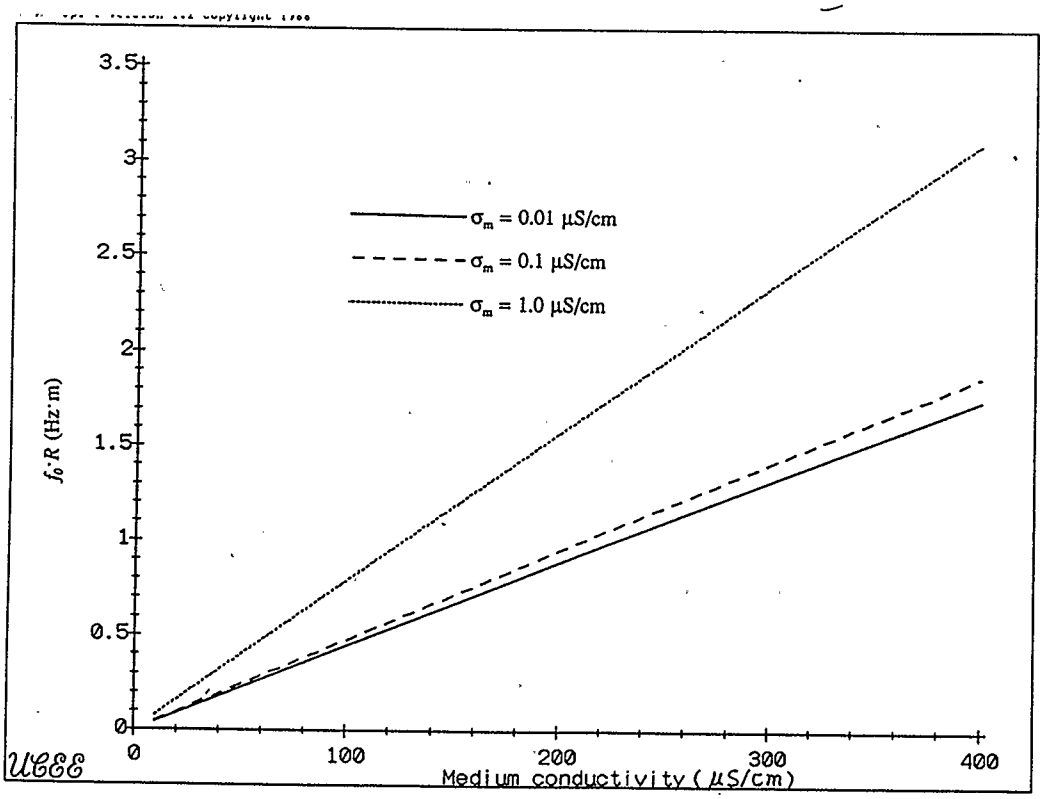

Figure 6.6. Effect of membrane conductivity on the slope of $f_0 \cdot R$~σ_1 plots

Therefore it can not be used to estimate the membrane capacitance. If, however, the membrane conductivity is in the range of 0.1 μS/cm or less, then Eq.(3.22) is quite consistent with the rigorously calculated relations. Therefore Eq.(3.22) can be used to estimate the membrane capacitance. As for the estimate of the possible range of the membrane conductivity, we can see, from the table, that the power of the fitted f_0~R function is a relatively sensitive parameter which can reflect the changes of the membrane conductivity and is also experimentally achievable. In addition, this power parameter is independent of the medium conductivity. We can also see, from the fitted relation of f_0~σ_m in Table 1 and Figure 6.6, that the contribution of σ_m become negligible if $1 \gg 0.76\sigma_m$, or $\sigma_m \ll 1.3$ μS/cm.

By determining the cross-zero frequencies in Figure 6.3, we obtained the experimental f_0~R data series. It was also fitted to a power function and the resultant function is described by the following relationship:

$$f_0 = 43435\ R^{-1.006}$$

Comparing the power value of the above equation to its counterpart in Table 1, we can infer that the actual membrane conductivity is very small (less than 0.1 μS/cm). Therefore, Eq.(3.22) can be effectively used to derive the membrane capacitance. By the determination of the slope value of the experimental $f_0 \cdot R$~σ_1 plot, which is obtained from Figure 6.2 and shown in Figure 6.7, the specific membrane capacitance thus derived is 0.55 ± 0.02 μF/cm^2.

From Figure 6.6 it can be seen that besides the membrane capacitance, the membrane conductivity also has an effect on the slope of f_0~σ_1 plot. To verify this behaviour,

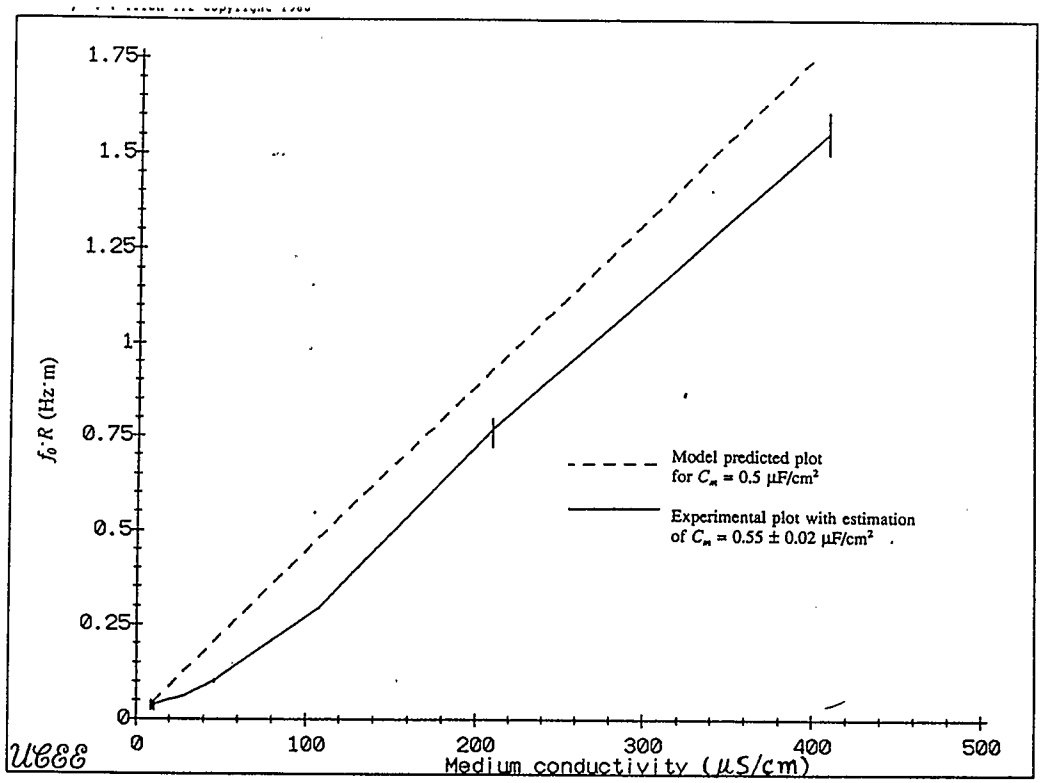

Figure 6.7. Comparison of theoretically predicted and experimentally obtained $f_0 \cdot R \sim \sigma_1$ plots

experiments were conducted (by Jack Yang in our research group) on protoplasts which had previously been subjected to saponin treatment. Saponin treatment is known to produce pores in the plasma membrane[22], hence the trans-membrane conductivity is expected to increase as a result. In our experiments, the *Canola* protoplasts were subjected to saponin treatment for 30 min at room temperature with the concentration of 900 μg/ml. Figure 6.8 shows the experimental plots of $f_0 \cdot R \sim \sigma_1$ for both the treated and untreated protoplasts. It can be seen that the saponin treatment has resulted in the increase of the slope of $f_0 \cdot R \sim \sigma_1$ plot, which confirms the increase in the trans-membrane conductivity

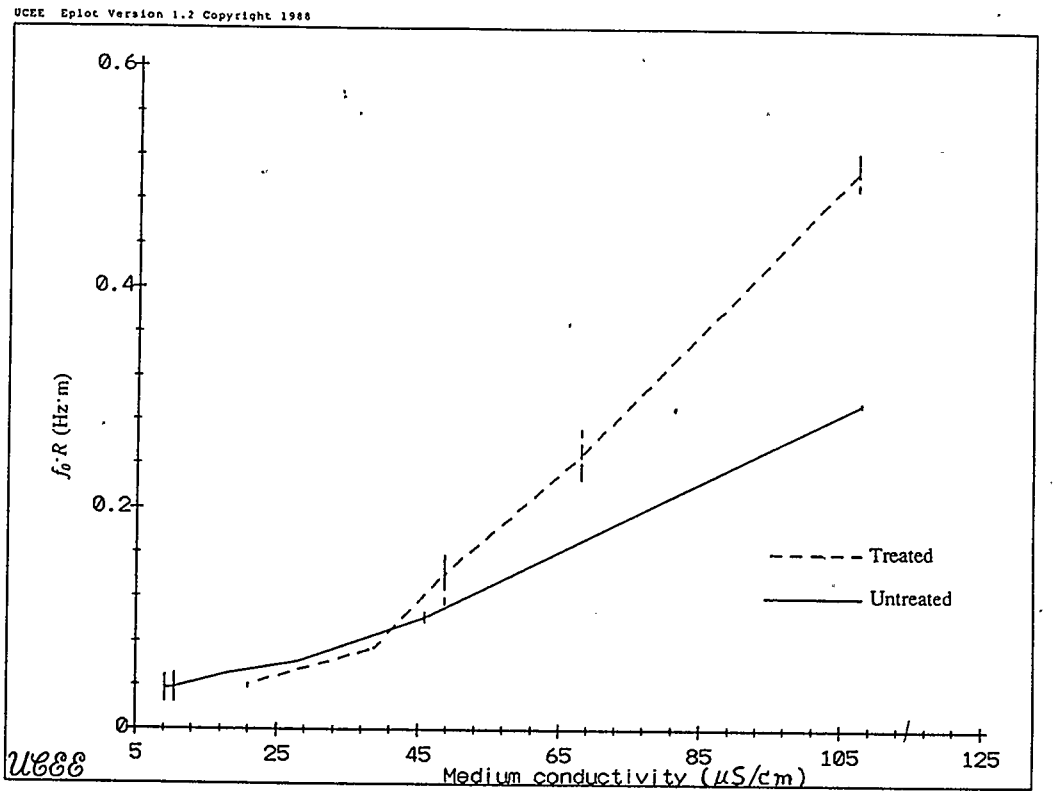

Figure 6.8. $f_0 \cdot R \sim \sigma_1$ plots of *Canola* protoplasts with and without saponin treatment

(compared with the theoretical prediction in Figure 6.6) after the treatment. By comparing with the theoretically predicted plot (such as those shown in Figure 6.6), it has been estimated that the membrane conductivity has increased to approximately 1 μS/cm.

6.3 The Low Frequency Behaviour of DEP Spectra for *Canola* Protoplasts

As we mentioned in the beginning of this chapter, after the positive/negative transition (f_0) as the frequency decreases, Re[$\underline{K}_e$] exhibits a negative peak and then goes up again. This negative peak has a value of around -0.35 rather than -0.5 as predicted in the shelled spherical model. Because in this frequency region Re[$\underline{K}_e$] is determined by the difference between σ_{eff} (the effective conductivity of the cell) and σ_1 (see Eq.(3.13)), therefore the

value of -0.35 indicates that σ_{eff} has a value comparable to σ_1. This behaviour has been attributed to the presence of a finite surface conductivity (conductance)[56] which is possibly associated with the surface charge mediated counterion distribution in response to the applied field. In such a case, the effective conductivity of cell can be expressed as[57]

$$\sigma_{eff} = \sigma_m + \frac{2K_s}{R} \tag{6.1}$$

where K_s is the membrane surface conductance. It is obvious that σ_m is negligible compared with the surface conductivity (second term in above equation) in the negative peak frequency region. From Figure 6.2 we can see that the negative peak values in the Re[$\underline{K}$] plots are almost independent of medium conductivity σ_1. Since in this frequency region Re[$\underline{K}$] is determined by σ_{eff} and σ_1 (see chapter 3), according to Eq.(3.13) we can obtain:

$$\sigma_{eff} = \frac{1 - 2\times0.35}{1 + 0.35}\sigma_1 \approx 0.22\,\sigma_1 \tag{6.2}$$

From above equation we know that σ_{eff} (or K_s) is linearly related to σ_1. By now a possible question might be asked by the careful reader: does the surface conductivity have the same effect on the slope of $f_0 \cdot R$~σ_1 (see Figure 6.6) as σ_m does? From Figure 6.4 we can conclude that the mismatches of f_0's between the theoretical and experimental plots are due to the presence of the surface conductivity. These mismatches, reflected on the $f_0 \cdot R$~σ_1 plot, are the downward shift of the plot (see Figure 6.7) rather than the change of the slope. These different effects between the trans-membrane and surface

conductivities are due to the fact that the surface conductivity, unlike trans-membrane conductivity, is determined by the medium conductivity. Therefore, by extending the $f_o \cdot R \sim \sigma_1$ plot obtained with relatively high medium conductivity data ($\sigma_1 > 50$ μS/cm) to the y axis, the y-intercept value gives an estimate of the contribution of the surface conductivity.

It is obvious that the surface conductivity is frequency dependent, i.e., it becomes effective in a certain frequency region and increases as frequency decreases, which accounts for the increase of Re[$\underline{K}_c$] in the low frequency region. This frequency dependence gives rise to another distinct relaxation process in the low frequency region. Without getting into detailed mathematical analysis of its physical and chemical origins, we can interpret this relaxation behaviour as follow: Due to the presence of the net charge on the cell surface and the presence of the membrane potential, the ions (mainly counterions) in the medium would accumulate around the cell surface, forming an electrical double layer. When the frequency of the applied field is high enough, these ions can not respond to the field, i.e., to the external observer, there is no net transport of ions around the cell surface, hence no surface current (or surface conductance); As the frequency decreases, these ions start (and more and more easily) to move in response to the applied field, hence to the external observer, a frequency-dependent surface current (surface conductivity) would be seen. Grosse[38] and Kaler *et al*[58] have studied the theoretical aspects of such a behaviour and found that such a frequency-dependent surface conductivity has the same characteristics as the first-order relaxation, which is qualitatively in agreement with our experimental results. Our results have shown that the

medium conductivity influences both the relaxation frequency (f_{0L}) and the magnitude of this low frequency response, and that the cell radius also affects these quantities. Burt and Pethig[22] also observed similar rising trend in the low frequency region (less than 200 Hz). By comparing their results with previous cell micro-electrophoresis data for the same type of the cells and same biochemical treatment, they conclude that this low frequency response appears to be primarily influenced by the cell surface charge[22].

6.4 Effects of Medium pH on the DEP Spectra

In addition to the effects of cell size and suspending medium conductivity, the influence of the medium *pH* on the DEP spectra was also experimentally examined over the *pH* values ranging from 4.6 to 8.0, as shown in Figure 6.9. It is observed that the magnitude of the low frequency polarization response is *pH* sensitive, although both the low (f_{0L}) and the mid (f_0) cross-zero frequencies are virtually unaffected. It is known[31] that *pH* influences on the degree of ionisation of certain protein groups, hence changing the amount of the surface charge. This has been confirmed with our electrophoretic measurement method, and the preliminary results are shown in Table 2. All measured surface charges are negative. From Table 2 it is shown that around physiological *pH* value (approx. 6.05) the *Canola* protoplasts have the lowest surface charge density. As the medium *pH* is increased or decreased above or below this value, the surface charge density increases. The latter effect is more evident as the medium becomes more basic. The fact that at the physiological *pH* the protoplasts have the lowest charge density is probably related to the observed phenomena that the DEP spectrum for $pH = 6.05$ has the lowest magnitude in the positive flat band region (see Figure 6.9). By measuring the

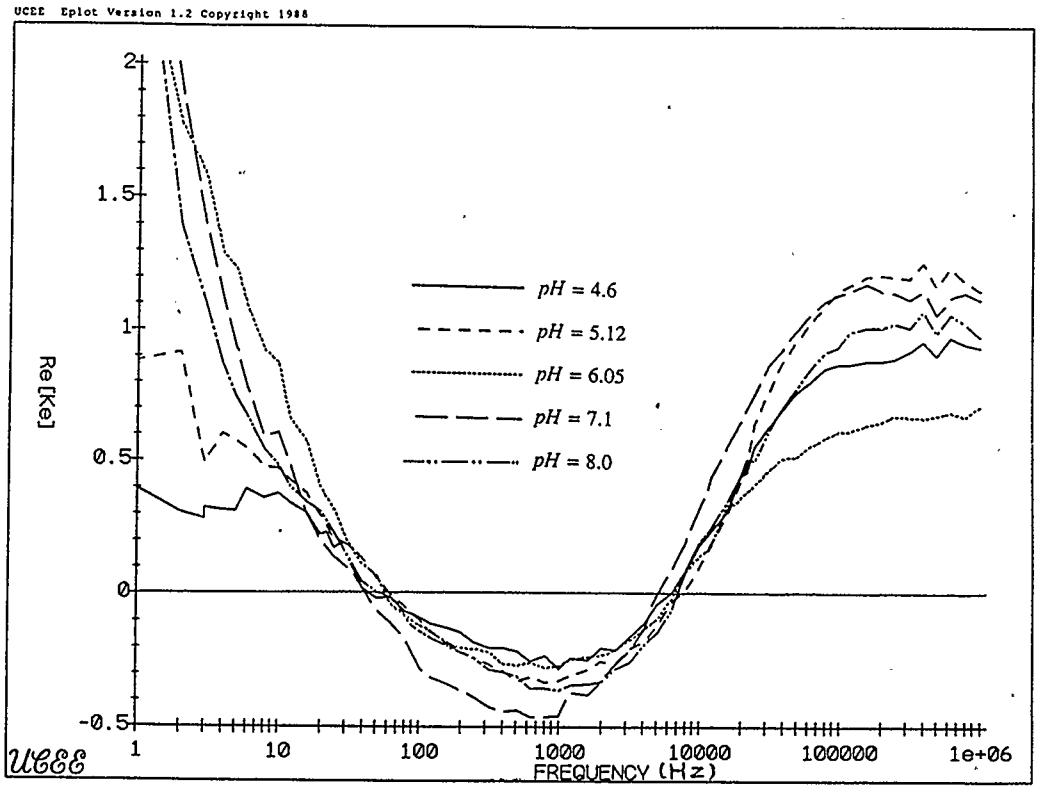

Figure 6.9. The influence of medium *pH* on the DEP spectra of *Canola* protoplasts with the medium conductivity of 45 μS/cm and R = 17~18 μm

Table 2. Measured Surface Density Indices at Various *pH* Values

pH values	4.6	5.12	6.05	7.1	8.01	8.9
Surface charge density indices	21.0	17.8	3.2	23.4	31.7	43.3

DEP spectrum twice for each single cell, it is also observed that the DEP spectra for *pH* = 6.05 has the highest repeatability in the flat band region. The DEP spectrum for *pH* = 4.6, however, has shown distinct difference in the magnitude between the first and

second runs (see Figure 6.10). For the second-run measurements, all the measured surface charge densities are significantly smaller than those obtained in the first run, and these decreases in the measured surface charge only occur when the first levitation measurements are carried out through the low frequency region. This phenomenon possibly suggests that these charged membrane protein groups tend to lose charge under the electrically induced mechanical stretching under the low frequency field, especially when the medium *pH* is low (see Figure 6.9). This may also explains why the low frequency magnitudes of the DEP spectra for low *pH* are lower than that for higher *pH* values: Due to the easier depletion of the surface charge in the low *pH* medium and low frequency field (less than 20 Hz), the counterion-charge concentration would decrease and hence reduces the surface conductivity, which accounts for the lower Re[$\underline{K}_e$] magnitude in that frequency region in the lower *pH* medium.

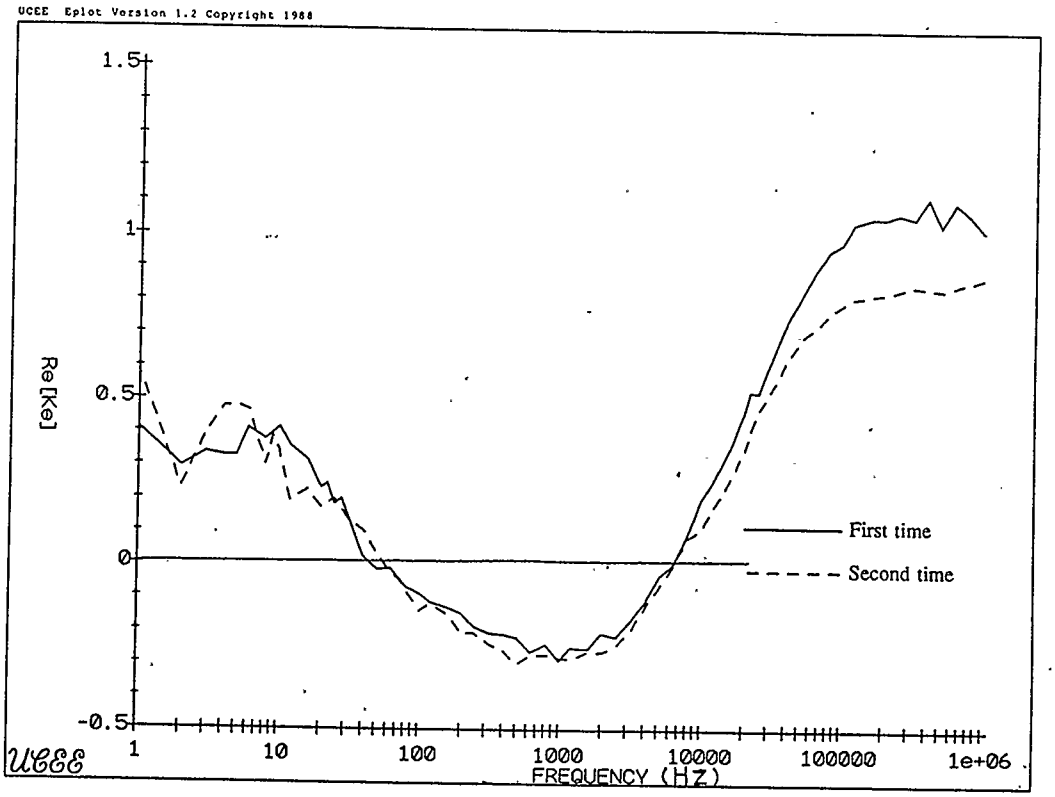

Figure 6.10a. Two consecutively measured DEP spectra at pH = 4.6, σ_1 = 45 µS/cm

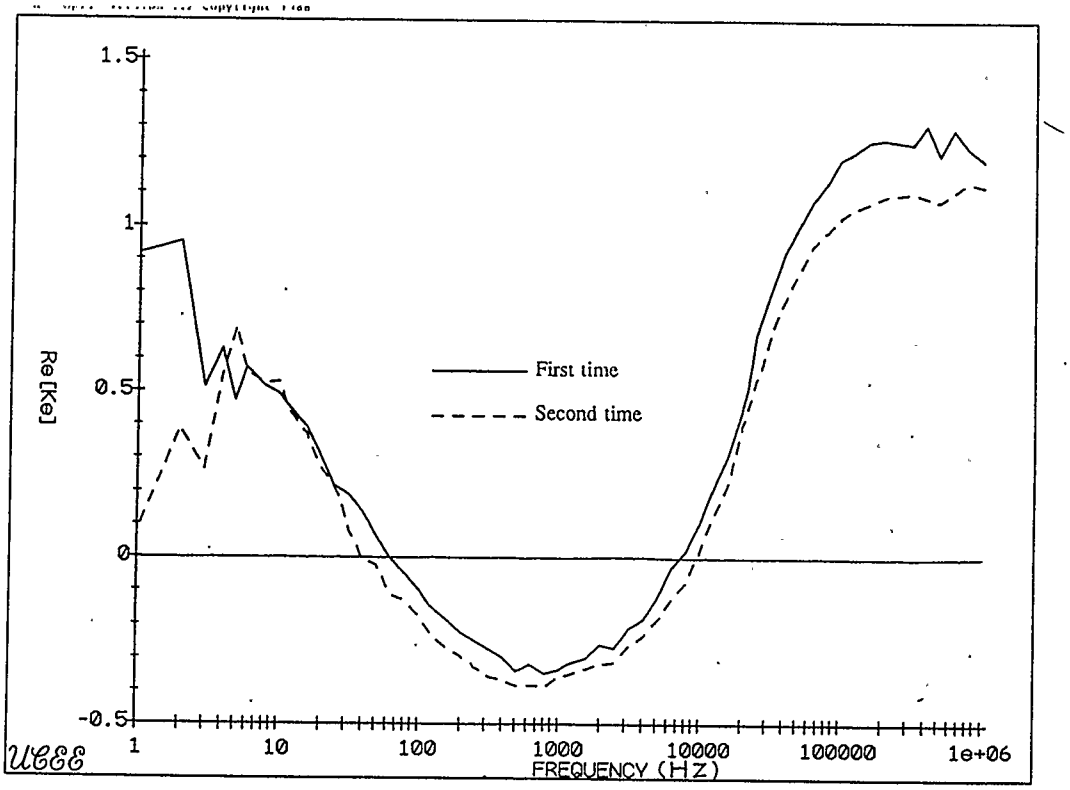

Figure 6.10b. Two consecutively measured DEP spectra at pH = 5.12, σ_1 = 45 µS/cm

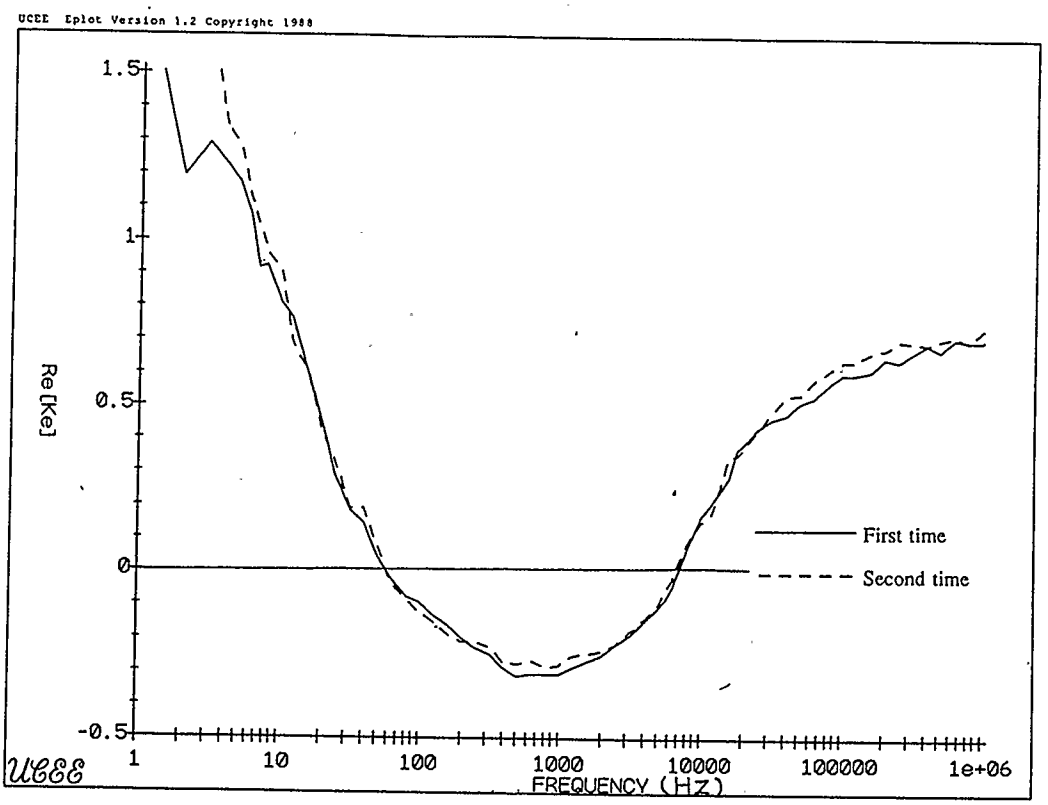

Figure 6.10c. Two consecutively measured DEP spectra at pH = 6.05, σ_1 = 45 μS/cm

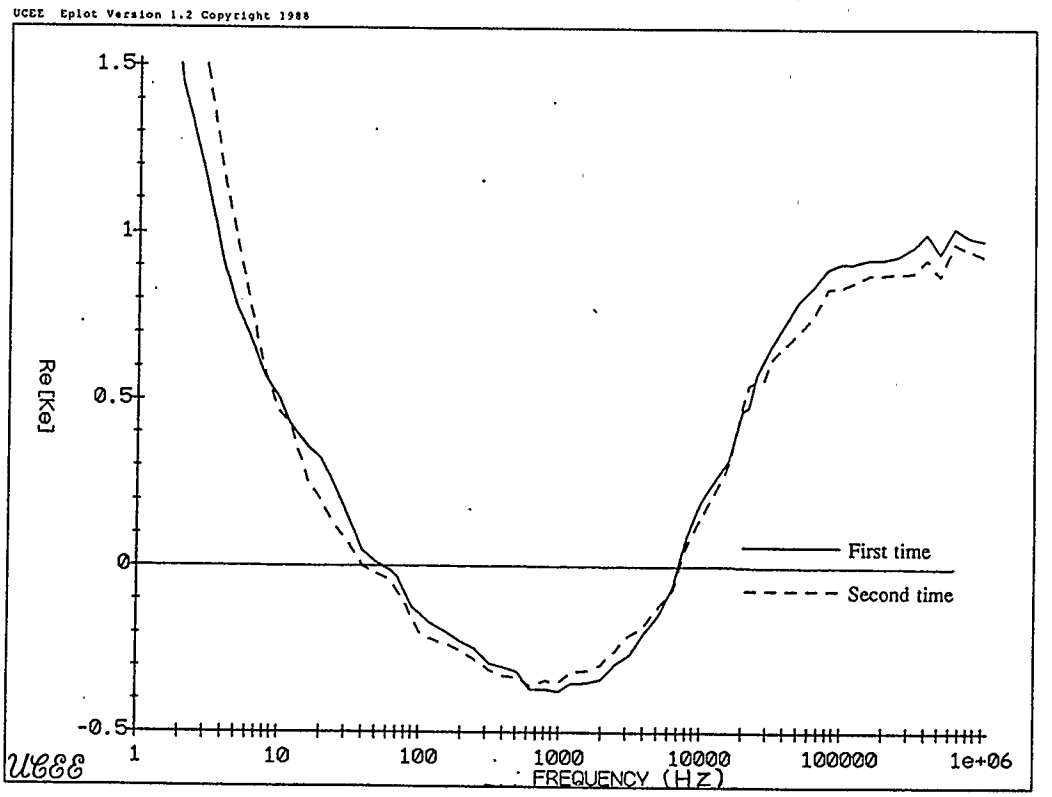

Figure 6.10d. Two consecutively measured DEP spectra at pH = 8.0, σ_1 = 45 μS/cm

CHAPTER 7

Conclusions

7.1 Summary of Accomplishments

In this thesis several accomplishments have been made: Methodologically, a double frequency levitation scheme has been proposed and implemented based on the previous DEP levitation system, which has been proved to be capable of measuring the DEP spectra of individual biological cells in both the positive and negative DEP frequency regions An electrophoretic measuring scheme has also been proposed and implemented, which enables the measurement of the cell surface charge with better resolution than the conventional dynamic methods. Technically, with the improvements made on the image processor, feedback controller and other technical aspects, the precise measurements of the above quantities become possible. Experimentally, measurements have been conducted on *Canola* protoplasts for various medium conditions and cell sizes. To the best of our knowledge, it is the first time that a complete and precise DEP spectrum response of individual cell has been obtained over a wide frequency range (1 Hz ~ 50 MHz).

Theoretically, the shelled spherical model[39] has been examined morphologically, analytically and numerically to find the direct affects of cellular and medium parameters on the DEP spectra and the mid cross-zero frequency (f_0). Comparing these theoretically obtained spectra and data with those experimental measured, it has been verified that the

polarization responses of the plant protoplasts in the mid and high frequency regions (where the surface conductivity effects associated with counterion polarization are negligible) can be faithfully predicted by the shelled spherical model. Based on this model several cellular parameters of *Canola* protoplasts have been estimated, with the conductivity of the cytoplasm ≈ 4000 μS/cm, the membrane capacitance ≈ 0.55 ± 0.02 μF/cm^2, and the membrane conductivity is less than 0.1 μS/cm and possibly in the range of 0.01 μS/cm. This shelled spherical model does not include the surface charge mediated counterion polarization and hence fails to explain the observed low-frequency polarization characteristics. The polarization behaviour in this frequency region is at present qualitatively interpreted as due to the presence of frequency dependent surface conductivity which is caused by the charged surface. It is found experimentally that this surface conductivity is linearly dependent on the conductivity of the suspending medium.

The dielectrophoretic and electrophoretic measurements have also been conducted on *Canola* protoplasts for various medium *pH* values. It is observed that the medium *pH* influences the magnitudes of Re[$\underline{K}_e$] in both the high frequency (flat band portion) and the low frequency regions. The measured surface charge density shows a significant dependence on the *pH* of the suspending medium.

7.2 Existing Problems and Recommendations for Further Work

7.2.1 Instrumentation Aspect

Although our DEP levitation system has been proved to be very effective, some problems still need to be resolved. With our present levitation electrode chamber it was found during the experiments that after each loading of fresh cell suspension to the

chamber, the fluid inside the chamber usually takes some time (10 ~ 30 min) to become stable, which is the prerequisite for accurate and reliable result. It sometimes consume the major time period for each DEP spectrum measurement. Another inconvenience of such a chamber design is the less control over the choice of certain cells (e.g. size, shape). A significant improvement might be a controllable cell injection chamber system to permit continuous, time-saving measurements on different cells.

With our present system, the frequency-dependent electrode polarization impedance has to be measured whenever the medium conductivity and the applied low-frequency voltage are changed (due to the medium conductivity and voltage dependencies of the polarization effect) and each set of DEP data has to be corrected after the measurement is performed. These procedures are very tedious and time-consuming. It therefore would be helpful to incorporate the measurement of the electric current passing through the electrode chamber so that the polarization effect can be determined and the data be corrected on-line. Such a measuring scheme has been proposed here and is shown in Figure 7.1. In addition to the feedback-loop via the imager, another electrical feedback-loop has been incorporated. In the single frequency levitation region this feedback-loop is paralyzed because the low-frequency voltage V_f is not applied, and the actual voltage cross the electrodes is linearly related to the applied voltage V_{app} via a constant coefficient (because electrode polarization does not come into play yet). In the double frequency levitation region, the low-frequency voltage V_f is applied and the electrical feedback-loop is activated to keep the actual low-frequency voltage V'_f constant. The frequency-dependent ratios of V'_f to V_f are then recorded and used for on-line correction.

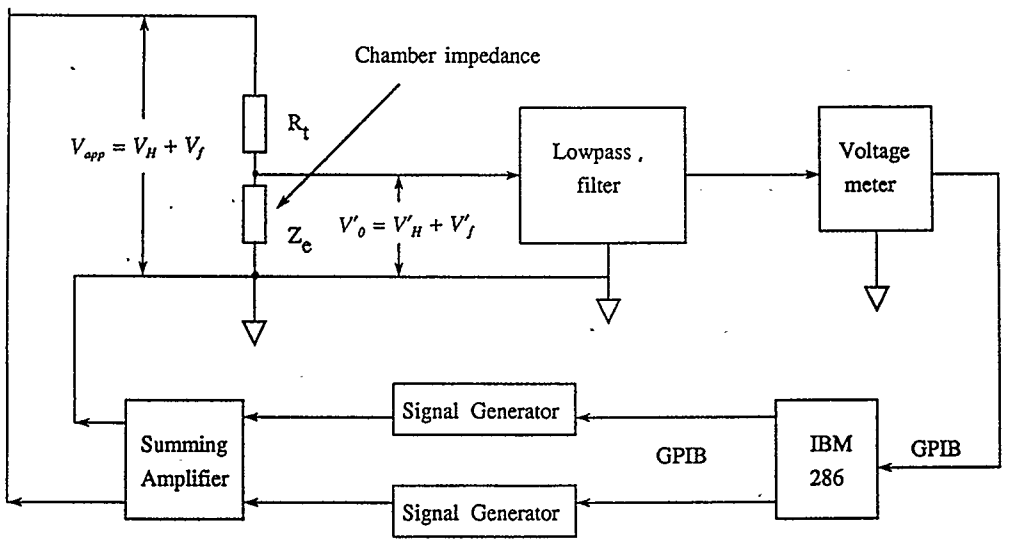

Figure 7.1. The block diagram of a proposed on-line electrode impedance measuring scheme

7.2.2 Experimental Aspects

Although it has been shown experimentally that the saponin treatment could increase the slope of $f_0 \cdot R \sim \sigma_1$ plots, which suggests an increase in the membrane conductivity, this however should be further verified through the measurements of $f_0 \sim R$ relation (see Chapter 6). As we discussed earlier, the difference of y-intercepts between the model predicted and the experimentally measured $f_0 \cdot R \sim \sigma_1$ plots (see Figure 6.7) is probably due to the presence of surface conductivity (caused by the charged surface and possibly membrane potential), this could be verified by treating the cells with certain chemical

agents to "kill" the cells physiologically without physical destruction (the effect is to minimize the surface charge and membrane potential).

7.2.3 Other Relevant Research Area

It is known that electrorotation measurement can determine the imaginary part of $\underline{K}_e$, i.e., Im[$\underline{K}_e$]. Both Re[$\underline{K}_e$] and Im[$\underline{K}_e$] predicted with shelled spherical model are shown here in Figure 7.2. It is shown that each dispersions in Re[$\underline{K}_e$] (DEP spectrum) correspond to a peak in Im[$\underline{K}_e$] (rotational spectrum). Jones and Kaler[59] have studied theoretically the relationship of rotational and dielectrophoretic cell spectra and combined them together in the Argand diagram. They have shown that for multilayered cell with widely spaced relaxation frequencies, the diagram appear as linked semicircular arcs, with one semicircle for each distinct relaxation mechanism. Therefore the availability of rotation spectra of biological cells will facilitate the better understanding of the polarization mechanisms of the cells. The present measuring techniques however are all based on manual counting of rotating cycle for each frequencies, which is extremely tedious, time consuming, and prone to error. Hence an automated image analysis system is necessary. With the image processing and analysis algorithms proposed in Section 4.4.2, it is feasible, at least methodologically, to develop such an analysis system.

Our DEP levitation system, not restricted to levitation of single cells, may also be useful in studying cell chains. Levitation of such chains could provide valuable insight into the nature of dipole-dipole interaction forces developed between contacting cells. Such measurements may prove useful in probing the underlying mechanism(s) operative in electric field mediated cell fusion (electrofusion).

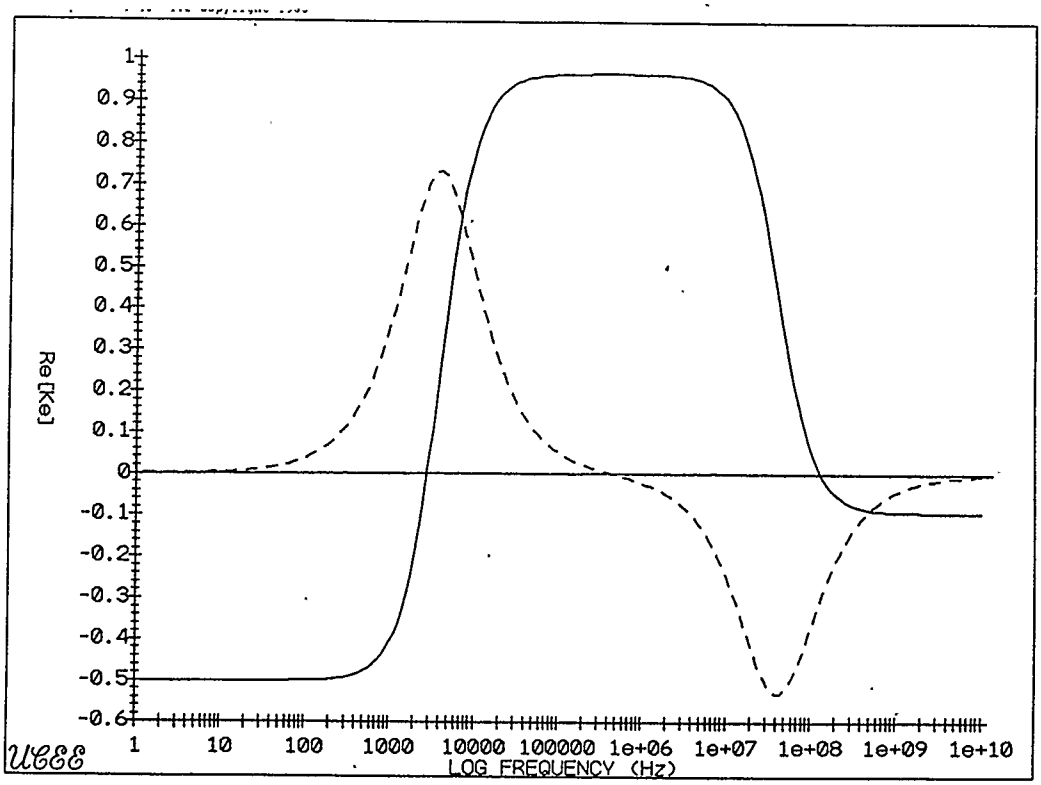

Figure 7.2. Rotational and dielectrophoretic spectra for shelled spherical cell model

REFERENCES

1. K.R. Foster and H.P. Schwan, "Dielectric Properties of Tissues and Biological Materials: A Critical Review," *Critical Reviews in Biomedical Engineering*. **17** pp. 25-101 (1989).

2. H.P. Schwan, "Electrical Properties of Tissue and Cell Suspensions," *Adv. Biol. Med. Phys.* **5** pp. 147-209 (1957).

3. H.P. Schwan, "Determination of Biological Impedance," *Phys. Tech. Biol. Res.* **6** pp. 323-407 (1963).

4. T. Hanai, K. Asàmi, and N. Koizumi, "Dielectric Theory of Concentrated Suspensions of Shell-Spheres in Particular Reference to the Analysis of Biological Cell Suspensions," *Bull. Inst. Chem. Res. Kyoto Univ.* **57** pp. 297-305 (1979).

5. H. Fellner-Feldegg, "The Measurement of Dielectrics in the Time Domain," *The Journal of Physical Chemistry*. **73** pp. 616-623 (1969).

6. H. Fricke, "The Complex Conductivity of Suspension of Stratified Particles of Spherical or Cylindrical Form," *J. Phys. Chem.* **59** pp. 168-170 (1955).

7. F. Bordi, C. Cametti, and A. di Biasio, "Passive Electrical Properties of Biological Cell Membranes Determined from Maxwell-Wagner Conductivity Dispersion Measurements," *Bioelectrochemistry and Bioenergetics*. **22** pp. 135-144 (1989).

8. E.H. Grant, R.J. Sheppard, and G.P. South, *Dielectric Behaviour of Biological Molecules in Solution*. Clarendon Press (Oxford University Press), Oxford (1978).

9. B. Sakmann and E. Neher, *Single Channel Recording*. Plenum Publishing Corp., New York (1983).

10. S. Takashima, K. Asami, and T. Takahashi, "Frequency-Domain Studies of Impedance Characteristics of Biological Cells Using Micropipette Technique," *Biophysi. J.* **54** pp. 995-1000 (1988).

11. W.M.Arnold and U.Zimmermann, "Rotating-Field-Induced Rotation and Measurement of the Membrane Capacitance of Single Mesophyll Cells of *Avena sativa*," *Z. Naturforsch. Teil C Biochem. Biophys. Biol. Virol.* **37** pp. 908-915 (1982).

12. W.M. Arnold and U. Zimmermann, "Electrorotation: Development of a Technique

for Dielectric Measurements on Individual Cells and Particles," *J. Electrostatics.* **21** pp. 151-191 (1988).

13. T. Nagata and G. Melchers, "Surface Charge of Protoplasts and Their Significance in Cell-Cell Interaction," *Planta.* **142** pp. 235-238 (1978).

14. I. Obi, Y. Ichikawa, T. Kakutani, and M. Senda, "Electrophoresis, Zeta Potential and Surface Charges of Barley Mesophyll Protoplasts," *Plant Cell Physiol.* **30** pp. 129-135 (1989a).

15. I. Obi, Y. Ichikawa, R. Nonaka, T. Kakutani, and M. Senda, "Electrophoretic Studies on Plant Protoplasts: II. Relative Amount of Various Charged Groups on the Surface of Barley Mesophyll Protoplasts," *Plant Cell Physiol.* **30** pp. 759-764 (1989c).

16. A. Tulp, A. Timmerman, and M.G. Barnhoorn, "A Separation Chamber to Sort Cells and Cell Organelles by Weak Physical Forces. I. Preparative Electrophoresis of Cells in Stationary Density Gradients at Low Electric Field Strength," *Anal. Biochem.* **124** pp. 432-439 (1982).

17. H.A. Pohl, *Dielectrophoresis : The Behaviour of Neutral Matter in Nonuniform Electric Fields.* Cambridge University Press, Cambridge (1978).

18. H.A. Pohl and I. Hawk, *Science* **152** pp. 647 (1966).

19. Karan Kaler and H.A. Pohl, "Dynamic Dielectrophoretic Levitation of Living Individual Cells," *IEEE Trans. Ind. Appl.* **IA-19**(6) pp. 1089-1093 (1983).

20. K.V.I.S. Kaler and T.B. Jones, "Dielectrophoretic Spectra of Single Cells Determined by Feedback-Controlled Levitation," *Biophys. J.* **57** pp. 173-182 (1990).

21. J.A.R. Price, J.P.H. Burt and R. Pethig, "Applications of a New Optical Technique for Measuring the Dielectrophoretic Behaviour of Micro-Organisms," *Biochimica et Biophysica Acta.* **964** pp. 221-230 (1988).

22. J.P.H. Burt, R. Pethig, P.R.C. Gascoyne, and F.F. Becker, "Dielectrophoretic Characterisation of Friend Murine Erythroleukaemic Cells as a Measure of Induced Differentiation," *Biochimica et Biophysica Acta.* **1034** pp. 93-101 (1990).

23. K.V.I.S. Kaler, O.G. Fritz Jr., and R.J. Adamson, "Dielectrophoretic Velocity Measurements Using Quasi-Elastic Light Scattering," *J. Electrostat.* **21** pp. 193-204 (1988).

24. R.J. Adamson and K.V.I.S. Kaler, "An Automated Stream-Centered Dielectrophoretic System," *IEEE Trans. Ind. Appl.* **IA-24**(1) pp. 93-98 (1988).

25. H.A. Pohl, K. Kaler, and K. Pollock, "Continuous Positive and Negative Dielectrophoresis of Microorganisms," *J. Biol. Phys.* **9** pp. 67-85 (1981).

26. P. Marsalek and J.J. Zielinski, "Experimental Verification of a Theoretical Treatment of the Mechanism of Dielectrophoresis," *Bioelectrochemistry and Bioenergetics.* **22** pp. 289-298 (1989).

27. T.B. Jones and G.A. Kallio, "Dielectrophoretic Levitation of Spheres and Shells," *J. Electrostat.* **6** pp. 207-224 (1979).

28. T.B. Jones, *Electromechanical Interactions of Dielectric (and Magnetic) Particles.* Lecture Notes Presented at Univ. of Calgary. (1988).

29. F.A. Sauer, "Interaction Forces Between Microscopic Particles in an External Electromagnetic Field," *Interactions Between Electromagnetic Field and Cells.* A. Chiabrera, C. Nicolini, and H.P. Schwan, editors. Pelenum Publishing Corp., New York. pp. 181-202 (1985).

30. H. Pauly and H.P. Schwan, "Über die Impedanz einer Suspension von kugelfÖrmigen Teilchen mit einer Schale," *Z. Naturforsch. Teil B.* **14** pp. 125-131 (1959).

31. R. Pethig and D.B. Kell, "The Passive Electrical Properties of Biological Systems: Their Significance in Physiology, Biophysics and Biotechnology," *Phys. Med. Biol.* **32** pp. 933-970 (1987).

32. G. Schwarz, "A Theory of the Low Frequency Dielectric Dispersion of Colloidal Particles in Electrolyte Solutions," *J. Phys. Chem.* **66** pp. 2636-2642 (1962).

33. S.S. Dukhin and V.N. Shilov, *Dielectric Phenomena and the Double Layer in Disperse Systems and Polyelectrolytes.* Halsted Press (1974).

34. M. Fixman, "Thin Double Layer Approximation for Electrophoresis and Dielectric Response," *J. Chem. Phys.* **78** pp. 1483-1491 (1983).

35. W.C. Chew and P.N. Sen, "Dielectric Enhancement due to an Electrochemical Double Layer Approximation," *J. Chem. Phys.* 77 pp. 4683-4690 (1982).

36. M. Mandel and T. Odijk, "Dielectric Properties of Polyelectrolyte Solutions," *Annu. Rev. Phys. Chem.* **35** pp. 75-87 (1984).

37. C. Grosse and K.R. Foster, "Permittivity of a Suspension of Charged Spherical Particles in Electrolyte Solution," *J. Phys. Chem.* **91** pp. 3073-3080 (1987).

38. C. Grosse, "Permittivity of a Suspension of Charged Spherical Particles in Electrolyte Solution. 2. Influence of the Surface Conductivity and Asymmetry of the Electrolyte on the Low and High Frequency Relaxations," *J. Phys. Chem.* **92** pp. 3905-3910 (1988).

39. T.B. Jones and G.W. Bliss, "Bubble Dielectrophoresis," *J. Appl. Phys.* **48** pp. 1412-1417 (1977).

40. A.S. Bahaj and A.G. Bailey, "Dielectrophoresis of Small Particles," *Proceedings of the Industry Applications Society (IEEE) 1979 Annual Meeting, Cleveland, OH.* pp. 154-157.

41. G.A. Kallio and T.B. Jones, "Dielectric Constant Measurements Using Dielectrophoretic Levitation," *IEEE Trans, Ind. Appl.* **IA-16** pp. 69-75 (1980).

42. T.B. Jones and J.P. Kraybill, "Active Feedback-Controlled Dielectrophoretic Levitation," *J. Appl. Phys.* **60** pp. 1247-1252 (1986).

43. R.C. Gonzalez and P. Wintz, *Digital Image Processing.* 2nd Ed. Addison-Wesley Publishing Company (1987).

44. J.M.S. Prewitt and M.L. Mendelsohn, "Analysis of Cell Images," *Ann. N.Y. Acad. Sci.* **128** pp. 1035-1043 (1966).

45. B. Dahlqvist, E. Bengtsson, O. Eriksson, T. Jarkrans, and B. Stenvkist, "Segmentation of Microscopic Cell Images by Minimum Error Thresholding," *Proceedings of 2nd Scandivinavian Conference on Image Analysis, Helsinki* pp. 306-313 (1981).

46. W.A. Barret, "An Iterative Algorithm for Multiple Thresholding Detection," *Proc. IEEE Comp. Soc. Conf. on P.R.I.P. Dallas, TX*, pp. 273-278 (1981).

47. B. Nordin, E. Bengtsson, B. Dahlqvist, O. Eriksson, T. Jarkrans, and B. Stenkvist, "Object Oriented Cell Image Segmentation," *1st international Symposium on Medical Imaging and Image Interpretation, ISMIII'82, Berlin*, pp. 140-145 (1982).

48. T. Pavlidis, *Algorithms for Graphics and Image Processing.* Computer Science Press: Rockville, Md., 1982.

49. C.R. Dyer and A. Rosenfeld, "Thinning Algorithms for Grayscale Pictures," *IEEE Trans. Pattern Anal. Machine Intell.*, **PAMI-1**, pp. 88-89 (1979).

50. E. Persoon, "Shape Discrimination Using Fourier Descriptors," *IEEE Trans. Systems, Man, Cybernetics SMC-7*, pp. 170-179 (1977).

51. F.P. Kuhl, "Elliptic Fourier Features of Closed Contour," *Computer Graphics and Image Processing*. **18** pp. 236-258 (1982).

52. D. Adelh and J.M. Chassery, "Shape Analysis of Ostracodes: Feature Extraction, Classification and Automation," *1st international Symposium on Medical Imaging and Image Interpretation, ISMIII'82, Berlin*, pp. 292-296 (1982).

53. C.L. Phillips and R.D. Harbor, *Feedback Control Systems*. Prentice-Hall, Inc., Englewood Cliffs, New Jersey (1988).

54. H.P. Schwan, "Electrode Polarization Impedance and Measurements in Biological Materials," *Ann. N.Y. Acad. Sci.* **148** pp. 191-209 (1968).

55. D.B. Kell in A.P.F. Turner, I. Karube and G.S. Wilson (Eds.), *Biosensors*, Oxford University Press, Oxford, New York, Tokyo. pp. 427 (1987).

56. Y. Chizmadzhev, A. Yu, P.I. Kuzmin, and V. Pastushenko, "Theory of the dielectrophoresis of vesicles and cells," *Biol. Membr.* **2** pp. 1147-1161 (1985).

57. H.P. Schwan, G. Schwarz, J. Maczuk and H. Paul, "On the Low Frequency Dielectric Dispersion of Colloidal Particles in Electrolyte Solution," *J. Phys. Chem.* **66** pp. 2626-2635 (1962).

58. K. Kaler, J.P. Xie, T.B. Jones, and R. Paul, "Double Frequency Dielectrophoretic Levitation," in Press.

59. T.B. Jones and K.V.I.S. Kaler, "Relationship of Rotational and Dielectrophoretic Cell spectra," *Annual International Conference of the IEEE Engineering in Medicine and Biology Society*, Vol. 12, No. 4, pp. 1515-1516 (1990).

APPENDIX

MATHEMATICAL PROOF OF DOUBLE FREQUENCY SCHEME

It has been known that for a spherical particle of radius R, the time averaged DEP force is given by

$$\langle F_{DEP} \rangle = 2\pi R^3 \varepsilon_1 \, Re[\underline{K}_e(\omega)] \, \nabla E_{rms}^2 \qquad \textbf{(A1)}$$

With E in Eq.(A1) replaced by a sum of two field terms such that

$$E(t) = E_1 \sin(\frac{2\pi}{T_1} t + \phi) + E_2 \sin(\frac{2\pi}{T_2} t) \qquad \textbf{(A2)}$$

By mathematical definition, the mean square value of $E(t)$ is given by

$$E_{rms}^2 = \frac{1}{T} \int_0^T [E_1 \sin(\frac{2\pi}{T_1} t + \phi) + E_2 \sin(\frac{2\pi}{T_2} t)]^2 \, dt \qquad \textbf{(A3)}$$

where T is the integral period which can be chosen to be either the common multiples of T_1 and T_2 or far greater. In our case it can be chosen as the system response time (in the order of seconds). Assume $T_2 = (n + \delta)T_1$, where $0 < \delta < 1$, and $T = mT_2$, Eq.(A3) can be written by

$$E_{rms}^2 = \frac{1}{m(n+\delta)T_1} \int_0^{m(n+\delta)T_1} [E_1 \sin(\frac{2\pi}{T_1} t + \phi) + E_2 \sin(\frac{2\pi}{(n+\delta)T_1} t)]^2 \, dt \qquad \textbf{(A4)}$$

$$= E_{1rms}^2 + E_{2rms}^2 + \mathfrak{L}$$

where the error term ϱ is given by

$$\begin{aligned}\varrho &= -\frac{E_1^2 \sin(4\pi m\delta)}{8\pi m(n+\delta)} \\ &\quad + \frac{2E_1E_2\sin(m\delta\pi)}{m[(n+\delta)^2-1]\pi}[\cos(m\delta\pi)\cos\phi + (n+\delta)\sin(m\delta\pi)\sin\phi] \\ &\le \frac{E_1^2}{8\pi m(n+\delta)} + \frac{2E_1E_2}{m(n+\delta-1)\pi} \\ &< \frac{E_1^2}{8\pi mn} + \frac{2E_1E_2}{m(n-1)\pi}\end{aligned} \tag{A5}$$

For our system and implementation, T is in the order of second, $1/T_1 = 3$ MHz and is fixed. Taking a worst case as an example, assume $1/T_2 = 500$ KHz $n = 5$, $T = 0.5$ s, we will obtain

$$\varrho \approx 3.8\times10^{-7}\, E_1^2 + 5.3\times10^{-7}\, E_1E_2 \tag{A6}$$

From above analysis and result we can see that this error term is negligible.